Understanding the properties of accretion powered Be/X-ray binary pulsars

A thesis submitted in partial fulfilment of

the requirements for the degree of

Doctor of Philosophy

by

Shivangi Gupta

(Roll No. 15330007)

Under the guidance of

Prof. Sachindranatha Naik

Astronomy and Astrophysics Division

Physical Research Laboratory, Ahmedabad, India.

DEPARTMENT OF PHYSICS

INDIAN INSTITUTE OF TECHNOLOGY GANDHINAGAR

July, 2020

Declaration

I, Shivangi Gupta, declare that this written submission represents my ideas in my own words and where others' ideas or words have been included, I have adequately cited and referenced the original sources. I also declare that I have adhered to all principles of academic honesty and integrity and have not misrepresented or fabricated or falsified any idea/data/fact/source in my submission. I understand that any violation of the above can cause disciplinary action by the Institute and can also evoke penal action from the sources which have thus not been properly cited or from whom proper permission has not been taken when needed.

(Signature)

(Name: Shivangi Gupta)

(Roll No: 15330007)

Date:

Certificate

It is certified that the work contained in the thesis entitled **"Understanding the properties of accretion powered Be/X-ray binary pulsars"** by **Ms. Shivangi Gupta** (Roll number: 15330007), has been carried out under my supervision and that this work has not been submitted elsewhere for any degree or diploma.

I have read this dissertation and in my opinion, it is fully adequate in scope and quality as a dissertation for the degree of Doctor of Philosophy.

Prof. Sachindranatha Naik
(Thesis Supervisor)
Professor
Astronomy & Astrophysics Division
Physical Research Laboratory
Unit of Department of Space, Govt of India
Ahmedabad-380009, Gujarat, India.

Dedicated to

My Teachers

Acknowledgements

As I have reached towards the completion of my thesis, it is an immense pleasure to express my deepest gratitude to all those people who have always been there to help and support me during the course of my PhD thesis work.

First and foremost, I would like to acknowledge my supervisor Prof. Sachindra Naik, who introduced me to the exciting field of "X-ray binaries". I am really grateful to have him as my mentor. His continuous support, guidance and encouragement have always helped me to deal with all kinds of situations in life personally and professionally. I would especially like to thank him for his valuable critique and discussions, which eventually helped me to develop a deeper understanding about the subject.

I would like to take this opportunity to thank all my collaborators. I have learned a lot from them throughout my PhD. Firstly, I would like to thank Dr Gaurava K. Jaisawal, who introduced me with X-ray data analysis in the early stage of my PhD. I especially thank him for addressing my innumerable doubts or questions and providing helpful suggestions whenever required. A special thanks to my senior and former officemate Dr Prahlad Rameya Epili. His expertise in software installation and handling have always fascinated me. I admire his helpful nature and enjoyed various fruitful discussions with him.

I convey a sincere thanks to my Doctoral Studies Committee, Dr Veeresh Singh and Dr Aveek Sarkar for checking my progress on a regular basis. Their valuable comments and remarks have always helped me to improve the scientific outcomes.

I express my gratitude to Prof. Anil Bhardwaj, Director, Physical Research Laboratory (PRL) for providing the necessary facilities to carry out my research work. I am also thankful to Prof. Abhijit Chakraborty, current area chairman of Astronomy and Astrophysics Division at PRL, for his support in the division to carry out this work. I am also indebted to all the faculty and staff members of our division for providing a pleasant research environment throughout all these years. I would like to extend my sincere thanks to the PRL Dean, Academic Committee Chairman and Registrar for their support during my research work at PRL. I am also thankful

to the Dean and Head of Physics Department at Indian Institute of Technology, Gandhinagar (IIT Gn) for their extended co-operation.

I am extremely fortunate to share the office space with many wonderful people during my Phd tenure. I would like to acknowledge Dr Main Pal, Dr Nilkanth D. Vagshette, Dr Shubahjeet Karmakar and Dr Arghajit Jana for various academic and non academic discussions. A special thanks to Dr Arti Joshi (babes), who in spite of being here for a short time, proved to be an extremely trustable and dependable friend. At last I would like to acknowledge my dearest junior Neeraj Kumari. I always enjoy her company and various stimulating discussions we have, and her thought provoking questions. I personally have learned a lot from all these people and I am grateful to have interacted with them.

I feel really blessed to have many good friends who always have been there for me. I will forever cherish the wonderful time spent with my dear batchmates, all my seniors and juniors of PRL. I would like to dedicate a heartiest thanks to my batchmates and closest friends Ranadeep Sarkar and Akanksha Bhardwaj, who always helped and unconditionally supported me in times of need. I would like to take this opportunity to thank my college friend Sudha Yadav, who has always been an integral part of my life. I am really fortunate to have a friend like her by my side.

Finally, I would like to express the deepest gratitude to my family and especially my parents, who always supported me and my education in all aspects. It would not have been possible for me to come this far without their love and faith in me. Last but not the least, I thank my brother (bhai) Vishal for his unconditional love and support.

- Shivangi Gupta

Abstract

This thesis is dedicated to understand the timing and spectral properties of accretion powered Be/X-ray binary pulsars. Accretion powered binary X-ray pulsars are system of highly magnetized neutron stars which accrete matter from non-degenerate companion and subsequently get powered in X-ray regime. Neutron stars are among the most compact objects in the universe, which contain more than a solar mass confined within spheres of $\sim$10 km radii. This results in an average density of a neutron star to be $\sim 10^{14}$g cm^{-3}, i.e. as high as that of the nuclear matter. Apart from the extreme density, the magnetic field of neutron star in these binary systems is of the order of 10^{8-12} G. These aspects make them one of the most exotic objects in the universe. Therefore, study of the accretion mechanism in these systems provide us with the opportunity to probe the properties of matter under extreme conditions, which otherwise is impossible to achieve through laboratory experiments.

During the process of accretion, the matter accreted from the non-degenerate optical companion follows the magnetic field lines and gets dumped onto the magnetic poles of the neutron star. This forms an accretion mound on the magnetic poles of the neutron stars. However, when the mass acretion rate is high, a column like structure, known as the 'accretion column', is formed at the magentic poles of the neutron star. A radiation dominated shock is expected to form in the accretion column which decelerates the infalling plasma before settling on to the surface of neutron star. Consequently, the surface temperature at the magnetic poles reaches as high as 10^7 K, resulting in X-ray emission. The interaction of this radiation with the infalling plasma, through complex physical processes, shapes the resulting spectral continuum of the neutron star. As the spin and magnetic axes are usually misaligned, the beam of X-ray radiation from the magnetic poles of the neutron star can be detected once it sweeps through the line of sight of the observer. This result in apparent X-ray pulsations, hence the neutron star in these systems is known as pulsar.

The emission characteristics of this radiation depend upon the mass accretion rate and hence on the luminosity. Therefore, it is interesting to investigate the characteristic properties

of these X-ray sources at different luminosities. One such class of X-ray binaries, showing extreme variability in terms of luminosity is, Be/X-ray binary pulsars. The neutron star in these systems revolve in a wide eccentric orbit around its Be optical companion and remain in quiescence most of the time. However, once it approaches the periastron, mass accretion from the circumstellar disk of the Be star becomes possible and the neutron star consequently show strong X-ray outburst activities, known as Type I outburst. The X-ray luminosity during these outburst events can reach as high as 10-100 times the quiescent luminosity ($L_{quiescent} \approx 10^{34}$ erg s^{-1}). Another kind of X-ray enhancement, i.e. Type II outbursts are also detected from these systems. The Type II outbursts are rare and independent of the orbital motion of the binary system. The X-ray luminosity during these (giant outburst) events may even reach as high as $\geq 10^{38}$ erg s^{-1}. Due to extreme variability and strong mass accretion rate during these X-ray outburst events, Be/X-ray binaries are ideal sources to study the luminosity dependence of the emission characteristics of the X-ray pulsars, which is the main focus of the present thesis.

In this work, I have carried out a detailed and systematic investigation of the spectral and timing properties of Be/X-ray binary pulsar 2S 1417-624. Using large number of *RXTE* pointed observations, taken during the 2009 giant X-ray outburst of 2S 1417-624, a systematic change in the shape of the pulse profile of the pulsar was observed. The pulse profiles were found to exhibit a transition from two-peak structure to three-peak during the rise of 2009 Type II outburst, while a reverse trend was observed during the outburst decline. At the same time, the pulsed fraction of the pulsar was found to be anti-correlated with the source luminosity. This kind of variation was never seen previously, for any kind of X-ray activity observed from this source. In order to probe the cause of such variation, a detailed phase averaged and pulse phase resolved spectroscopy was performed for each epoch of the observation. The spectral continuum was found to be described well with an absorbed cut-off power law model with an additional Gaussian component for the iron emission due to Fe K_{α}. The dependence of the spectral parameters on the source luminosity was studied for the first time in great detail. It was found that the observed changes in spectral and timing properties

of the pulsar pointed towards the change in the accretion geometry close to *critical luminosity* regimes. This subsequently allowed to constrain one of the most fundamental physical parameter of the pulsar, i.e. magnetic field strength, by using the relation between critical luminosity and the magnetic field strength (Becker et al., 2012).

Recently in 2018, 2S 1417-624 showed another giant outburst activity and was observed simultaneously with *NuSTAR* and *Swift* X-ray observatories at the outburst peak. This was the most luminous outburst detected from the pulsar till date and provided a unique opportunity to carry out a systematic analysis of the emission characteristic of the pulsar at even higher luminosity. The pulse profiles of the pulsar during this event was found to evolve further to four-peak structure. This was a direct observational evidence of the strong dependence of the emission geometry of pulsar on the mass accretion rate. The phase averaged spectrum of the pulsar was different as compared to its previous outburst events and found to be described only with a composite model consisting of an absorbed cut-off power law model, a Gaussain component for iron fluorescence emission and an additional blackbody emission component with a temperature of ≈1 keV (soft X-ray excess). The detection of soft-excess emission in the pulsar spectrum is quite rare. Therefore, a detailed pulse phase resolved spectroscopy was performed in order to probe the origin of this component. Moreover, a detailed physical modeling was carried out for the first time in this work to describe the X-ray spectrum of 2S 1417-624 self consistently, using physically motivated spectral continuum model `COMPMAG` (Farinelli et al., 2012). The results obtained from these studies are discussed in great detail in the thesis.

Keywords: X-ray binaries, Accretion powered Pulsars, Magnetic fields, Accretion, Pulse profiles, Spectroscopy, Pulse phase resolved spectroscopy, Critical luminosity.

List of Publications

I. In Refereed Journals included in the Thesis

1. **Gupta, S.**, Naik, S., Jaisawal, G. K., 2019, *"NuSTAR view of Be/X-ray binary pulsar 2S 1417-624 during 2018 giant outburst"*, **Monthly Notices of the Royal Astronomical Society**, 490, 2458.

2. **Gupta, S.**, Naik, S., Jaisawal, G. K., Epili, P. R., 2018, *"Spectral and timing studies of 2S 1417-624 during a giant outburst"*, **Monthly Notices of the Royal Astronomical Society**, 479, 5612.

II. Additional Publications in Refereed Journals

1. Jaisawal, G. K., Naik, S., **Gupta, S.**, Chenevez, J., Epili, P., 2018, *"A curious case of the accretion-powered X-ray pulsar GX 1+4"*, **Monthly Notices of the Royal Astronomical Society**, 478, 448.

2. Epili, P., Naik, S., Jaisawal, G. K., **Gupta, S.**, 2017, *"Decade long RXTE monitoring observations of Be/X-ray binary pulsar EXO 2030+375"*, **Monthly Notices of the Royal Astronomical Society**, 472, 3455.

Contents

List of Figures

List of Tables

Physical Constants

Speed of light	$c = 2.997 \times 10^{10}$ cm s^{-1}
Planck constant	$h = 6.626 \times 10^{-27}$ erg s^{-1}
Gravitational constant	$G = 6.672 \times 10^{-8}$ cm^3 g^{-1} s^{-2}
Boltzmann's constant	$k_B = 1.380 \times 10^{-16}$ erg K^{-1}
Mass of electron	$m_e = 9.109 \times 10^{-28}$ g
Mass of proton	$m_p = 1.673 \times 10^{-24}$ g
Parsec	pc $= 3.086 \times 10^{18}$ cm
Solar Mass	$M_\odot = 1.989 \times 10^{33}$ g
Solar Luminosity	$L_\odot = 3.826 \times 10^{33}$ egs s^{-1}
Solar Radius	$R_\odot = 6.959 \times 10^{10}$ cm

List of Abbreviations

XRB	X-ray binary
XBP	X-ray binary pulsar
HMXB	High mass X-ray binary system
LMXB	Low mass X-ray binary system
ULX	Ultraluminous X-ray source
AMXP	Accreting millisecond X-ray pulsar
BH	Black hole
NS	Neutron star
WD	White dwarf
CV	Cataclysmic variable
SGXB	Supergiant X-ray binary
Be/XRB	Be/X-ray binary
SFXT	Supergiant fast X-ray transient
SMC	Small Magellanic Cloud
LMC	Large Magellanic Cloud
QPO	Quasi periodic oscillation
RLO	Roche Lobe overflow
RTE	Radiative transfer equation
CRSF	Cyclotron resonant scattering feature
RXTE	Rossi X-ray Timing Explorer
PCA	Proportional Counter Array
HEXTE	High Energy X-ray Timing Experiment
ASM	All Sky Monitor
XRT	X-ray Telescope
GRB	Gamma-Ray Burst
BAT	Burst Alert Telescope
NuSTAR	Nuclear Spectroscopic Telescope Array
FPM	Focal Plane Module
FWHM	Full width at half maximum
SAA	South Atlantic Anomaly
PDS	Power density spectrum
HXMT	Hard X-ray Modulation Telescope
NICER	Neutron star Interior Composition Explorer mission
XTI	X-ray Timing Instrument
GBM	Gamma-ray Burst Monitor

Chapter 1

Introduction

1.1 The dawn of X-ray astronomy

Earth's atmosphere is opaque to X-ray photons and makes the X-ray observations of extra-terrestrial sources a daunting task. Therefore, the study of the cosmos in X-ray band became possible only after the advent of rocket technology i.e., the ability to send the X-ray detectors above the Earth's atmosphere via sounding rockets. The idea of the Sun being a prominent X-ray emitter existed before though the first confirmation of solar X-rays came only when the V-2 sounding rocket was flown above the atmosphere of Earth on 28 January 1949 (Friedman et al., 1951). Consequently, the NASA launched *Aerobee* rocket in 1962, which carried Geiger counters onboard it. One of the main scientific objective of this experiment was to carry out a detailed study of solar radiation reflected from the surface of the moon. This experiment serendipitously discovered the extra-solar X-rays, which seemed to be distributed evenly across the sky. Apart from the uniform distribution of X-ray radiation, the first X-ray source outside the solar system was detected in the Scorpius constellation and was subsequently named as Sco X-1 (Giacconi et al., 1962). This was a historic step towards the origin of X-ray astronomy. Subsequent studies showed that Sco X-1 is 10,000 times more brighter in X-rays compared to that of the Sun in the entire band of electromagnetic spectrum. This discovery astonished the researchers across the globe and the concept of mass accretion was first evoked to explain

the origin of high energy emission from this source. This was a major step towards the understanding of *accretion* as the main source of energy production mechanism (Zeldovich & Guseynov, 1966).

Inspite of being restricted to their fly time and limited field of view, the sounding rockets and balloon borne experiments provided the earliest pathways toward our understanding of X-ray universe for about a decade until the first X-ray satellite *Uhuru* was launched. *Uhuru*, also known as *Small Astronomy Satellite* (SAS-A) was the first orbiting X-ray mission launched by NASA in late 1970. During three years of its mission lifetime, *Uhuru* provided the first extensive catalogue, listing more than 300 X-ray sources in the sky (Forman et al., 1978). These sources mostly include X-ray binaries, cluster of galaxies, supernova remnants, and Active Galactic Nuclei (AGNs). One crucial discovery which is of particular importance was the detection of pulsed X-ray emission from neutron star X-ray binaries, Cen X-3 (Giacconi et al., 1971) and Her X-1 (Tananbaum et al., 1972). Although the existence of neutron stars as the stellar remnants had already been predicted theoretically by Baade & Zwicky (1934), their observational evidence came only in 1967 when Jocelyn Bell discovered the first pulsar PSR B1919+21 in radio band (Hewish et al., 1968). Soon, it was shown by Lamb et al. (1973) that only a strongly magnetized neutron star (B $\approx$ 10^{12} G) would be able to focus the accreting material (in the form of accretion stream) on to the magnetic poles, thereby producing beams of radiation along its magnetic axis. If the magnetic and spin axes of the neutron star are misalligned, the radiation beams from the magnetic poles make the rotating neutron star appear as emitting pulses of radiation coherent with its spin period and hence known as pulsars.

The present thesis is focused on the spectral and timing investigation of accretion powered X-ray pulsars. The main system under investigation is Be/X-ray binary pulsars (see the following sections for the classification and properties of accretion powered pulsars). Be/X-ray binary pulsars show luminosity dependent behavior in the sense that the pulse profiles and spectral properties change with the change in the mass accretion rate (luminosity) of the pulsar. The cause of such behavior is still not well understood. Therefore, we have investigated

the spectral and timing properties of Be/X-ray pulsars at different luminosity ranges. The following sections describe the classification and formation theories of X-ray binaries, basics of accretion physics, possible modes of mass transfer mechanism in binary systems, properties of accretion powered X-ray pulsars, the pulsar magnetosphere, the accretion column and emission mechanism for the X-ray pulsars.

1.2 X-ray binaries : Classification and evolution

X-ray binaries (XRBs) are the systems of two stars in which a compact object i.e., a black hole, a neutron star or a white dwarf co-rotates with its optical companion around the common center of mass (Lewin et al., 1995). Depending upon the nature of the compact object present in the binary system, the XRBs are classified into: (i) Black hole X-ray binary (BH-XRB) (ii) Neutron star X-ray binary (NS-XRB) and (iii) White dwarf X-ray binary (WD-XRB or CV i.e., Cataclysmic Variable). X-ray emission from the compact object in the binary system is powered by accretion of matter from the optical companion to the compact object. Typical luminosity of XRBs ranges from 10^{34}–10^{38} erg s^{-1}, which could even exceed $\sim 10^{41}$ erg s^{-1} for Ultraluminous X-ray binary sources (ULXs; Kaaret et al. 2017). Such events could occasionally outshine the host galaxy, making XRBs as one of the brightest objects in the X-ray sky. Depending upon the mass of donor star (M_{donor} or the optical companion), the XRBs are further classified into low mass X-ray binary (LMXB; $M_{donor} < 2\ M_{\odot}$) and high mass X-ray binary (HMXB; $M_{donor} > 8\ M_{\odot}$). We note that this classification is valid only in the cases of NS and BH-XRBs. However, the other group of XRBs, i.e., CVs can be classified into magnetic and non-magnetic ones (on the basis of the strength of the magnetic field of white dwarf). For more details on this class of XRBs, refer to Lewin et al. (1995) and Warner (2003).

The fact that one component of the binary system have reached its end stage, indicates that the binary system as a whole must have gone through various stages of evolution via angular momentum transfer and mass exchange between the members of the binary system.

Further, the mass transfer from the donor star to the compact object can take place through three different processes: (i) Roche-lobe overflow, (ii) capture of wind emanating from the photosphere of the optical companion or (iii) accretion from the Be circumstellar disk (see section 1.3 for the details about various accretion modes). Generally, the Roche-lobe overflow is considered to be a dominant mode of mass transfer mechanism for the LXMBs, whereas, the other two possibilities are usually seen in case of HMXBs. In the following section, the properties and possible formation theories for HMXB and LMXB systems are presented.

1.2.1 High Mass X-ray Binaries (HMXBs)

The HMXBs constitute about one-third of the known population of X-ray binaries in our Galaxy (Liu et al., 2006). These systems are relatively younger and are generally found in the star forming regions of the galactic disk. The compact object in HMXBs is mostly a neutron star which accretes matter from an early-type massive OB companion star. Furthermore, depending upon the type and luminosity class of the optical companion, the HMXBs are classified into Supergiant X-ray binaries (SGXBs; with a supergiant companion of luminosity class I-II) and Be/X-ray binaries (Be/XRBs; dwarf, sub-dwarf or giant OB companion with luminosity class III-V).

In SGXB systems, the neutron stars are deeply embedded in the supersonic stellar wind (with a terminal velocity of $\sim$1500 km s^{-1}) of the companion stars and show persistent emission in X-rays by capturing the stellar wind ($\sim 10^{-6}$ M$_{\odot}$ yr^{-1}; Puls et al. 2008). The orbital period of these systems is generally shorter than $\sim$ 15 days and a large fraction of these system shows eclipsing activity in their X-ray light curves. The supergiant companions in these system are close to filling their Roche-lobe and have masses typically in the range of 20 to 50 M$_{\odot}$. The total number of confirmed SGXB systems in our Galaxy is $\sim$30, more than half of which are discovered only recently i.e., after the advent of the *INTEGRAL* mission. Apart from detecting highly obscured systems among the SGXBs, the *INTEGRAL* discovered previously unknown population of SGXBs and classified them as Supergiant Fast

X-ray Transients (SFXTs; see Sidoli & Paizis 2018). Although the SGXBs are widely known as wind-fed systems, Cen X-3, SMC X-1 and LMC X-4 are the only exceptions among them i.e., being the disk-fed SGXB systems or perhaps the combination of both wind and disk accretion (Schreier et al. 1972; Petterson 1978; Blondin et al. 1991).

The other type of HMXB system i.e., Be/XRBs represents the largest sub-class of HMXBs with a currently known population of about 220 Be/XRB systems. The Small Magellanic Cloud (SMC) is particularly rich in these systems and hosts a large fraction of them ($\sim$70; Coe & Kirk 2015). Practically, each of the Be/XRB systems hosts a neutron star as the compact object with only one exception, MWC 656, which hosts a black hole and is the only known BH-Be/XRB system yet (Casares et al., 2014). The optical companion in Be/XRBs is a Be star (with typical mass in the range of 8 to 20 $M_{\odot}$), which shows emission lines in its optical and infrared spectra. The presence of circumstellar disk around the Be star is believed to be the cause of observed emission lines (Porter & Rivinius 2003; Slettebak 1988). Most of these Be/XRB systems are recurrent X-ray transients, which become detectable only after the mass transfer from the Be circumstellar disk to the compact object (see section 1.3.3 for the properties of Be/XRBs).

For the sake of completeness, it should be mentioned that there exists a third class of HMXBs apart from the SGXBs and Be/XRBs, i.e., Wolf-Rayet X-ray binaries (WRXBs). A total of seven WRXBs are known. Among them, only Cyg X-3 resides in our Galaxy (Esposito et al. (2015) and references therein). A detailed discussion on the properties and evolution of WRXBs is given in van den Heuvel et al. (2017), while a brief overview of the evolution theories for HMXBs are described below.

A pioneering work on the formation and evolution of the HMXBs was done by van den Heuvel & Heise (1972) and the basic model is depicted in Figure 1.1. According to the theory, initially the massive (primary) member of the binary system evolves and transfers a large fraction of its mass to the other member (secondary) of the binary system. The primary star will finally explode into a supernova to form either a neutron star or a black hole at its center, depending upon its initial mass. By this time, a strong mass inversion has occurred

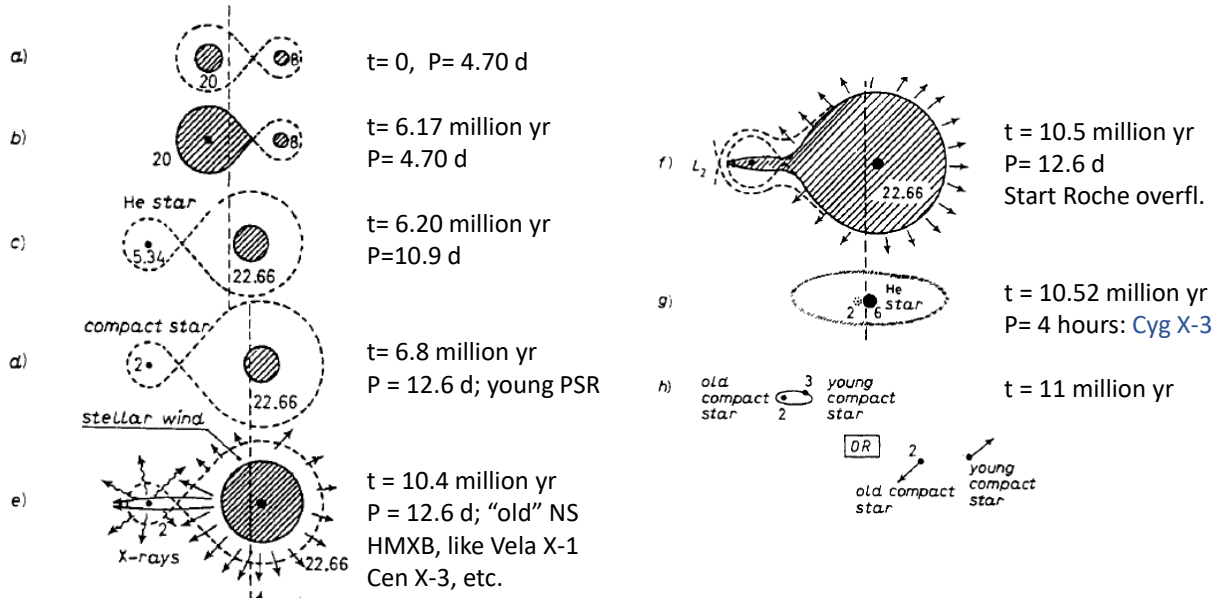

Figure 1.1: A possible evolutionary scheme for HMXBs leading towards forming an SGXB system. The figure is adopted from van den Heuvel (1976).

and the secondary member became the massive component of the binary (Figure 1.1, panel-d). According to the Virial theorem, the binary system still remains undisrupted if less than half of the total mass of the system was ejected during the supernova explosion (Blaauw, 1961). The newly formed compact object receives a birth-kick (probably due to the asymmetry in explosion), which tends to alter the orbit of the binary. At this point (assuming that the binary is still intact after supernova explosion), the HMXB system could be detected in X-rays, as the compact object started to accrete from the stellar wind of the massive companion (Figure 1.1, panel e-f). As pointed out by Paczynskii (1976), this second episode of mass transfer could soon run out and become unstable if the the mass ratio (q) of the compact star and the donor is < 0.3 (see Pavlovskii et al. (2017) for the calculations of q). On the other hand, if stable Roche-lobe overflow occurs, the binary will end up into a system of double compact objects.

1.2.2 Low Mass X-ray Binaries (LMXBs)

This class of X-ray binaries typically consists of a low mass companion star (<1 $M_{\odot}$, usually K or M spectral type) along with a compact object which could either be a black hole or a neutron star. As opposed to HMXBs, the orbital period of LMXBs are rather short i.e., usually within a few hours. Since the low mass companion star does not have strong stellar wind (unlike HMXBs), the mass accretion from the donor star to the compact object mainly takes place via Roche-lobe overflow (see section 1.3.1), effectively forming an accretion disc around the compact star. Consequently, the optical spectra of the LMXBs are usually dominated by the reprocessed X-ray emission from the accretion disk around the compact objects (van Paradijs & McClintock, 1994). The population census of X-ray binaries in our Galaxy shows that the LMXBs are more abundant as compared to the HMXBs (Liu et al., 2007). This is not a mere coincidence, rather a selection effect i.e., they have longer evolutionary time scales ($\geq 10^9$ yr) as compared to the HMXBs ($\leq 5 \times 10^6$ yr). If the compact object in the LXMB is a neutron star, the evolutionary time scales play a major role in decaying down its magnetic field significantly till $\sim 10^8$ G (Bhattacharya, 1995). As a consequence of weak magnetic field and in turn the ineffective channeling of matter onto the magnetic poles, most of the neutron star in LMXBs do not show X-ray pulsations. However, there exist a subgroup of LMXBs which indeed show X-ray pulsations at the time scale of milliseconds, known as accreting millisecond X-ray pulsars (AMXPs). The magnetic field of these AMXPs lies is in the range of 10^{8-10}G (Patruno & Watts, 2012). The LMXBs exhibit several interesting observational features such as quasi-periodic oscillations (QPOs, see section 2.5.1 of Chapter 2), thermo nuclear bursts (i.e., unstable burning of matter accumulated on the surface of the neutron star), X-ray outbursts (common explanations include changes in accretion rate or accretion instability; Lewin et al. 1993) and burst oscillations in some sources. These features could help to distinguish between the type of compact object present in the LMXB system and are widely discussed in literature (Lewin et al. 1997; Lattimer 2007). Moreover, as opposed to HMXB systems, understanding of the origin and evolution of the LMXB systems is not

very clear. A possible evolutionary scenario was suggested by Henrichs & van den Heuvel (1983), discussing the evolution of HMXB system with an extreme mass ratio (of the binary members) into an LMXB system via the common-envelope (CE) evolution scenario.

1.3 Accretion: Modes and mechanism

As pointed out earlier, mass accretion has been recognized as the most efficient form of energy production mechanism, responsible for the high energy emission from XRBs (Zeldovich & Guseynov, 1966). For a comparison, the maximum amount of energy that could be extracted during the nuclear fusion reactions (by fusing hydrogen into helium) is $\sim 6 \times 10^{18}$ erg g^{-1}. On the other hand, the amount of energy released by accretion of about 1 gram of matter onto a compact object with mass $\sim$1.4 M$_\odot$ and radius $\sim$10 km (parameters for a canonical neutron star) is $\sim 10^{20}$ erg. This is about 20 times more efficient than the nuclear fusion yield (Frank et al., 2002). The total amount of energy released (per unit time) during the process of accretion, called accretion luminosity (L$_{acc}$), is given by:

$$L_{acc} = \frac{GM\dot{m}}{R} \tag{1.1}$$

where G is the gravitational constant, M is the mass of compact object, R is its radius and $\dot{m}$ is the mass accretion rate. From Equation 1.1, it is evident that the L$_{acc}$ basically depends upon the mass accretion rate ($\dot{m}$) and compactness parameter (M/R). This implies that the accretion luminosity is much higher in case of black holes and far less efficient in case of white dwarfs with mass $\sim$1 M$_\odot$ and radius $\sim 10^4$ km.

The process of mass accretion basically converts the gravitational potential energy of accreted material into the kinetic energy, which gets radiated thermally (predominantly in X-ray regime) by following the impact on the surface of compact object (in case of neutron star and white dwarfs). Therefore, understanding of the gravitational potential surfaces of both the stars in the binary system is of utmost importance. The trajectory of a test particle

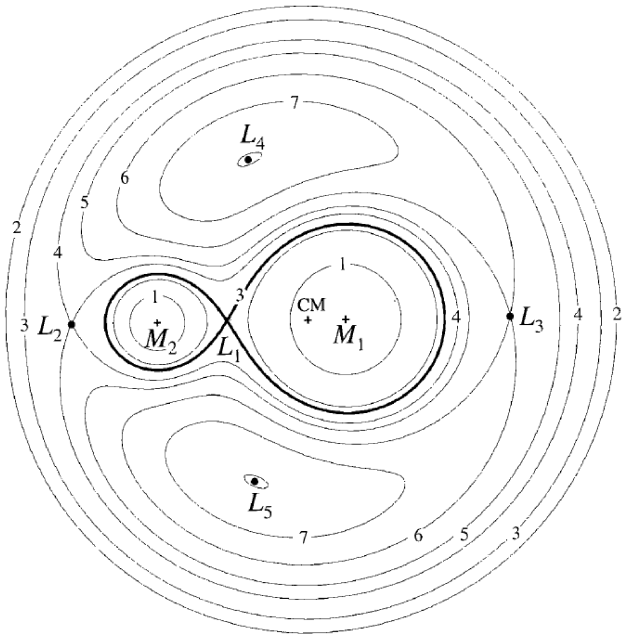

Figure 1.2: The equipotential surfaces (Φ_R = constant) for a binary system with mass ratio of 0.25 (see text). The figure is adapted from Frank et al. (2002).

with mass m, at a position r, around the binary system could be approximated by the *Roche potential* which can be expressed as:

$$\Phi_R = -\frac{GM_1}{\mid r - r_1 \mid} - \frac{GM_2}{\mid r - r_2 \mid} - \frac{1}{2}(\Omega \times r)^2 \tag{1.2}$$

where M_1, r_1 and M_2, r_2 are the masses and positional vectors of the individual stars of the binary system, respectively. While the angular momentum Ω, is expressed as:

$$\Omega = e\sqrt{\frac{GM_1}{a^3(M_1 + M_2)}} \tag{1.3}$$

where, a is the binary separation and e is the unit vector normal to the orbital plane of the binary system. The first two terms in Equation 1.2 represent the gravitational potential of individual stars acting on the test particle. The third term in the equation arises due to the binary rotation and represents the centrifugal potential. Figure 1.2 shows several equipotential surfaces of a binary system with mass ratio (M_2/M_1) of 0.25.

The Roche potential has its extrema (either maxima or minima) or in other words, the net force acting on the test particle is zero at the *Lagrangian* points, labeled L_1 to L_5 (Figure 1.2).

L_1 represents the first or inner Lagrangian point, where the gravitational forces of both the stars are balanced out. While at L_2 and L_3, the centrifugal forces cancel the summed gravitational potential due to both the stars. The other two Lagrangian points i.e. L_4 and L_5 are located perpendicular to the binary orbital plane and represent the global maxima (unstable points). During the process of evolution, the companion star overfills its Roche-lobe and the matter becomes free to fall under the gravitational potential of other star (compact object in the binary system). This matter gets accreted onto the compact object through the inner Lagrangian point L_1. This kind of mass transfer mechanism is known as Roche-lobe overflow and is described in the following section in detail.

1.3.1 Roche-lobe overflow and disk accretion

As mentioned in Section 1.2.2, the Roche-lobe overflow is a dominant mode of mass transfer mechanism for LMXBs, where the mass donor or companion star does not have strong stellar wind. Since the compact object and the companion star in the binary system orbit around the common center of mass, matter escaping through the inner Lagrangian point carries a significant amount of angular momentum. This forbids the material to fall directly onto the compact object, rather it starts to encircle the accreting object in circular orbits (due to the conservation of angular momentum) and in the process, an accretion disk is formed around the compact object. If the compact object is a neutron star, the accretion dynamics is mainly governed by its spin and magnetic field (see Section 1.7, the pulsar magnetosphere). However, in case of black holes (with no hard surface; unlike neutron stars), a fraction of gravitational potential energy of accreted matter is dissipated via viscosity in the stable accretion disk (Shakura & Sunyaev, 1973), resulting in emitting radiation in multi-wavelength range such as optical, infrared, UV and X-ray bands. But the dominant contribution in X-rays comes from the presence of a hot corona (electron plasma) above the accretion disk and/or black hole (Haardt & Maraschi, 1991). In this hot corona, the low energy photons, originated from the accretion disk, get inverse Compton scattered and ejected as high energy photons. These

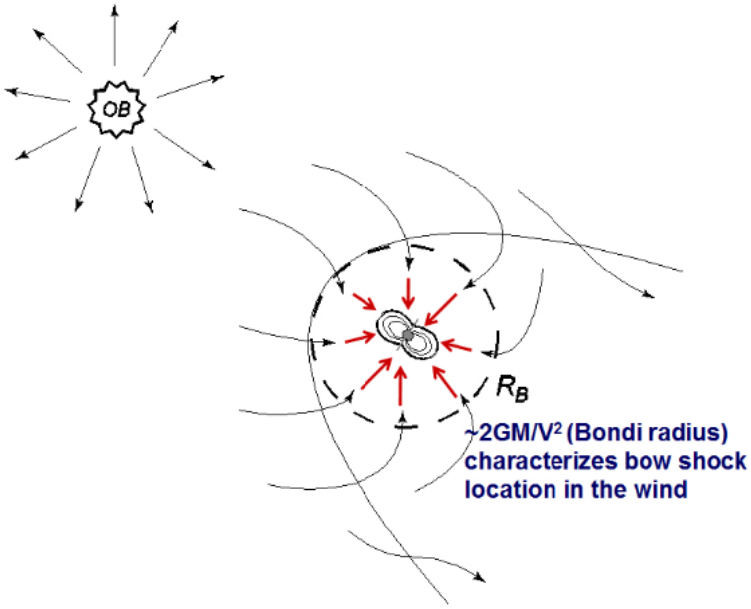

Figure 1.3: Schematic depiction of stellar wind accretion in HMXBs. The compact object shown here is a neutron star which is accreting matter from the supersonic wind of the OB optical companion i.e., Bondi-Hoyle-Lyttleton accretion. Image is adapted from Shakura et al. (2015).

high energy photons are described with non-thermal power-law continuum model.

Irrespective of the type of compact object, the accretion disk could be formed, provided that the angular momentum of the accreted material is sufficient and the circularization radius is greater than the radius of compact object. The circularization radius (R_{cir}) basically marks the distance from where the accretion disk starts to build up and is mathematically expressed as:

$$R_{cir} = \frac{J^2}{GM_X} \tag{1.4}$$

where J is the specific angular momentum[1] of the accreting material and M_X is the mass of accreting object (Pringle, 1981). Apart from the Roche-lobe overflow, two other types of mass transfer mechanism exist (particularly relevant for HMXBs) and are described in the following sections.

[1]The specific angular momentum of accreted material in this case is approximately equals to that of a flat circular disc of radius r_{acc}, rotating with angular velocity ω i.e., $J \sim 1/4\ r^2_{acc}\omega$ (see also Frank et al. 2002).

1.3.2 Wind accretion

As mentioned in Section 1.2.1, the optical companion in a HMXB is a massive star of O-B spectral type with a typical mass loss rate of about 10^{-6}-10^{-5} $M_\odot$ yr^{-1} (Puls et al., 2008). Due to such high mass loss rate, the companion star throws off matter from its surface in the form of stellar wind even before completely filling its Roche-lobe. This stellar wind is highly supersonic in nature (i.e. greatly exceeds the sound speed) which is often comparable to the escape velocity from the stellar surface. The expression for wind velocity can be written as

$$v_{wind} \approx v_{esc} = \left(\frac{2GM_c}{R_c}\right)^{1/2} \tag{1.5}$$

where M_c and R_c are the mass and radius of the companion star, respectively. While orbiting around its companion, the compact object (usually a neutron star) captures a fraction of this wind and gets powered in X-rays. However due to inhomogeneous mass accretion and insufficient angular momentum in most cases, the formation of an accretion disk in wind-fed systems is quite rare (Petterson, 1978). Consequently, the matter distribution (around the compact object) in this case is isotropic which leads to quasi-spherical accretion (Davidson & Ostriker, 1973). In this scenario, a bow shock is expected to form around the compact object (due to the interaction between compact object and supersonic wind). The characteristic distance of location of the bow shock (see Figure 1.3), is known as *Bondi radius,* R_B (Bondi & Hoyle, 1944) (more commonly known as *accretion radius* r_{acc}) and can be calculated as:

$$R_B = \frac{2GM_X}{v_{rel}^2} \tag{1.6}$$

where M_X is the mass of compact object and v_{rel} is its relative velocity w.r.t the wind velocity and is given by:

$$v_{rel} = (v_{Xorb}^2 + v_{wind}^2)^{1/2} \tag{1.7}$$

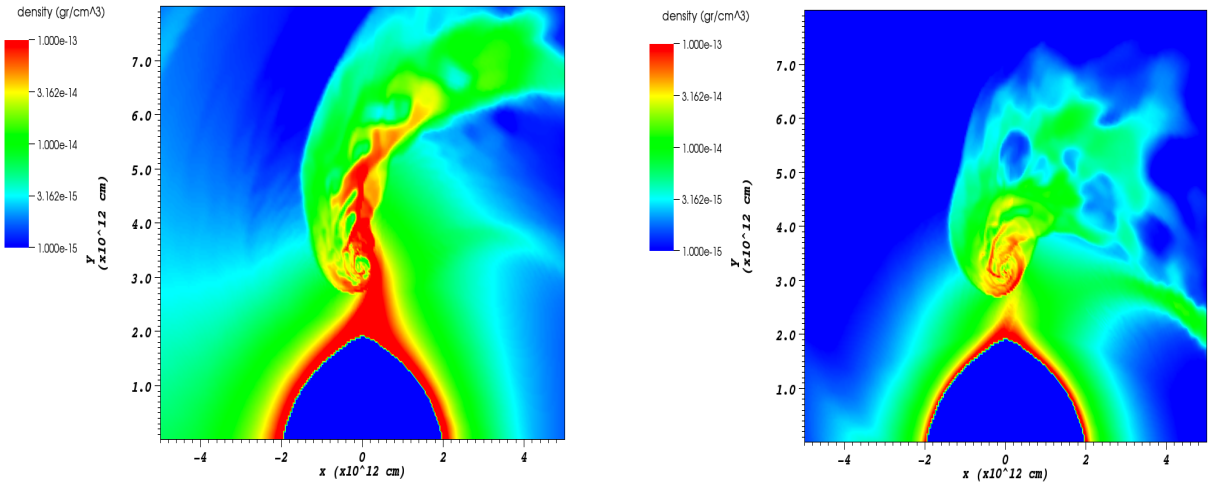

Figure 1.4: MHD simulation of the stellar wind structure around a neutron star in an HMXB. The figure is taken from Manousakis et al. (2012) and the mass loss rate of the companion star is assumed to be 2 $\times$ 10^{-7} $M_{\odot}$ yr^{-1}. Left Panel: The accretion wake structure, when a wind velocity of 500 km s^{-1} is considered. Right Panel: The accretion wake structure, when a higher wind velocity i.e., 1200 km s^{-1} is considered.

where v^2_{Xorb} is the orbital velocity of the compact object ($\sim$150 km s^{-1}), which is negligible as compared to the wind velocity ($\sim$1500 km s^{-1}). If we plug in the value of v_{rel} in Equation 1.6, we get the Bondi radius to be in the order of $\sim 10^{10}$ cm. Furthermore, by using above equations, it is possible to calculate the amount of matter accreted by the compact object i.e., by equating the mass flux at Bondi radius with the total mass loss rate of the companion (see Frank et al. 2002). It comes out to be in the order of $\sim 10^{-4}$ times the total mass loss rate of the companion. This indicates that the wind accretion is a quite ineffective mode of mass transfer as compared to the disk accretion (Roche-lobe overflow), where the entire outer envelope of companion is transfered to the compact object. However, due to the high mass loss rate of the companion star, a sustainable mass accretion is possible in these systems. As a consequence, these systems were the first ones to be detected, for example Cen X-3 (Giacconi et al., 1971).

By analyzing several wind accreting XRBs, Sako et al. (2003) first proposed that the stellar wind in these systems is highly structured in the form of "clumps". The evidence of clumpy wind has also been found in many wind accreting XRBs such as Vela X-1 (Kreykenbohm et al. 2008; Fürst et al. 2010), 4U 1700-371 (Jaisawal & Naik, 2015), OAO 1657-415 (Jaisawal &

Naik, 2014) and GX 301-2 (Islam & Paul, 2014). Apart from clumpiness of the wind, several other interesting structures are also observed in these systems. If the mass accretion rate is high, the resulting X-ray radiation is able to ionize the wind in the vicinity of the neutron star. This wind consequently, slows down in a sphere of ionized material around the neutron star, known as Strömgren sphere. The matter gets accumulated at the boundary of this spherical structure and a bow shock is formed, which together with the movement of neutron star along the binary orbit, form an elongated stream (with enhanced wind density) known as"accretion wake" (see Blondin et al. 1990). Recently, Manousakis et al. (2012) performed a detailed MHD simulations to reveal the complex structure of the accretion wake (see Figure 1.4).

1.3.3 Accretion through Be circumstellar disk

Be/X-ray binaries (Be/XRBs) represent the major sub-class of HMXBs and are the focus of present thesis work. Almost all of these systems consist of a neutron star as the compact object and a non-supergiant optical companion with spectral type Oe or Be. As opposed to the classical B-type stars which show absorption lines in their optical/infrared spectra, the Be stars rather show strong Balmer *emission* lines (hence the qualifier 'e'). Apart from the emission lines, another characteristic feature of Be stars is the presence of excess emission in its infrared spectrum, known as infrared excess. These properties of Be stars have been associated with the presence of extended envelope of ionized material surrounding the equatorial plane of the B-type star i.e., a circumstellar disk (see Figure 1.5). However, the formation of disk around the Be star has remained elusive. Possible explanations evoke the high rotational velocities of these stars $v_{rot} \approx 250$ km s^{-1} i.e., close to the critical or 70% of break-up velocities[2] (Porter 1996; Townsend et al. 2004), leading to the formation of a viscous disk or magnetically confined stellar wind (Rivinius et al., 2013).

The neutron star in Be/XRB system revolves in a wide and eccentric orbit (e $\geq$ 0.3) around its companion and has an orbital period of more than 15 days. As a consequence,

[2]Critical or break-up velocity of a star is defined as the velocity at which the centrifugal forces at the equator is just balanced by its gravitational forces such that above this rotational velocity, star ceases to hold up.

it spends most of the time far away from the companion star and does not show any X-ray activity and remains in quiescence. However, once it passes close to the Be star (at periastron), mass accretion from Be disk becomes possible and the neutron star accretes matter from the circumstellar disk and show the so called 'Type-I' X-ray outburst (see Figure 1.5). These outbursts are highly periodic in nature i.e., coincident with the periastron passage of the neutron star and lasts a small fraction of the orbital period ($\sim$ 20-30% of the orbital period). The X-ray luminosity during these events reaches as high as 10-100 times the quiescent luminosity ($L_{quiescent} \approx 10^{34}$ erg s^{-1}; Stella et al. 1986). Occasionally, the neutron star in Be/XRB systems shows another kind of X-ray enhancement, known as 'Type-II' outbursts. The X-ray luminosity during the Type-II outburst events can reach as high as 1000 times the quiescent luminosity (or may even exceed the Eddington luminosity[3] of a neutron star), due to which they are often called 'giant' outbursts. Unlike Type-I outbursts, the Type-II outbursts are not associated with the orbital period and are extremely rare and random in terms of their occurrence (Negueruela, 2007). These giant outburst events could even last more than a complete orbital period of the binary i.e., spanning over a few weeks to months.

erg s^{-1}.

The determining factor behind the occurrence and absence of Type-I X-ray outbursts is believed to be the evolution of the circumstellar disk of Be star. Okazaki & Negueruela (2001) investigated the effect of neutron star's gravitational field on the size (extent) of Be disk and found that the Be disk gets tidally truncated at specific radii, known as resonance radii. They argued that if the Roche radius of companion star lies within the resonance radii, the neutron star is allowed to accrete matter during the periastron passage (Okazaki & Negueruela, 2001). Some of the Be/XRB systems showing regular Type-I activity includes GRO J1008-57 (Coe et al., 2007) and EXO 2030+375 (Taam et al. 1988; Parmar et al. 1989a,b; Reynolds et al. 1993; Epili et al. 2017). On the other hand, the actual reason behind the occurrence of Type-II

[3]The Eddington luminosity L_{Edd} sets an upper limit to the maximum luminosity for a spherically emitting body, given that the radiation force acting on an electron-proton pair, balances the gravity. Assuming the case of spherical accretion on to the surface of neutron star, L_{Edd} is given by: $4\pi GM\ m_p c/\sigma_T = 1.3 \times 10^{38}\ M/M_\odot$

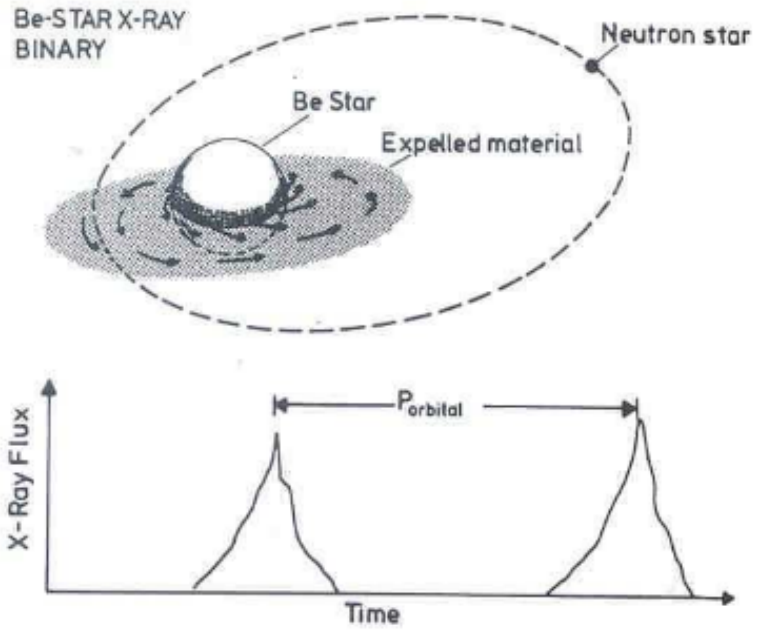

Figure 1.5: Schematic depiction of a Be/X-ray binary system. The neutron star accretes matter from the circumstellar disk of its Be companion (see text) and shows Type-I X-ray outburst. Type-I outbursts are periodic in nature and coincides with the periastron passage of the neutron star (see the bottom panel of this figure). Image credit: van den Heuvel (2004).

outburst is still not clear. Possible explanations include the increase in activity of companion star (Coe, 2000) or the presence of inclined Be disk (with respect to orbital plane; Okazaki et al. 2013). Irrespective of the outburst type, the accreted matter is expected to form an accretion disk around the neutron star. Observational evidence on the formation of accretion disk comes from the detection of strong spin-up episodes during the giant outburst events of Be/XRBs. Since the accretion disk tends to exert a torque on the rotating neutron star, thus increasing its spin frequency (Ghosh & Lamb, 1979). Also, Quasi Periodic Oscillations (QPOs) have been detected in several Be/XRBs, which are believed to be associated with the motion of inhomogeneous matter in the inner edge of the accretion disk (see Chapter-2, Section 2.5.1 for the discussion on QPOs).

Apart from the above mentioned transient activities like Type-I and Type-II X-ray outbursts, some Be/XRBs are persistent emitters with low X-ray luminosities of $\sim 10^{34}$ erg s^{-1}. At present, X Persei and LS+61°235 represent such kind of Be/XRB systems (Negueruela, 1998). As compared to transient Be/XRBs, the neutron stars in these persistent systems have longer orbital periods and rotate rather slowly. Therefore, due to the wider orbits, the neu-

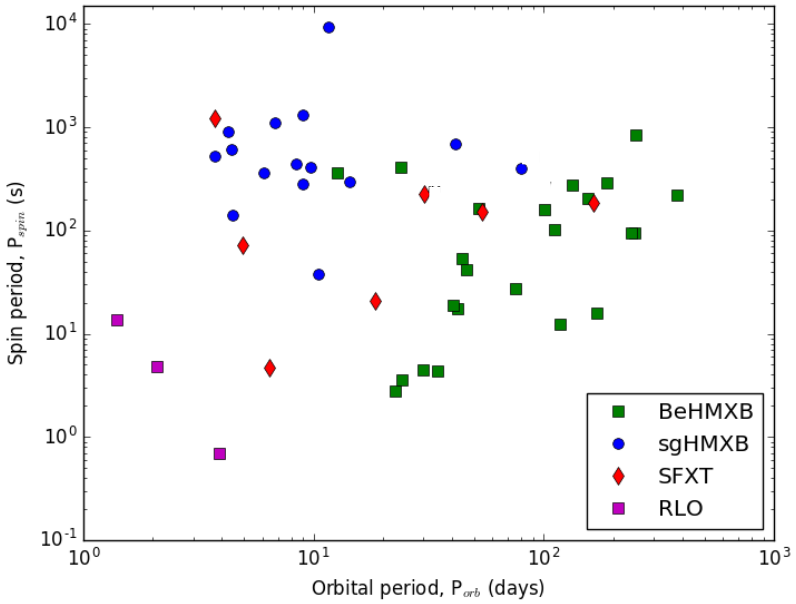

Figure 1.6: Corbet diagram : Plot between the spin and orbital periods of neutron star HMXBs. Different population of HMXBs (as described in section 1.2.1) gets clustered in different regions in this plot. The Be/XRB population shows positive correlation, disk-fed SGXBs (RLO) show negative correlation, while the wind fed SGXBs and SFXTs show no correlation at all. Figure adapted from Chaty et al. (2019).

tron star in these systems are expected to accrete from the outer regions of the circumstellar disk (which have low matter density as compared to inner regions of the disk). This could possibly explain the low luminosity observed from these systems. Interestingly, the spin and orbital periods of all Be/XRB systems show a positive correlation on the Corbet diagram (see Figure 1.6; Corbet 1986). The reason behind this positive correlation is believed to be a limiting condition (during the episodes of accretion) when the radius of pulsar magnetosphere (Alfvén radius; r_A) becomes comparable to the corotation radius (r_{co}), i.e. $r_m \approx r_{co}$ (discussed in the following section; Corbet 1986).

1.4 Accretion powered X-ray pulsars

The accretion powered X-ray pulsars are basically the rotating neutron stars in binary systems in which both the components orbit around the common center of mass. Due to the misalignment between the spin and magnetic axes, the beam of radiation (in X-ray band) from the magnetic poles of the neutron star can be detected once it sweeps through the line

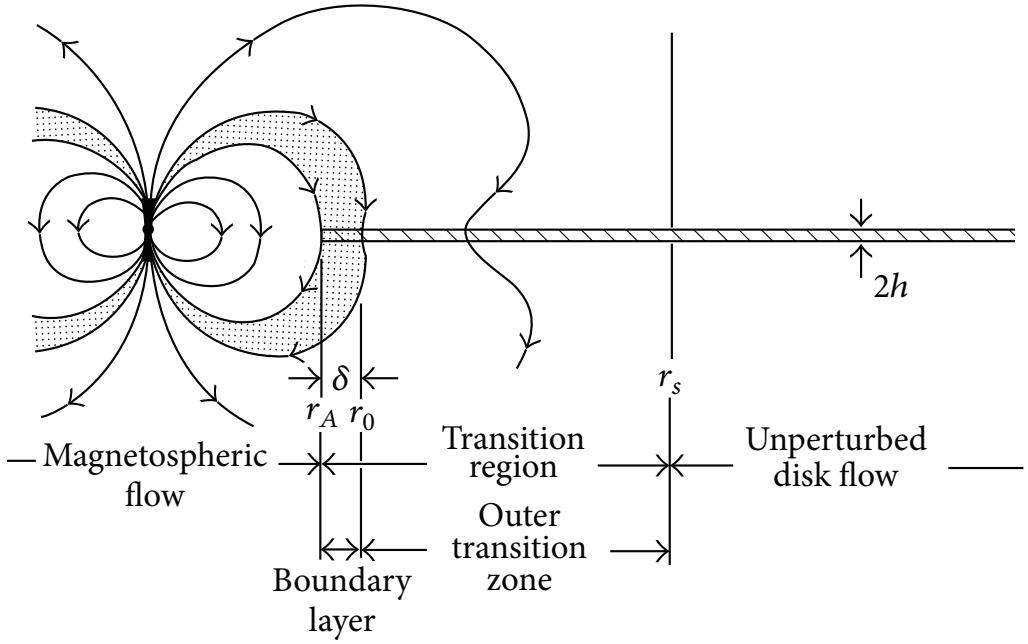

Figure 1.7: Schematic depiction of pulsar magnetosphere, showing the interaction of strong magnetic field with the accreting plasma. Figure has been adapted from Ghosh & Lamb (1979).

of the sight of observer. Hence, the observed X-ray emission (powered via the accretion of matter from the companion star; see Section 1.5) from the neutron star appears to be pulsating. The neutron star in these systems are relatively young and posses strong magnetic fields of the order of $\sim 10^{12}$ G. Apart from the extreme magnetic field, the density of a neutron stars ($\sim 10^{14}$g cm^{-3}) is as high as that of nuclear matter. These aspects make them one of the most exotic objects in the universe. Therefore, study of the accretion mechanism in these systems, provide us with the opportunity to probe the properties of matter under extreme conditions, which otherwise is impossible to achieve through laboratory experiments.

In previous sections, different modes of accretion processes were summarized. However, once the matter reaches close to the surface of neutron star, its journey is completely governed by the magnetosphere. Therefore, it is important to look closely into the magnetic field regime of the accretion powered X-ray pulsars. At this point, it is worth to emphasize that the actual geometry of the pulsar magnetosphere is extremely complex and depends upon the manner in which the accreting plasma interact with the magnetic field of the pulsar. However, it is still possible to have a rough estimation of the size of the magnetosphere i.e, by equating

the ram pressure (P_{ram}) of infalling plasma with the magnetic pressure (P_{mag}) asserted on it. The distance (from the surface of NS) where these two competing forces balance each other is known as the *Alfvén radius* (r_A; see Figure 1.4) or magnetospheric radius (Lamb et al., 1973). Now, by starting with a simple approximation of dipolar field, the strength of magnetic field varies with the radial distance (r) as:

$$B(r) \approx \frac{\mu}{r^3} \tag{1.8}$$

where μ is the magnetic dipole moment of the neutron star. The magnetic pressure thus can be expressed as:

$$P_{mag} = \frac{B^2}{8\pi} \approx \frac{\mu^2}{8\pi r^6} \tag{1.9}$$

Corresponding ram pressure P_{ram} of the infalling plasma is given by $\rho\ v^2$, where v is the infall velocity and is comparable to the free fall velocity (v_{ff}= $(2GM/r)^{1/2}$). For steady state accretion, the mass accretion rate is $\dot{m}$= $4\pi\rho v r^2$. Therefore, P_{ram} is given by:

$$P_{ram} = \left(\frac{\dot{m}}{4\pi r^2}\right)\sqrt{\frac{2GM}{r}} \tag{1.10}$$

By equating above expressions 1.9 and 1.10, we can derive the expression for Alfvén radius (r_A) in terms of the mass accretion rate ($\dot{m}$) as:

$$r_A = 5.1 \times 10^8 \dot{m}^{-2/7} M^{-1/7} \mu^{4/7} \quad cm \tag{1.11}$$

where M is the mass of neutron star expressed in units of $M_\odot$, $\dot{m}$ is expressed in units of 10^{16} g s^{-1} (hereafter $\dot{m}_{16}$) and μ is expressed in units of 10^{30} G cm^3 (hereafter μ_{30}). This expression could finally be expressed in terms of accretion luminosity (by substituting Equation 1.1 in above expression) as:

$$r_A = 2.9 \times 10^8 M^{1/7} R_6^{-2/7} \mu_{30}^{4/7} L_{37}^{-2/7} \quad cm \tag{1.12}$$

where R_6 is the radius of neutron star expressed in units of 10^6 cm and L_{37} is the luminosity

in 10^{37} erg s^{-1}. However, the expression for for Alfvén radius (r_A), given in equations 1.11 and 1.12 holds in the case of spherically symmetric homogeneous flow. However, in the case of disk accretion, the Alfvén radius is given by $R_A = 0.5 \times r_A$ (Frank et al., 2002). Apart from the magnetospheric radius (r_A), two other characteristic radii i.e., *accretion radius* (r_{acc}; see Equation 1.6 in Section 1.3.2) and *corotation radius* (r_{co}) are important to understand the dynamics of pulsar magnetosphere.

The corotation radius (r_{co}) is defined as the distance at which the angular velocity of the magnetosphere (ω) matches with the angular velocity of the Keplarian disk i.e, $\sqrt{\frac{2GM}{r^3}}$. It could also be described as the radius at which the centrifugal force due to the rotating pulsar balances the gravity. The corotation radius could thus be expressed as:

$$r_{co} = \left(\frac{2GM}{\omega^2}\right)^{1/3} = 1.5 \times 10^8 M^{1/3} P_{spin}^{2/3} \quad cm \tag{1.13}$$

where, P_{spin} is the spin period of the pulsar (which changes during the outburst events in case of Be/XRB pulsars). It is clearly evident from Equations 1.6, 1.11, and 1.13 that these radii are not constants, rather a function of relative wind velocity (as ${v_{rel}}^{-2}$), mass accretion rate (as $\dot{m}^{-2/7}$) and spin period (as ${P_{spin}}^{2/3}$), respectively. Therefore, depending upon the interplay between these three characteristic radii, four regimes of the pulsar accretion are established (Davidson & Ostriker 1973; Stella et al. 1986). Three of these regimes, relevant to the present discussion are described below. While the fourth one describes the situation where the pulsar is young and rotates too quickly ($P_{spin} << 1$ s), so it will not be discussed further.

- `Regime I` : When the following condition is satisfied: $r_{acc} > r_A$ and $r_{co} > r_A$. The captured matter at r_{acc} falls inwards till r_A and enters into the pulsar magnetosphere. The channeling of this matter onto the magnetic poles along the magnetic field lines, forms an accretion column (see Section 1.8) which then radiates in X-rays. Therefore this regime is referred as 'accretion regime'.

- `Regime II` : When the following condition is satisfied: $r_{acc} > r_A > r_{co}$. During the outburst (i.e. when accretion rate is high), the ram pressure is strong enough to keep r_A within r_{co}. However, once the accretion rate decreases (when the pulsar moves away from the periastron, in case of Be/XRB systems), the r_A is allowed to expand. Once it grows beyond r_{co}, the centrifugal force arises which inhibits the matter to enter into the pulsar magnetosphere. This result into the cessation of pulsation and this is known as the 'propeller effect' (Lamb et al. 1973; Illarionov & Sunyaev 1975). Moreover, as mentioned in Section 1.3.3, the limiting condition for accretion is when $r_A = r_{co}$. Therefore, the limiting luminosity (i.e., the luminosity below which accretion is not possible) can be determined by equating the expressions given by Equations 1.13 and 1.12 as:

$$L_{acc}(min) = 2 \times 10^{37} k^{7/2} R_6^{-1} M^{-2/3} \mu_{30}^2 P_{spin}^{-7/3} \quad erg\ s^{-1} \tag{1.14}$$

  Here, k characterizes the mode of accretion and is calculated by $k = \mathrm{r}_A/\mathrm{r}_{acc}$ (typical value is 0.5 for disk accretion scenario; Ghosh & Lamb 1978). Below this value of L_{acc}, the pulsar tends to 'turn off' as a consequence of propulsion of matter describe above. Therefore, this regime is referred as 'propeller regime' or centrifugal inhibition of accretion. However, recent observational evidences point towards the accretion of matter even at extremely low mass accretion rates. Recently, Romanova et al. (2004) have performed MHD simulations to parametrize the disc-field interaction and the corresponding instabilities leading to episodic mass accretion during propeller regime (see also D'Angelo & Spruit 2010).

- `Regime III` : When the following condition is satisfied: $r_A > r_{acc}$ and $r_{co} > r_{acc}$. In this case, 'magnetic inhibition of accretion' may occur before centrifugal inhibition could come into the picture. As r_{acc} shrink below the magnetospheric radius r_A, very little amount of matter would be able to penetrate the pulsar magnetosphere. This happens as most of the matter would be deflected by the magnetosphere itself, similar to what happens during the interaction of solar wind with the terrestrial magnetosphere

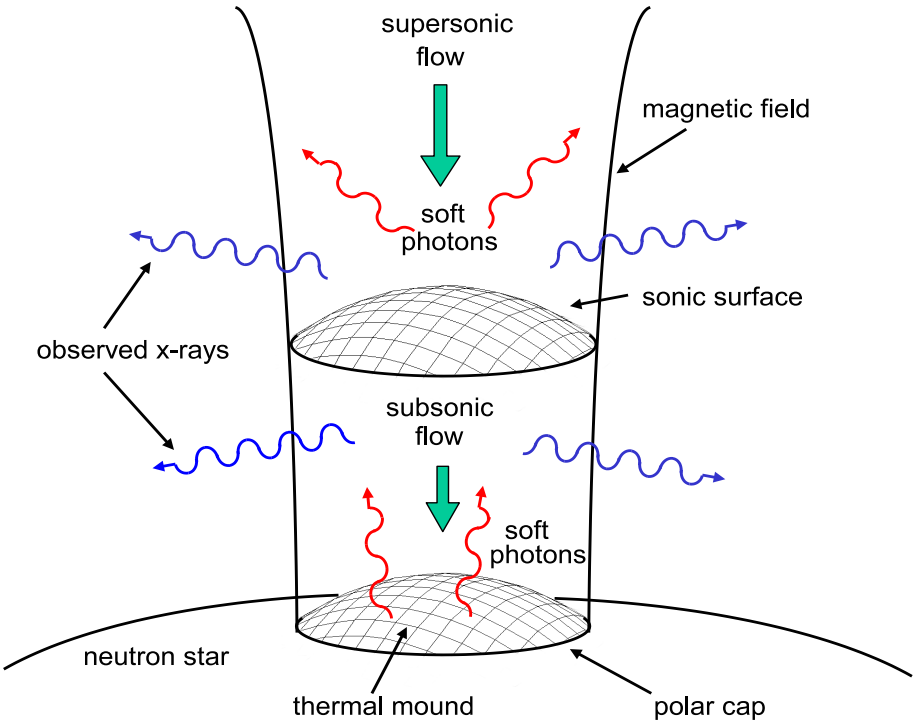

Figure 1.8: Schematic depiction of accretion column formed at the magnetic poles of accretion powered pulsars. The seed photons (red; see text for description) produced at the base of the column interacts with the accreting plasma and gets upscattered to higher energies via inverse Comptonization processes. The figure has bene adapted from Becker & Wolff (2007a).

(Illarionov & Sunyaev 1975; Stella et al. 1986).

1.5 Accretion Column

In accretion powered pulsars, irrespective of the mode of accretion (see Section 1.3), the fate of the accreted matter is mainly governed by the strong magnetic field ($\sim 10^{12}$ G) of the neutron star. Once the matter reaches at magnetospheric radius, it is forced to follow the field lines until it gets dumped onto the magnetic poles, forming an accretion mound. If the mass accretion rate is sufficiently high, the deposition of the accreted matter at the magnetic poles form a column like structure (see Figure 1.8), called the *accretion column*. As the accreted matter strikes the surface of the neutron star, its kinetic energy is converted into heat energy at the magnetic poles of the neutron star. The temperature at the poles reaches as high as 10^7 K, which is sufficient enough to emit in X-rays through blackbody radiation. However, the observed spectrum of X-ray pulsars is far more complicated than this simple

picture. The presence of hard X-ray flux (> 10 keV) points towards the non-thermal origin of the spectrum. Theoretical investigations have been carried out in past to comprehend the formation mechanism of pulsar spectrum. However, the previous atempts to compute the spectra of accretion powered X-ray pulsars, based upon the static or dynamic theoretical models, were not able to well describe the observed spectrum (Basko & Sunyaev 1976; Nagel 1981b,a; Meszaros & Nagel 1985a,b). Much of the current understanding about the emission mechanism in X-ray pulsars is based on the recent theoretical investigations by Becker & Wolff (2007a). They considered a cylindrical geometry of the accretion column to derive the analytical solution to the radiative transfer equation (RTE) of pulsars, which can be expressed as:

$$\begin{aligned} \frac{\partial f}{\partial t} + v\frac{\partial f}{\partial z} &= \frac{Q(z,\epsilon)}{\pi r_0^2} - \frac{f}{t_{\rm esc}} + \frac{n_e \overline{\sigma} c}{m_e c^2}\frac{1}{\epsilon^2}\frac{\partial}{\partial \epsilon}\left[\epsilon^4\left(f + kT_e\frac{\partial f}{\partial \epsilon}\right)\right] \\ &+ \frac{dv}{dz}\frac{\epsilon}{3}\frac{\partial f}{\partial \epsilon} + \frac{\partial}{\partial z}\left(\frac{c}{3n_e\sigma_{\parallel}}\frac{\partial f}{\partial z}\right) \end{aligned} \tag{1.15}$$

This equation describes photon distribution $f(z,\epsilon)$ in the emergent spectrum and is inseparable in energy (ϵ) and space (z; characterizes the height of accretion column). While the terms on the right hand side of this equation, in chronological order are described below.

- `The source of seed photons` Q`(`z`,`ϵ`):` Apart from the blackbody seed photons originating at the column base ($z = 0$; thermal mound), two other radiation mechanism could be considered in a crude approximation, which contributes to the population of seed photons in the accretion column i.e., Bremsstrahlung and Cyclotron processes. The Bremsstrahlung radiation (free-free emission) is produced due to the deflection of free electrons by the ions present in the infalling plasma. While the Cyclotron radiation results when the orbit of electron gets quantized into the Landau levels due to the presence of magnetic field. When the electron jumps from the higher to lower energy Landau level, a Cyclotron photon is emitted corresponding to the energy equal to the difference between these levels. These photons are also considered as seed photons.

- `The photon escape:` The second term on the right hand side of Equation 1.15 corresponds to the diffusion of X-ray photons, perpendicular to the direction of magnetic field (i.e. through the side walls of the accretion column; labeled as 'observed X-rays' in Figure 1.8). This process is characterized by the time scale t_{esc}, which in turn is a function of column radius (r_o) and optical thickness ($\tau_\perp$) of the accretion column perpendicular to the field lines ($t_{esc}(z) = r_o\ \tau_\perp/c$). Here, $\tau_\perp(z)$ is calculated as $n_e\ \sigma_\perp\ r_o$, where n_e is the number density of electrons and $\sigma_\perp$ is the angle averaged scattering cross section of photons perpendicular to the field lines (Becker & Wolff, 2007a).

- `Thermal Comptonization:` Thermal Comptonization is the process where seed photons (relatively cool) gets comptonized by the infalling thermal plasma (relatively hot). This thermal plasma is characterized by the optical depth τ and temperature kT_e. While propagating through the hot plasma, the seed photons suffer multiple scattering before leaving the accretion column. Since the typical electron temperature for accreting pulsars is low as compared to the average kinetic energy of the plasma, i.e. $kT_e << m_e c^2$, the contribution of thermal Comptonization is less (as compared to bulk Comptonization). However, it is extremely important to incorporate this term while solving the RTE as it has been able to successfully describe the typical cut-off observed in the spectrum of X-ray pulsars (Becker & Wolff 2005, 2007b). This cut-off like feature is originated due to the electron recoil (f in the third term of the right hand side of Equation 1.15) in the thermal plasma (Becker & Wolff, 2007a).

- `Bulk Comptonization:` The fourth term describes the contribution of bulk Comptonization. This originates due to the bulk motion of the plasma and basically describes the inverse Compton scattering of X-ray seed photons with relativistic electrons ($\sim$0.5 c). The bulk Comptonization is highly directional (unlike thermal Comptonization where the thermal motion of electrons is completely random) and is highly efficient[4] to upscatter the X-ray seed photons. A radiation dominated shock is expected to form in the accretion column during this interaction (Davidson & Ostriker 1973; Becker &

Wolff 2005). Consequently, the accreting plasma decelerates to subsonic velocities before setteling onto the poles of the neutron star.

- `Diffusion along the column:` This is similar to what described above for the photon escape term. This last term describes the scattering of X-ray photons ($\sigma_{\parallel}$) along the magnetic field lines but opposite to the bulk velocity of the plasma.

In order to solve the RTE given in equation 1.15, a steady state condition ($\partial f/\partial t = 0$) of pure and fully ionized hydrogen plasma was considered by Becker & Wolff (2007b). Moreover, these authors assumed a cylinderical symmetry, a constant magnetic field and temperature along the accretion columnn. For the computation of electron cross-sections, the bimodal treatment was considered i.e., modeling the scattering of photons propagating either parallel or perpendicular to the magnetic field. The analytical solutions of RTE, obtained by this approach, have been able to describe the spectrum of many bright pulsars qualitatively such as Her X-1, Cen X-3 and LMC X-4 (Becker & Wolff, 2007b). However, these analytical solutions are not yet able to describe the spectrum of X-ray pulsars with low luminosities. Recently, a significant improvement in the self consistent modeling of X-ray pulsars have been done by Farinelli et al. (2012). These authors have solved the RTE numerically, however its applicability is limited to the small number of observations yet. To sum up, these physically motivated spectral models are extremely complex, relatively new and still under development.

Despite the complexity of the physical processes involved, the shape of the continuum spectrum can easily be described with the phenomenological models like cut-off power law. Due to the lack of self consistent models to explain the pulsar spectrum, the phenomenological models have widely been used to describe the pulsar spectrum. The mathematical expression and the implementation of these phenomenological models are described in more detail in Section 2.6.1 of Chapter-2.

[4]The average increase in energy per collision is given by $\Delta E = \gamma^2$ E, where γ is the Lorentz factor of the relativistic electron.

1.5.1 Cyclotron resonance scattering features (CRSFs)

Apart from the continuum emission described above, the spectrum of several accreting X-ray pulsars additionally features Cyclotron Resonant Scattering Features (CRSFs) due to their strong magnetic field. These features are a manifestation of quantum electrodynamical process and have been observed in 10-100 keV range (Staubert et al., 2019). According to classical electrodynamics, an electron moving in the presence of magnetic field, will undertake a helical trajectory with the gyration radius (Larmour radius) expressed as:

$$r_L = \frac{m_e v_\perp}{Be} \tag{1.16}$$

This radius decreases with the increase in the strength of magnetic field. Once this radius r_L approaches the de Broglie wavelength (λ=h/m$_e$ v), the quantum mechanical effects starts to dominate. Consequently, the electron momentum $(p_\perp)^5$ (and hence energy) perpendicular to the direction of magnetic field becomes quantized into Landau levels. The X-ray photons while interacting with the relativistic plasma in the accretion column, undergo scattering processes with these electrons. The scattering cross section resonantly increases at the energies corresponding to the separation between these Landau levels (Lai 2001 and references therein) given by

$$E_n = \frac{m_e c^2}{\sin^2\theta}\left(\sqrt{1 + 2n\frac{B}{B_c}\sin^2\theta} - 1\right) \tag{1.17}$$

where θ is the angle between photon direction and magnetic field axis, B$_c$=m$_e{}^2$c^3/e$\hbar$ $\approx$4.4$\times$10^{13} G is the critical magnetic field i.e., the value of magnetic field where kinetic energy of electron matches its rest mass energy. Now, since the magnetic field of most of the pulsars is weaker as compared to the critical value i.e., B << B$_c$, we can therefore, calculate the Taylor approximation of equation 1.17 as

$$E_n = E_o + m_e c^2 n\frac{B}{B_c} \quad , \tag{1.18}$$

By plugging in the value of B_c in above equation, the cyclotron energy could be calculated as the difference between the two consecutive energy levels i.e., $E_{cycl} = E_{n+1} - E_n$,

$$E_{cycl} = 11.58\ keV \left(\frac{B_{NS}}{10^{12}G}\right) \tag{1.19}$$

For accreting X-ray pulsars, these discrete energy levels seemed to be equispaced with energy difference of E_{cycl}. Therefore, the X-ray photons with energies $n\ E_{cycl}$ could thus get absorbed and are missed from the line of sight of the observer. As a consequence, the absence of these photons is manifested as absorption features in the observed spectrum of the pulsar. From Equation 1.19, it is clear that the cyclotron line energy is directly proportional to the magnetic field strength of the pulsar. Therefore, detection of the CRSF in the pulsar spectrum is considered as a direct method to estimate the magnetic field of X-ray pulsars. Many efforts have been made to model these CRSFs through Monte Carlo Simulations (See Schwarm et al. (2017) and references therein). However, these models are still under development. Therefore, the CRSFs are widely described with the phenomenological models such as Gaussian (Lorentzian) absorption profile (see Section 2.6.2, Chapter-2).

1.5.2 Critical Luminosity and beam pattern

Previous sections were dedicated to summarize the radiation mechanism in accretion powered X-ray pulsars. However, the characteristics of this radiation depends upon the mass accretion rate $\dot{M}$ (and hence the luminosity). At low luminosities (low $\dot{M}$), the thermal mound formed at the surface of neutron star shapes the continuum spectrum. At higher luminosities, a radiation dominated shock front develops, which together with the accretion mound, shapes the spectral continuum via Comptonization processes. The concept of critical luminosity is thus introduced by Basko & Sunyaev (1976), in order to differentiate between these two possible scenarios. In other words, the critical luminosity is defined as the luminosity at

[5]While the electron momentum parallel to the magnetic field ($p_{\|}$) is continuous and could be interpreted as plasma temperature.

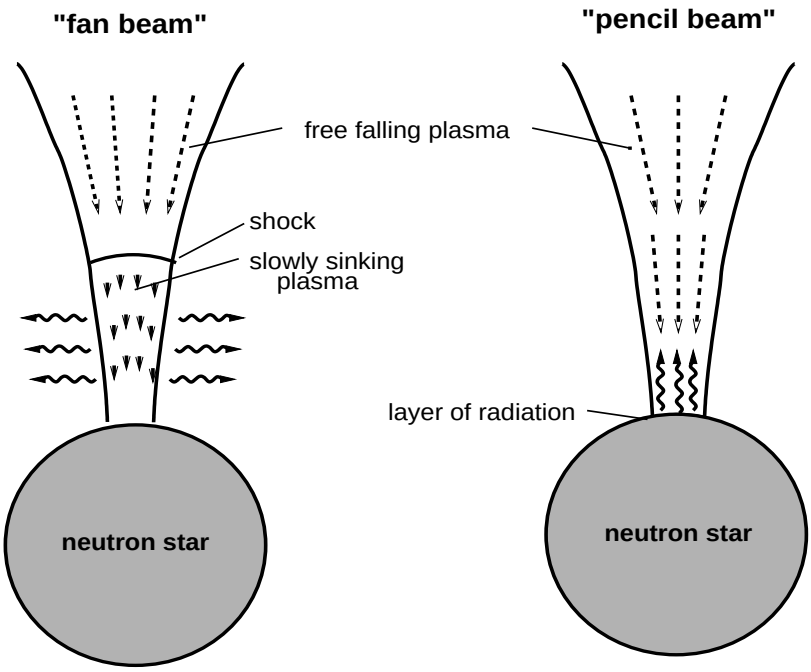

Figure 1.9: Schematic depiction of the formation of different kind of emission beam originating from the accretion column of the pulsar. Left panel shows fan beam pattern of emission when the luminosity of the pulsar is beyond the critical limit (see text). In this case, the radiation dominated shock front is developed and most of the photons diffuse through the sideways of the column below the shock region. Right panel shows the pencil beam pattern of emission when the mass accretion rate is low. Therefore, most of the photons propagate vertically along the magnetic field lines. The figure is taken from Schönherr et al. (2007).

which the radiation emanating from the surface of neutron star, is strong enough to stop the accreting material above the magnetic poles by forming a radiation dominated shock. The mathematical expression for critical luminosity, in terms of scattering cross section of X-ray photons, can be expressed as (Basko & Sunyaev 1976; Mushtukov et al. 2015) :

$$L_{crit} = 2.72 \times 10^{37} \left(\frac{\sigma_T}{\sqrt{\sigma_{\parallel}\sigma_{\perp}}} \right) \left(\frac{r_o}{R} \right) \left(\frac{M}{M_{\odot}} \right) \quad erg\ s^{-1} \tag{1.20}$$

where, r_o is the radius of polar cap, σ_T is the Thomson scattering cross section, $\sigma_{\parallel}$ and $\sigma_{\perp}$ are the angle averaged cross sections for the scattering of X-ray photons propagating parallel and perpendicular to the magnetic field respectively. Becker et al. (2012) calculated the scattering cross sections by considering the Comptonization processes and expressed the

critical luminosity in terms of the magnetic field of the pulsar as:

$$L_{crit} = 1.49 \times 10^{37} w^{-28/15} \left(\frac{\Lambda}{0.1}\right)^{-7/5} \left(\frac{M}{1.4M_{\odot}}\right)^{29/30} \left(\frac{R}{10km}\right)^{1/10} \left(\frac{B}{10^{12}G}\right)^{16/15} \quad erg\ s^{-1} \tag{1.21}$$

Here, w is the parameter which describes the shape of continuum spectrum and Λ characterizes the mode of accretion. Other parameters i.e., M, R and B are typical mass, radius and magnetic field strength of the neutron star, respectively. Therefore for standard neutron star parameters, above equation simplifies to:

$$L_{crit} = 1.49 \times 10^{37} \left(B_{12}\right)^{16/15} \quad erg\ s^{-1} \tag{1.22}$$

The luminosity of the pulsar below and above this critical luminosity, can thus be termed as sub-critical and super-critical luminosity, respectively. For the sources in sub-critical luminosity regime (L $\sim 10^{34}$–10^{35} erg/s i.e, $<<$L$_{crit}$), the accreting matter is brought to rest at the surface of neutron star via Coulomb interactions (Langer & Rappaport, 1982). In this situation, the radiation is emitted from the accretion mound formed at the base of the accretion column and most of the photons are emitted parallel to the direction of magnetic field in the form of 'pencil-beam' (see the right panel of Figure 1.9). However, in super-critical luminosity regime (L $\sim 10^{37}$–10^{38} erg/s i.e, $\geq$ L$_{crit}$), due to the development of radiation dominated shock above the surface of the neutron star, the accretion column becomes optically thick. Due to this, the parallel component of Thomson scattering cross section is drastically reduced as compared to the perpendicular one (i.e., $\sigma_{\parallel} << \sigma_{\perp}$; see also Mushtukov et al. 2015). As a result, most of the X-ray photons escape the accretion column through the side walls in the form of 'fan-beam' emission pattern (see left hand side of Figure 1.9). However, the decomposition of beam profiles into pencil and fan beam patterns, is a crude approximation and provides very little information about the intrinsic geometry and emission profile of the pulsar. In order to interpret the (observed) complex pulse profiles of the pulsars, theoretical efforts have been made in the past to reconstruct or model them (Kraus et al. 1996; Sasaki

et al. 2010). Recently, as pointed out by Kraus et al. (2003), the inclusion of general relativistic considerations and gravitational light bending effects in the modeling of pulse profiles may lead to even complex geometries and corresponding complex evolution with the photon energy.

1.6 Motivation and Objectives of the Thesis

The X-ray emission from the accreting pulsars are a result of the complex physical processes occurring in the vicinity of the surface of neutron stars. In particular, the accretion column at the magnetic poles of the neutron star acts as the primary source of X-ray emission. The X-ray photons emitted from the accretion column get reprocessed at various sites in the vicinity of the neutron star before reaching the observer. The observed data posses signatures of all the complex processes the photons have undergone before being collected at the detectors. The present thesis is dedicated to understand the emission mechanism in highly magnetized accreting X-ray pulsars. As pointed out in the previous section, the emission characteristics of this radiation depends upon the mass accretion rate and hence on the luminosity. Therefore, it is interesting to investigate the characteristic properties of such X-ray sources at different luminosities. For this kind of study, Be/X-ray binary pulsars are most suitable as they show a broad range of luminosity (spanning about four orders in magnitude from quiescence to outburst phases) and thereby offer a unique opportunity to study the X-ray variability (spectral and temporal) with luminosity. To accomplish the proposed research objectives, I have performed a comprehensive study of Be/XRP 2S 1417-627 across two giant outbursts, seperated by almost a decade in time. The major research objectives of our investigations in the present study are summarized below.

- To understand the spin period evolution of the Be/X-ray binary pulsars.
- To investigate the reason behind the changes in pulse profiles of the pulsar with luminosity and photon energy. Subsequently, attempting to infer the corresponding changes

in the accretion column geometry.

- To carry out a detailed pulse phase-averaged and phase-resolved spectroscopy analysis in order to probe the accretion environment around the pulsar i.e., how the physical parameters of the system changes with the pulsar rotation.

- To study the physical properties of the accretion column i.e., electron temperature in the plasma, density and optical depth of the emitting region. Until recently, various phenomenological models have been used widely to describe the pulsar spectrum. These models however are not adequate to provide any conclusive insights about the physical properties of the system. In the present work, we aim to investigate the emission mechanism by using recently developed physically motivated models to probe the physical properties of these systems.

- To investigate the nature and origin of soft X-ray excess emission (below $\sim$5 keV) seen in the spectrum of a few accreting pulsars.

1.7 Thesis Organization

The present chapter outlines the current understanding about the radiation processes in accretion powered X-ray pulsars, while rest of the thesis is organized as follows:

`Chapter-2:` This chapter provides an overview of various instruments onboard respective X-ray astronomical observatories, from which the data have been acquired to study the Be/X-ray binary system under investigation. It also offers a detailed explanation on the data reduction procedures, softwares used and a detailed description of timing and spectral methods utilized to carry out the present work.

`Chapter-3:` A detailed timing and spectral investigation has been carried out on Be/X-ray binary pulsar 2S 1417-624 during its 2009 giant outburst event, as observed with the *Rossi X-ray Timing Explorer (RXTE)* observatory. The pulse profiles of the pulsar shows complex evolution with the pulsar luminosity and photon energy. The cause of changes in the beam

pattern has been probed in detail using large number of observations carried out during the rising, as well as the declining phase of the giant X-ray outburst. This enabled us to carry out a detailed study of evolving pulse profile of the pulsar with luminosity. The broadband spectral study (3-70 keV) has also been carried out using phenomenological models. The evolution of spectral parameters with luminosity has been studied in detail and its implications are discussed in this chapter.

`Chapter-4:` This chapter is dedicated to develop an understanding about the physical processes contributing towards the formation of pulsar spectrum. For this, physically motivated self consistent working models have been implemented on the spectrum of pulsar 2S 1417-624 obtained during its rather recent giant X-ray outburst in 2018, observed simultaneously with *NuSTAR* and *Swift* observatories. For the first time, we observed a soft X-ray excess in the energy spectrum of pulsar 2S 1417-624. The origin behind this feature is explored in the light of present theoretical understanding about emission processes. We have also carried out the timing studies and found a remarkable evolution in the pulse profile of this pulsar with luminosity. The implications of these results are summarized in this chapter.

`Chapter 5:` The conclusive remarks on the present work and the prospects for future studies are discussed in this chapter.

Chapter 2

X-ray Instruments & Data Reduction: Analysis and Techniques

In the present thesis, we have used X-ray data collected from various instruments onboard three different X-ray observatories: the Rossi X-ray Timing Explorer (*RXTE*), the Neil Gehrels *Swift* observatory, and the Nuclear Spectroscopic Telescope Array (*NuSTAR*). This chapter offers a brief overview of the instruments, observations and X-ray data reduction, and analysis techniques. The chapter is arranged as follows: The first three sections are dedicated to describe individual instruments on board respective satellites. In the following section, we describe the detailed procedures adopted to reduce data from each instrument. The rest of the sections describe the analysis methods utilized to study the properties of accreting X-ray pulsars.

2.1 Rossi X-ray Timing Explorer (*RXTE*)

2.1.1 Satellite Overview

The Rossi X-ray Timing Explorer mission was launched on 30 December 1995 from NASA's Kennedy Space Centre. It remained operational for about 16 years and got decommissioned on 5 January 2012. Till date, the *RXTE* remained one of the most influential mission dedicated

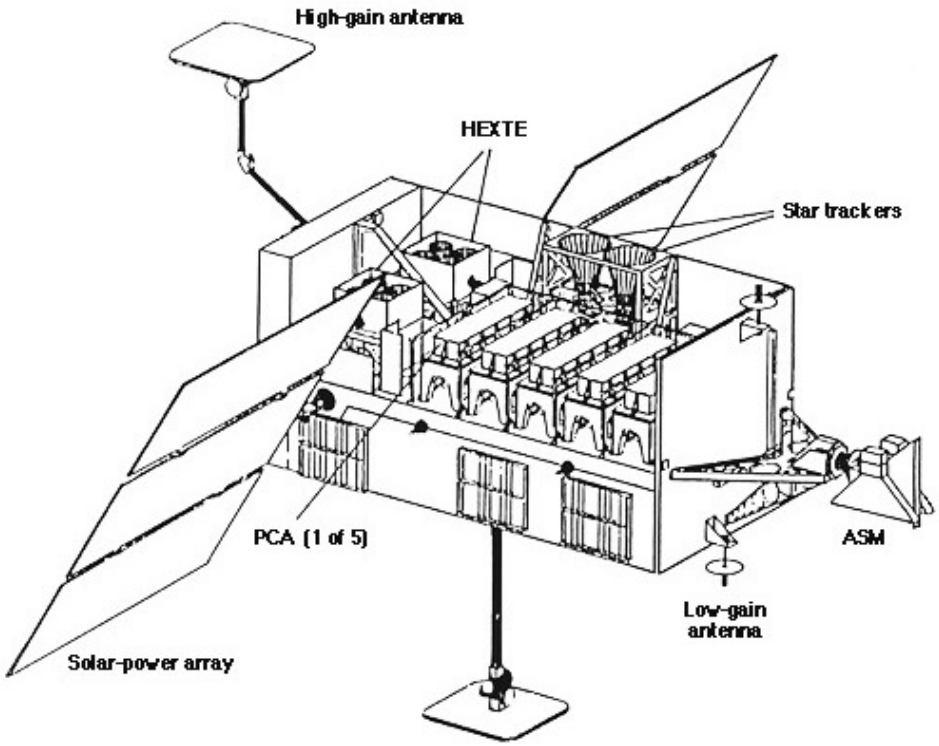

Figure 2.1: Schematic view of the *RXTE* spacecraft along with the major instruments onboard. Image Credits- `https://heasarc.gsfc.nasa.gov/docs/xte/xte_images.html#scraft`

for the study of temporal variability of astronomical sources in X-ray range. It provided an unprecedented time resolution thereby allowing to study the time variability of sources from micro-seconds to months and years. The Proportional Counter Array (PCA; Jahoda et al. 1996) and the High Energy X-ray Timing Experiment (HEXTE; Rothschild et al. 1998) were the two sets of primary instruments onboard *RXTE* with sufficient spectral overlap, providing the energy coverage from 3-250 keV. The *RXTE* also carried a small 1D coded mask All Sky Monitor (ASM; Levine et al. 1996), which continuously monitored the X-ray sky in a 2-12 keV energy range. The ASM was capable of scanning ∼80 % of the sky in every satellite orbit (∼96 minutes). It contributed to the detection of numerous transient X-ray sources during its lifetime. Figure 2.1 shows a schematic depiction of *RXTE* observatory, with the main instruments onboard it.

2.1.2 Proportional Counter Array (PCA)

The *RXTE*/Proportional Counter Array (PCA; Jahoda et al. 2006) was operational in 2-60 keV energy range and provided an energy resolution of <18% at 6 keV. It consisted of an array of five Proportional Counter Units (PCUs, labeled as PCU0-4) with a total effective area of ∼6500 cm^2. Each PCU consisted of five layers: a propane layer at the top acts as a veto later, the xenon filled veto layer sits at the bottom of the detector and three xenon layers situated in between, are surrounded by additional veto counters which help to reduce the background by discriminating the photons entering from the sideways. Each PCU runs in many different modes due to telemetry limitations. The observer could therefore select a suitable data mode to observe any particular source, in order to serve the scientific objective. These mode of observations would be discussed in detail in Section 2.4.1. A high timing resolution of ∼1 µs could be achieved from the event mode of PCA. The PCU0 was switched off after being hit by a micro meteorite on 12 May 2000[1]. This event caused the loss of propane and making it less useful. For this reason, data analysis is often restricted to PCU2, which is known as the best PCU among all (Jahoda et al., 2006). However, the other PCUs i.e. PCU1, PCU3 and PCU4, were switched on and off during the observations so as to compliment with PCU2 to cover the entire duration of an observation. Since PCA is a non-imaging instrument, the background determination becomes extremely important. The background is modeled using the data collected from the veto layers, since it can not be measured directly. It introduces a major source of uncertainty (1%) in the source spectrum. See Table 2.1 for the characteristic properties of these instruments.

2.1.3 High Energy X-ray Timing Experiment (HEXTE)

The High Energy X-ray Timing Experiment (HEXTE; Rothschild et al. 1998) consisted of two identical sets of instruments called Cluster-A and B. Each cluster was made of four NaI/CsI scintillator detectors with an effective area of ∼800 cm^2 at 50 keV (thus providing

[1] `http://heasarc.gsfc.nasa.gov/docs/xte/whatsnew/big.html`

Table 2.1: Detector specifications for primary instruments onboard *RXTE* observatory.

Parameters	Detector specifications	
	PCA	**HEXTE**
Detector type	5 Proportional Counter Units (PCU0-PCU4)	2 Clusters of 4 NaI/CsI Scintillation counters
Effective area	6500 cm^2	2×800 cm^2
Energy range	2-60 keV	15-250 keV
Energy resolution (FWHM)	<18%@ 6 keV	∼15%@ 60 keV
Time resolution	1 µs	8 µs
Detection sensitivity	0.1 mCrab	1 Crab
Field of View (FOV)	1° (FWHM)	1° (FWHM)

a total effective area of 2×800 cm^2). The HEXTE was operational in 15-250 keV range with an energy resolution of ∼15% at 60 keV. It provided a timing resolution of ∼8 µs. The background events are distinguished from the source events with the help of pulse shape discriminators. Since the pulse decay time in CsI crystal is different to that in NaI crystal, the pulse shape discriminators can identify in which crystal the event took place. An event registered simultaneously in both the crystals is identified as a background event caused by a charged particle traveling through the detector. In order to measure the background, both the HEXTE clusters were rocking ON/OFF the source position in every 16 s. During a pointed observation of the source of interest, both the clusters are 'rocked' orthogonal to each other, thereby allowing the simultaneous measurement of source and background events. Unfortunately the rocking mechanism of HEXTE clusters stopped working on 6 January 2006 for cluster A[2] and on 20 December 2010 for cluster B[3]. Since then, clusters A and B are fixed at on-source and off-source positions respectively. A complete data reduction and analysis guide for HEXTE is available at the RXTE Guest Observer Facility[4] and a brief overview of the instrument specifications for HEXTE (alongwith PCA) is listed in Table 2.1.

[2] `https://heasarc.gsfc.nasa.gov/docs/xte/whatsnew/newsarchive_2006.html#_hexteA-norock`
[3] `https://heasarc.gsfc.nasa.gov/docs/xte/whatsnew/newsarchive_2010.html#hexteB_locked`
[4] `https://heasarc.gsfc.nasa.gov/docs/xte/recipes/hexte.html`

2.2 Neil Gehrels *Swift* Observatory

2.2.1 Satellite Overview

The Neil Gehrels *Swift* observatory (hereafter *Swift*) is a multi-wavelength mission launched by NASA as a Medium Explorer program (MIDEX) on 20 November 2004. The mission acquired this name from its capability of pointing towards a source *swiftly* and autonomously in less than 90 s. The satellite is orbiting in a low earth orbit at an altitude of about 600 km and an inclination of 20.6°. The primary objective of this mission was rapid detection of gamma-ray bursts (GRBs) and multi-wavelength follow-up of their afterglow. For that purpose, the *Swift* has three scientific instruments onboard, in operation (Gehrels et al., 2004): the Burst Alert Telescope (BAT; Barthelmy et al. 2005), the X-Ray Telescope (XRT; Burrows et al. 2005) and the Ultra-Violet/Optical Telescope (UVOT; Roming et al. 2005). The *Swift*/BAT with largest field of view among all, is the primary instrument for GRB detection. While the XRT and the UVOT are high precision focusing instruments. Apart from the detection of GRBs, the *Swift* regularly scan for the transient sources in the X-ray sky and monitor them from time to time. The observed data becomes publicly available typically within a day after preliminary processing. Since UVOT is not sensitive to X-rays, it will not be discussed further. While the details of BAT and XRT instruments are given below in details. For a schematic view of the *Swift* observatory, please refer to Figure 2.2.

2.2.2 X-ray Telescope (XRT)

The X-ray Telescope (XRT) onboard *Swift* is a focusing X-ray telescope working in 0.3-10 keV range. It is specifically designed to measure the fluxes, spectra, and light curves of GRBs and afterglows over a wide dynamic range covering more than seven orders of magnitude in flux. The *Swift*/XRT has a total effective area of $\sim$110 cm^2 at 1.5 keV and it can pinpoint the location of any transient event with an accuracy of better than 5 arcsec (see Table 2.2). The XRT consist of 12 confocal and coaxial mirror shells (Moretti et al., 2005) arranged

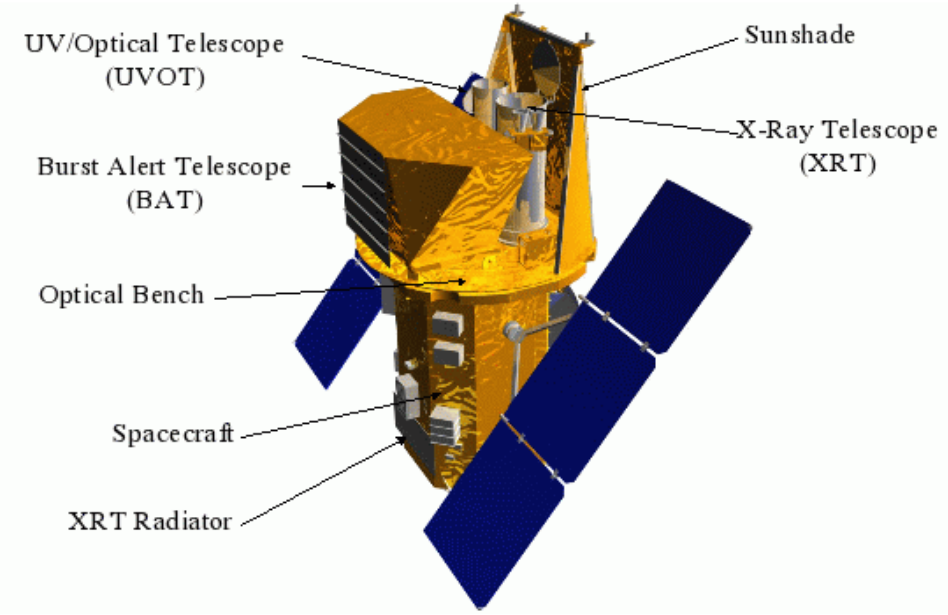

Figure 2.2: Schematic view of the *Swift* observatory with the main instruments labeled in the figure. The Image is taken from the webpage of NASA - `http://www.swift.ac.uk/about/instruments.php`

in the Wolter-I configuration, focusing on a single MOS CCD detector. The focal imaging array consist of 600×600 (40 μm × 40 μm) pixels with a plate scale of 2.36 arcsec/pixel. It provides a spectral resolution of 190 eV at 10 keV and 60 eV at 0.1 keV (FWHM), respectively. However, one should always be careful about the spectral features below 0.5 keV, where the effects of charge trapping starts to dominate.

Depending upon the brightness of the source being observed, the XRT can be operated in four different modes: (i) Imaging mode (IM), (ii) Photo-Diode (PD) mode, (iii) Photon Counting (PC) mode and (iv) Window Timing (WT) mode (see Hill et al. 2004 for more detailed discussion on readout modes of XRT). However, since the end of May 2005, PD mode is disabled. The IM mode produces an integrated image measuring the total energy deposited per pixel. It does not permit spectroscopy but the accurate position of the source is possible to determine in imaging mode. The PC mode is traditional frame transfer operation of a CCD camera. The full chip readout in this mode results in complete 2D image of the source, thereby limiting the time resolution to the readout time of 2.5 sec. While in the WT mode, high timing resolution of ∼1.8 ms could be achieved at the expense of loosing the information about the source position. In this mode, the readout is restricted to a narrow

Table 2.2: Detector specifications for *Swift*/XRT and *NuSTAR*/FPMs.

Parameters	Instrument Specifications	
	Swift/**XRT**	*NuSTAR*/**FPMs**
Telescope type	Wolter Type-I	Wolter Type-I
Focal length	3.5 m	10.14 m
Field of View (FOV)	$23.6' \times 23.6'$	$13' \times 13'$
Pointing accuracy	$3''$-$5''$	$\sim 1.5''$
Effective area	$\sim$125 cm^2@ 1.5 keV	$\sim$800 cm^2@ 6 keV
	$\sim$20 cm^2@ 8.1 keV	$\sim$125 cm^2@ 60 keV
Energy range	0.2-10 keV	3-78 keV
Energy resolution (FWHM)	140 eV @ 5.9 keV	400 eV @ 6 keV
		900 eV @ 68 keV
Time resolution	1.8 ms (for WT Mode)	2 µs
	2.5 s (for PC Mode)	
Detection sensitivity	2×10^{-14} (0.2-10 keV)	2×10^{-15} (6-10 keV)
(in erg cm^{-2} s^{-1})		1×10^{-14} (10-30 keV)

part of the CCD. The central 200 columns ($\sim$8 arcmin) are read out all at once in a single row, resulting in collapsed 1D source image. Due to high timing resolution of this mode, pile-up could be avoided for moderately bright sources ($<$ 100 counts/s; Romano et al. 2006). The primary characteristic properties of this telescope is listed in Table 2.2.

2.2.3 Burst Alert Telescope (BAT)

The Burst Alert Telescope (BAT) onboard *Swift* (Barthelmy et al., 2005) is an imaging telescope, designed primarily to monitor a large fraction of the sky for GRB occurrences. The mirrors are not used to focus the X-ray photons rather a D-shaped coded mask is used to reconstruct the source position with an accuracy of 5 arcmin. The X-ray photons are then detected by 32,769 CdZnTe (CZT) elements situated 1 meter behind the coded mask, i.e., at the detector plane. The mask has an area of 2.7 m^2, yielding a field of view of about $\sim$1.4 steradians. The BAT operates in two modes: burst mode which locate the burst position and survey mode which produces the hard X-ray survey data. In the present work, we have utilized the daily averaged monitoring light curves (in 15-50 keV energy range) provided by the BAT hard X-ray transient monitor[5] (Krimm et al., 2013).

[5]`https://swift.gsfc.nasa.gov/results/transients/`

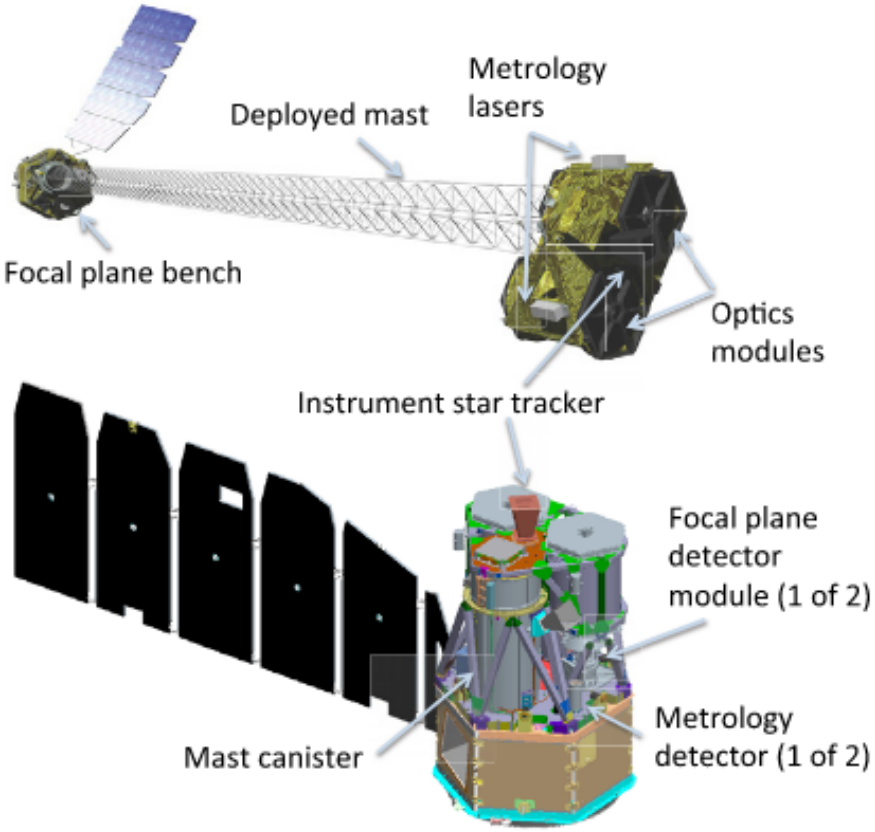

Figure 2.3: Schematic view of *NuSTAR* observatory in the stowed (bottom) and deployed (top) configurations. The figure is adapted from Harrison et al. (2013).

2.3 Nuclear Spectroscopic Telescope Array (*NuSTAR*)

The *NuSTAR*, the first hard X-ray focusing observatory (operating in a 3-79 keV range; Harrison et al. 2013), was launched on 13 June 2012 as a Small Explorer satellite mission (SMEX) led by the California Institute of Technology (Caltech) and managed by Jet Propulsion Laboratory (JPL). After being settled into a low equatorial earth orbit (with inclination $\sim 6°$) at an altitude of 600 km, the *NuSTAR* X-ray optics and detector benches got separated with the help of a deployable mast. In Figure 2.3, a schematic view of satellite is shown as before and after being deployed. The X-ray optics consists of two co-aligned grazing incidence Wolter-I telescopes with a focal length of 10.14 m each. Each telescope consists of 133 mirror shells arranged in a conical approximation of Wolter-I configuration. Each shell is coated with depth-graded multilayers of Pt/SiC and W/Si in alternation, thus enabling *NuSTAR* to achieve an efficient reflectivity up to 78.4 keV. Above this energy, the mirror coating starts absorbing instead of reflecting the hard X-ray photons (Harrison et al., 2013).

The two telescopes focus hard X-ray photons on separate focal plane modules FPMA and FPMB (hereafter FPMs). Each module consists of a 2×2 array of CdZnTe (CZT) crystal detectors with 32×32 pixels, resulting in a field of view of about ∼12 arcmin. Each pixel has an independent discriminator, hence the read out process is trigerred upon individual X-ray interactions. Therefore, the *NuSTAR* observations do not suffer from the effect of pile-up until a source flux of 10^5 count s^{-1} $pixel^{-1}$. The energy resolution of each detector is 0.4 keV at 10 keV and 0.9 keV at 68 keV (FWHM), respectively. Each FPM is shielded with an anti-coincident CsI scintillator. The X-ray events registered simultaneously in the CsI shield and CZT detectors are rejected as X-ray background by on-board electronics. The high temporal resolution of 2 μs could be achieved with the *NuSTAR*. Table 2.2 lists the instrument specifications for *NuSTAR* observatory.

2.4 Data extraction and analysis techniques

The raw event data files of each X-ray observation are stored in a Flexible Image Transport System (FITS) format and needed to be processed for deriving the science products from them. The High Energy Astrophysics Software (HEASoft)[6] package was utilized for the analysis of data obtained from above listed observatories. The HEASoft package is publicly available on NASA's High Energy Astrophysics Science Archive Research Centre (HEASARC)[7]. It is a multi-mission platform as the data from various observatories (known as supported mission) are publicly available on this platform. A Caliberation Data Base (CALDB)[8] is maintained on HEASARC for each individual mission, which regularly gets updated as per the instrument's performance and condition in space. We have utilized HEASoft version 6.17 and an up-to date CALDB to derive the scientific products for each observation. Below we list the procedures followed for the reduction of data obtained from the X-ray observatories mentioned in the previous sections.

[6] `https://heasarc.gsfc.nasa.gov/lheasoft`
[7] `https://heasarc.gsfc.nasa.gov/`
[8] `https://heasarc.gsfc.nasa.gov/docs/heasarc/caldb/caldb_supported_missions.html`

2.4.1 *RXTE* PCA and HEXTE data

The data obtained from the PCA onboard *RXTE*, runs through EDS (Experiment Data System) and gets packed into six different configurations called Event Analyzers (EAs), in order to serve the scientific objective of the observer/proposer. Two of these EAs always run in the following configurations :

- `Standard-1`: It is a binned mode configuration where the data are stored in a science array format (i.e., binned at regular intervals by onboard space electronics). The time resolution achieved via this mode is 0.125 s, but no energy information is possible due to the binning of all 256 energy channels into a single one.

- `Standard-2`: It is another binned mode configuration with a time resolution of 16 s (2 s for bright sources). This mode records the spectral information in 129 channels, covering 2-60 keV energy range.

Apart from these two EAs, the observer has a choice to select the other four EA modes. Common choices for other EA modes include `Good Xenon` mode (event mode with 256 channel resolution), `Generic binned` mode and `Generic FFT` mode. A complete guide to all the observing modes of PCA is available at the *RXTE Guest Observer Facility*[9]. To reduce the data obtained from these modes, it is necessary to make a Good Time Interval (GTI) file. This is done in order to get rid of unwanted data i.e., when the source of interest is at the edge of the field of view or occulted by the Earth. This is accomplished by using the GTI-generating `FTOOL` task `maketime`, alongwith the choice of apppropriate screening (or filtering) criteria. In the present work, we have implemented the following screening criteria to generate the GTI file: 'elevation angle `ELV`$>10^\circ$; electron contamination `ELECTRON2` <0.2 and pointing stability `OFFSET` $<0.02^\circ$'. Here, the keyword `ELV` denotes the angle between the Earth's limb and the source of interest, subtended by the spacecraft. The shape of the source spectrum is distorted when the `ELV` is low, for instance, when the source is occulted by the earth, `ELV`$< 0^\circ$. Furthermore, the PCA is subjected to contamination from the trapped electron in the Earth's magnetosphere, which contribute towards higher background level at lower

energies. Such events are filtered by setting `ELECTRON2` <0.2. Additionally, the on-source data file occasionally contains short streches of slew data which needs to be filtered out while creating a clean event file. This is done by setting the keyword `OFFSET` <0.02°. The `saextrct` task was finally utilized to create the light curve and spectrum of the source from the binned mode data (`seextrct` for the event mode data). While background estimation was done by using `runpcabackest` task of `FTOOLS`. The response files were generated by using `pcarsp` task.

In the present work, we have utilized the Cluster-B data of HEXTE for spectral analysis (see Chapter-4). The `hxtback` task was used to estimate the background and the deadtime correction was done by the task `hxtdead`. Finally, response matrix files were generated by using `hxtrsp` task. The individual recipes for the data reduction of the PCA and HEXTE data are available in the *RXTE Cook book*[10].

2.4.2 *Swift* XRT data

The *Swift*/XRT (Burrows et al., 2005) data used in the present thesis work, were reduced and analyzed by following the standard procedures suggested by the instrument team[11]. The standard `xrtpipeline` task was utilized to reprocess the raw event files into the screened event files. We used latest calibration (`CALDB`) files of *Swift* mission while reducing the XRT data. Depending upon the source brightness, the events are automatically recorded in different modes (e.g. for a source brightness of 10 mCrab−600 mCrab, the event is observed in WT mode while for <10 mCrab, the PC mode gets activated). However, the data extraction procedure for all the modes is similar.

The present thesis work is dedicated towards the study of Be X-ray Binary (Be/XRB) pulsars during the outburst phases, where the X-ray luminosities of such sources are significantly higher. Therefore, these pulsars are usually observed in WT mode of XRT, in order to avoid the pile-up[12] effects. In our analysis, we have estimated the effect of pile-up events, by following the recipes suggested by the instrument team. For the WT mode, the source

[9] `https://heasarc.gsfc.nasa.gov/docs/xte/abc/pca_issues.html#struc`
[10] `https://heasarc.gsfc.nasa.gov/docs/xte/recipes/cook_book.html`

products were extracted from the cleaned event file by applying a rectangular region file of 20×40 pixels (centered on the source position) in the `xselect` package. The extraction region was chosen carefully by following the recommendations of the instrument team[13]. While the background products were extracted by choosing another region in the outer parts of the CCD. The auxiliary response file (ARF) was generated by using `xrtmkarf` task while the response file was sourced from the latest CALDB.

2.4.3 *NuSTAR* data

In order to reduce the *NuSTAR* data, we have used standard *NuSTAR* data analysis software (`NuSTARDAS`) available in the HEASoft package. The `nupipeline` task was run to extract the calibrated and cleaned event files from the raw data files. These events are further reprocessed to generate the science quality products i.e., barycenter corrected light curves, energy spectrum, effective area files and response matrices for each detector (FPMA and FPMB) by using `nuproducts` task. The source light curves and spectra are accumulated by selecting a circular region centered around the source coordinates in the cleaned event file. The background products are extracted in the similar manner by selecting another circular region away from the source center (in order to avoid the contamination from source photons). A detailed description of individual task could be found in the *NuSTAR* data analysis software guide[14].

2.5 Timing analysis methods

X-ray photons from the astrophysical sources, after being detected in the X-ray detectors are stored as event lists. The event list contains information regarding the arrival time and

[11] `https://www.swift.ac.uk/analysis/xrt/`

[12] The pile-up of source photons occurs when two or more soft X-ray photons are registered as a single higher energy photon. However, it is possible to estimate the extent of pile-up effected area in the source image on the detector plane. For any scientific analysis, this pile-up effected area has to be estimated and removed from the event file. In case of XRT, the step by step procedure for pile-up correction could be found at: `https://www.swift.ac.uk/analysis/xrt/pileup.php`

[13] `https://www.swift.ac.uk/analysis/xrt/spectra.php`

[14] `https://heasarc.gsfc.nasa.gov/docs/nustar/analysis/nustar_swguide.pdf`

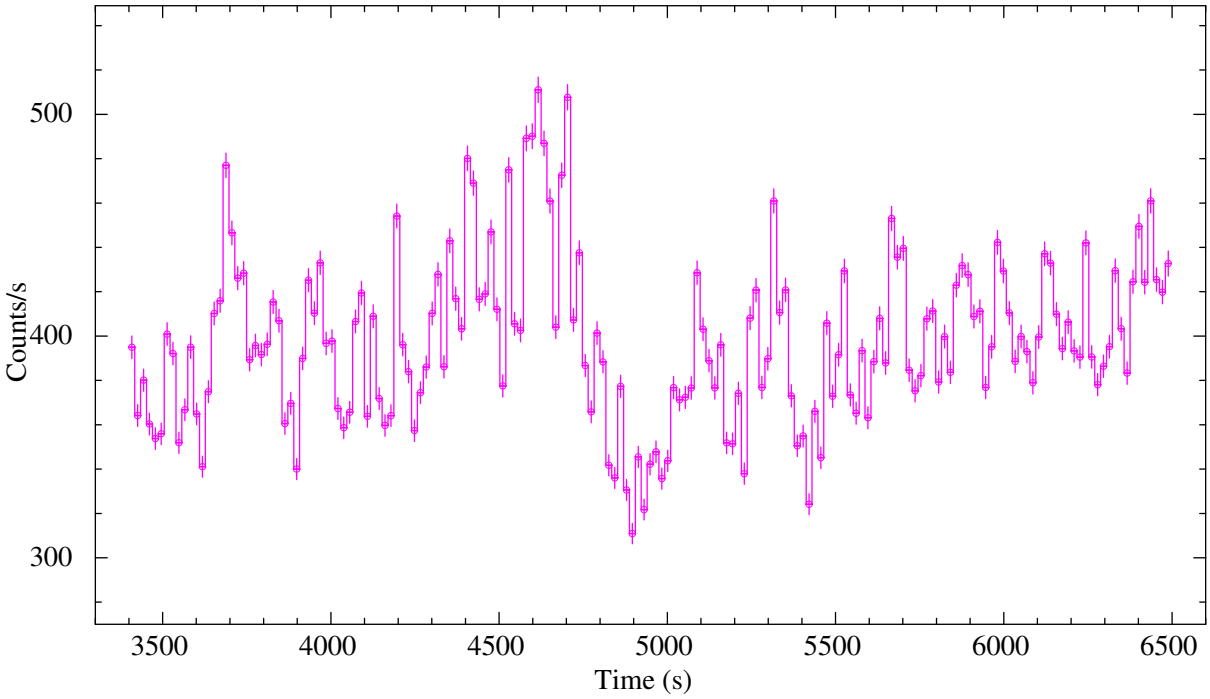

Figure 2.4: A representative light curve of a Be/XRB pulsar 2S 1417-624 obtained from one of the *RXTE* observation during an X-ray outburst is shown. The light curve is plotted by using `lcurve` task of FTOOLS. The light curve was extracted for a time resolution of 0.125 s (from `Standard-1` PCA data) and is rebinned at the pulsar spin period (∼17.5 s). This was done in order to see the time variations in the light curve, apart from the variations due to the spin period.

position of the photon on the detector plane along with its energy. In order to study the timing properties of a given source, its light curve (i.e., the distribution of photon counts over time) was extracted by using `XRONOS`[15] package. The `XRONOS` is a timing analysis software package available as a subpackage of `FTOOLS`[16].

By following the procedures described in the previous section, we extracted the source light curve by selecting an appropriate circular region centered on the object of interest (in case of X-ray imaging instrument, e.g. *NuSTAR*/FPMs and *Swift*/XRT). While the background light curves were extracted in similar manner from the source free region. Finally, the background subtraction of the source light curves was done by using the task `lcmath`. The background subtracted source counts were then rebinned and plotted using `lcurve` task. While rebinning, the minimum time bin of the light curve should be chosen in such a way that the presence of any periodic or aperiodic variations in the source intensity should get retained and made clearly visible. A representative light curve of a Be/XRB pulsar observed with the *RXTE* observatory during an X-ray outburst is presented in Figure 2.4.

In order to search the periodicity associated with the pulsar spin, a periodogram analysis is being carried out. Most commonly used technique to construct or create a periodogram is the Fourier Transform (FT) of the light curve. In order to perform a detailed and consistent timing analysis of pulsars, we have used three independent methods in the present thesis work. These methods are summarized below. Finally, I will conclude this section with the description of epoch folding method and `efold` task to generate the pulse profiles of X-ray pulsars.

2.5.1 Fourier Transform (FT)

Any given function or periodic signal can be converted into frequency domain by using Fourier transformation technique. This basically provides the amplitude of sinusoidal (or any periodic) signal present in the time series, as a function of its frequency. For a finite number of discrete measurements (with n = 0, 1, 2,..., N-1) of quantity 'A', the k^{th} element of a uniformly-spaced time series $A(t_n)$ can be written as:

$$B(\nu_k) = \sum_{n=0}^{N-1} A(t_n)\ \exp(-i\nu_k t_n), \qquad k = 0, 1, 2, .., N-1 \tag{2.1}$$

where the power accumulated at frequency ν_k is given by

$$P(\nu_k) = \frac{|B(\nu_k)|^2}{N} \tag{2.2}$$

In the present work, we have utilized `powspec` task of `FTOOLS` to create the Power Density Spectrum (PDS) from the source light curves. In Equation 2.2, $P(\nu_k)$ represents the strength of individual frequency component present in the time series. Therefore, a strong and narrow peak in the PDS corresponds to the most significant periodic variation in the light curve, which in our case is usually the spin period of the pulsar. Apart from periodic signals, the PDS of some X-ray binaries show aperiodic or quasi-periodic power peaks known as Quasi

[15] `https://heasarc.gsfc.nasa.gov/docs/xanadu/xronos/xronos.html`
[16] `https://heasarc.gsfc.nasa.gov/lheasoft/ftools/ftools_subpacks.html`

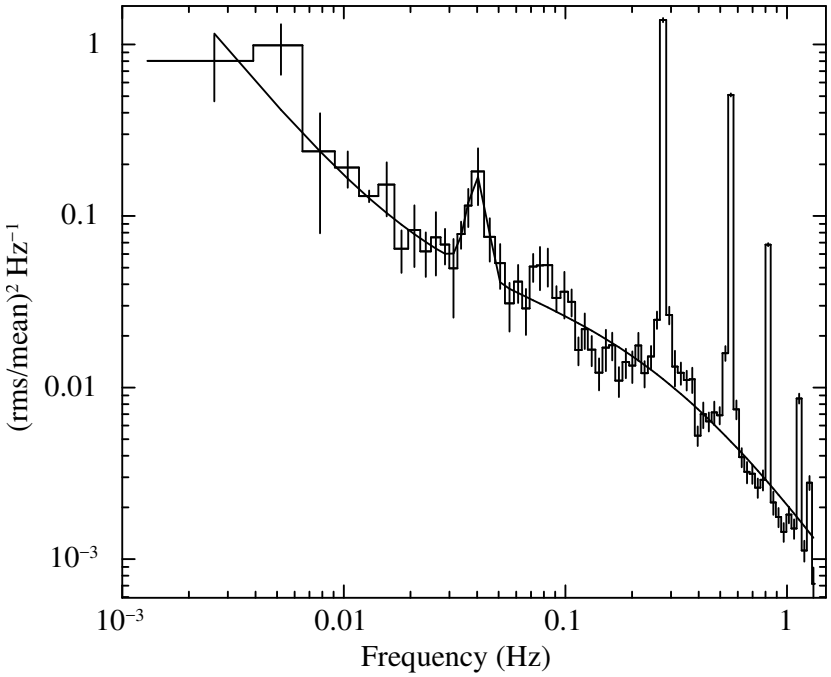

Figure 2.5: The power density spectrum obtained from one of the *RXTE* observations of the transient Be/XRB pulsar 4U 0115+634 during its 1999 X-ray outburst, showing a broad QPO feature at 41 mHz alongwith sharp peaks corresponding to the spin frequency of the pulsar v_{spin} and its harmonics. The figure is taken from Dugair et al. (2013).

Periodic Oscillations (QPOs). As opposed to periodic signals, QPO usually appears as a broader feature in the PDS of X-ray binaries. Figure 2.5 shows a representative PDS for a transient high mass Be/XRB pulsar 4U 0115+634 (Dugair et al., 2013). The data were taken from one of the *RXTE* observations of the pulsar during an X-ray outburst in 1999 March. A broad feature can be seen in the PDS at around 41 mHz (v_{QPO}) has been identified as the QPO feature present in the source, while the other sharp peaks represent the spin frequency of the pulsar (v_{spin}) along with its harmonics. The QPOs have been widely interpreted as the beat frequency between the rotating neutron star and the inner edge of the accretion disk (known as magnetospheric beat frequency model; Alpar & Shaham 1985). According to another explanation, the QPO gets originate from the modulation of X-rays by the inhomogeneities present in the accretion disc at the disk keplarian frequency (known as keplarian frequency model; van der Klis et al. 1987).

Apart from the `powspec`, two independent methods i.e., Lomb-Scargle periodogram and `CLEAN` algorithm (as implemented in `STARLINK` software collection[17]; Currie et al. 2014) were also used for the timing analysis in the present work. The Lomb-Scargle (LS) periodogram is

a modified version of Fourier transform and is mainly useful for the detection of weak periodic signal in unevenly sampled time series. This method provides a unique 'False Alarm Probability', (FAP; Scargle 1982; Horne & Baliunas 1986) which is the probability of determining a peak in the periodogram, provided that the data is assumed to be pure noisy. While, the corresponding error on the true frequency of the periodic signal could be estimated by (Horne & Baliunas, 1986),

$$\delta\nu = \frac{3\pi\sigma_N}{2N^{1/2}TA} \tag{2.3}$$

where N is the number of data points in the time series, A is the amplitude of the signal, σ_N is the standard deviation of the noise after the signal has been removed and T is the duration of observation. Generally, this method requires an order of $10^2\mathrm{N}^2$ operations to analyze N number of data points, due to which it is often termed as slow method. An improved implementation of this method by Press & Rybicki (1989), however, requires $10^2\mathrm{N(logN)}$ operations, making the calculations much faster. Therefore, this method could be utilized even for larger time series data.

In general, the pointed X-ray observations are interrupted with irregular gaps attributed to various effects like the passage of satellite through the South Atlantic Anomaly (SAA) regions and the source being obstructed by earth in some cases. These gaps are responsible for the effect of spectral leakage in the PDS and hence complicating the process of finding the true periodicity. The `CLEAN` algorithm is specially developed to deal with such infrequent samplings (Roberts et al., 1987). This alogorithm basically de-convolves the spectral window from the dirty power spectrum. Therefore, it generates a `CLEAN`ed power spectrum i.e., which is free from the effect of spectral leakages in the final output. In this method, the error on the estimated period value is determined as $P^2/2T$, where P is the estimated period value and T is the duration of observation (see Roberts et al. 1987).

[17] `http://starlink.eao.hawaii.edu/starlink`

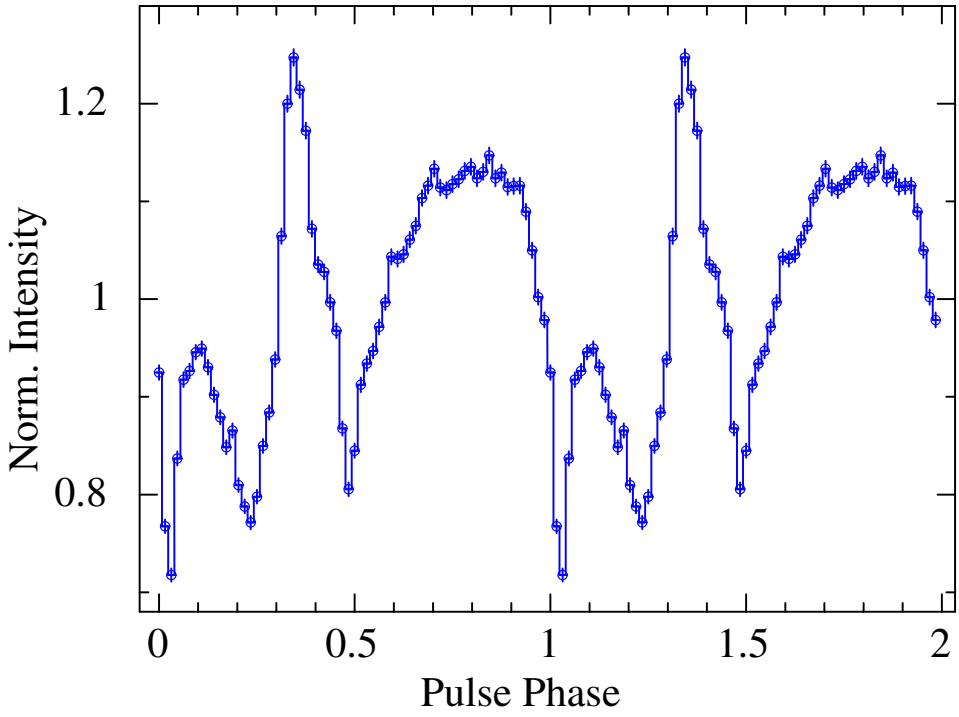

Figure 2.6: The output of `efold` task performed on the pulsar light curve shown in Figure 2.4. The pulse profile is created by folding the pulsar light curve with 0.125 s time resolution with its best determined period, by `efsearch` task. Two pulses are shown for the clarity.

2.5.2 Epoch folding method

Epoch folding is another method to search for periodicity in the light curves and it is available as `efsearch` task in `FTOOLS`. This task considers a range of trial periods for a given trial period as input on which the light curve is folded. It finally plots a distribution between χ^2 value of folded light curve and the offset between the true periodicity and the trial period. The period corresponding to the highest value of χ^2 represents the true periodicity of the pulsar (see Leahy et al. 1983 for details and implementation of this task). After having determined the spin period of the pulsar, the pulse profiles of accretion powered X-ray pulsar are generated by folding the light curves at this period by using the `efold` task of FTOOLS. It outputs a plot with *Normalized Counts* s^{-1} versus phase folded *period* (ranging from 0.0-1.0). A sample pulse profile of the transient Be/XRB pulsar 2S 1417-624 is shown in the Figure 2.6. It is created by folding a light curve of the pulsar with a time resolution of 0.125 s, at the pulse period determined from the `efsearch` task as described above.

2.6 Spectral analysis methods

The observed spectrum $D(I)$ of an X-ray source is basically a distribution of photon counts over the instrument channels (I). However, it is not the actual description of the source properties as the spectrum measured with the X-ray detectors are contaminated with the background contribution $B(I)$. Therefore, the observed spectrum of the source $D(I)$ is related to the actual spectrum $f(E)$ by:

$$D(I) = \int_0^\infty R(I,E) f(E) A(E) dE + B(I), \tag{2.4}$$

where $R(I,E)$ is the response matrix function which is the probability that an incoming photon of energy E would be detected in channel I, and $A(E)$ is the effective area of the instrument. The net source counts per channel (after background subtraction) could be thus derived by the quantity $D(I) - B(I)$. Since there are N number of discrete channels, the integral part of Equation 2.4 can be written as summation, i.e.,

$$D(I) - B(I) = C(I) = \sum_{i=1}^{N} f_i(E) R_i(I,E) \tag{2.5}$$

In principle, the response matrix function is a non-invertible matrix. Hence Equation 2.5 could not be solved directly to infer the actual source spectrum $f(E)$. Rather, an alternative approach is used to find the actual source spectrum in which an empirical or physically motivated spectral models $M(I)$ are used to "fit" the observed spectrum $C(I)$. Then the model predicted counts are being compared with the observed counts by using a fit statistics. The most commonly used fit statistic is chi-square statistics which is defined as:

$$\chi^2 = \sum_{i=1}^{N} \frac{(C_i(I) - M_i(I))^2}{\sigma_i(I)^2}, \tag{2.6}$$

where σ_i(I)=$\sqrt{C_i(I)}$ is the error associated with the observed counts $C(I)$ assuming Gaussian distribution (Wheaton et al., 1995). In general, for best-fit, the expected value of "Reduced-χ^2

$= \chi^2/(\text{dof})$" to be approximately equal to one for any acceptable model. Here, the number of degrees of freedom (dof) is taken as the difference between the number of energy channels/bins and number of free parameters of the best-fitted model. For the case of low count statistics (or low source counts, it is more appropriate to use C-statistic (CSTAT) for the spectral fitting. However, there may be cases when a number of models could be acceptable to fit the data with comparable goodness-of-fit. In such cases, the choice of best-fit model is driven by the scientific judgment and feasibility of the derived parameters. After having obtained the best-fit parameter values for the given model of choice, one must determine the range of values within which true value of parameter lies, called confidence interval. In the present work, we have estimated the best-fit parameter values for 90% confidence level unless stated otherwise.

We used `XSPEC` package for the spectral fitting in this thesis work. The X-ray spectral fitting package (`XSPEC`; Arnaud 1996) is a command-driven, interactive, X-ray spectral-fitting program, available as an integrated part of `HEASoft`. The `XSPEC` package comes equipped with inbuilt models ranging from simple mathematical functions (e.g. constants, power laws, Gaussians, etc.) to highly complex physically-motivated models. A brief overview of the physical models used in the present work are given at the end of this chapter, while a more detailed description is presented in Chapter-4. For the present work, I have extensively utilized the commonly used empirical models for the continuum modeling of Be/XRB pulsars. Apart from the continuum spectra, other spectral components such as interstellar absorption, atomic emission lines, blackbody emission, are also seen in the spectrum of X-ray pulsars. In the following subsection, I will present an overview of these components.

2.6.1 Empirical Continuum Models

Despite of the complexity of the various physical processes involved in the spectral formation in accreting X-ray pulsars, the spectrum could be well described with simple power-law based models. Moreover, as described in Chapter-1, bulk comptonization plays a significant role in

upscattering of the seed X-ray photons, which mainly results in the power law continuum of the form:

$$\texttt{powerlaw}(E) = NE^{-\Gamma}, \tag{2.7}$$

where N is the normalization of the power law, representing the photon flux in Photons keV^{-1} cm^{-2} s^{-1} units and Γ is the photon index of the power law, varying in the range of 0.0-2.0. However, the observed spectrum of accreting X-ray pulsars generally shows an exponential cut-off (E_{cut}) around 5-30 keV energies (see Bildsten et al. (1997) and references therein). Therefore, a `Cutoffpl` i.e, power law modified with an exponential cut-off is commonly used in spectral fitting. The mathematical form of `Cutoffpl` is:

$$\texttt{Cutoffpl}(E) = NE^{-\Gamma}e^{-E/E_{cut}}, \tag{2.8}$$

Another widely used model to describe the spectral continuum of pulsars is the `HighECut` model, which includes an additional fit parameter (E_{fold} as compared to `Cutoffpl` and is expressed analytically as:

$$\texttt{HighECut}(E) = NE^{-\Gamma} \times \begin{cases} 1 & (E \leq E_{cut}), \\ e^{-(E-E_{cut})/E_{fold}} & (E > E_{cut}) \end{cases} \tag{2.9}$$

This model is successfully able to reproduce the spectrum of most of the accretion powered X-ray pulsars and is widely used among all the empirical models (White et al., 1983). However, as we can see from the analytical expression, the functional form is not continuously differentiable at roll-over energy E_{cut} (not to be confused with the E_{cut} of `Cutoffpl` model). Therefore, it sometimes produce spurious absorption-like features around E_{cut}. Another model which fix this issue is `NewHCut` model (Burderi et al., 2000), i.e., a power law

modified with high energy cutoff with smoothening around cut-off energies, expressed as:

$$\texttt{NewHCut}(E) = \begin{cases} NE^{-\alpha} & (E \leq E_{cut} - \Delta(E)), \\ c_3E^3 + c_2E^2 + c_1E + c_0 & (E_{cut} - \Delta(E) < E < E_{cut} + \Delta(E)), \\ NE^{-\alpha}e^{-(E-E_{cut})/E_{fold}} & (E \geq E_{cut} + \Delta(E)) \end{cases} \tag{2.10}$$

where, the constants c_0, c_1, c_2, and c_3 are computed by assuming the continuous derivability of the functional form of `NewHCut`(E) in range $E_{cut} - \Delta E$ to $E_{cut} + \Delta E$ and ΔE is usually fixed at 5 while fitting. Another empirical model is negative and positive exponential cut-off model, called `NPEX` and expressed as:

$$\texttt{NPEX}(E) = A(E^{-\alpha} + BE^{+\beta}) \times exp(E/KT), \tag{2.11}$$

where, A and B are the normalizations and α and β are photon indices of the negative and positive power laws, respectively. The `NPEX` model was introduced by Mihara (1995). It differs from the above mentioned continuum models in the sense that it consists of two power laws. The parameter kT here plays a similar role as cutoff energy in other models. The index β represents Wein's hump in the spectrum and is generally fixed at 2 (Makishima et al., 1999), while α corresponds to the hard comptonized part and is left free to vary while fitting in `XSPEC`.

2.6.2 Photoelectric absorption and other spectral features

The intrinsic source spectrum gets modified by the interstellar absorption before reaching the X-ray detectors. The interaction of X-ray photons with the absorbing matter could be responsible for two observable features in the pulsar spectrum, namely the absorption of soft X-ray photons in the continuum spectrum and absorption edges or fluorescent emission lines. The continuum absorption is manifested as a lack of soft X-ray photons mainly at energies below ∼10 keV. The spectral model `Phabs` (i.e., photoelectric absorption model), implemented

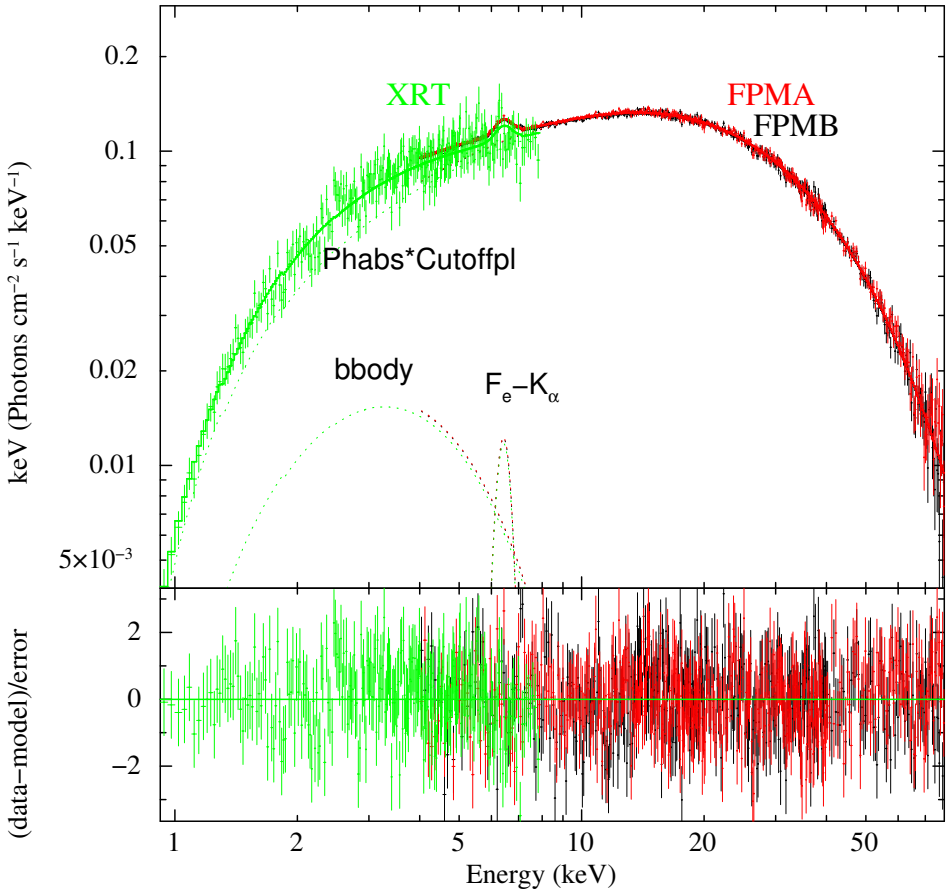

Figure 2.7: A sample spectrum fitted with empirical model: Phabs*(Cutoffpl+bb+ga) is shown. The contribution of different spectral components is labelled and is shown in different colors.

in `XSPEC` and widely used to describe the continuum absorption, is expressed as:

$$M(E) = exp[-N_H \sigma(E)], \tag{2.12}$$

where, N_H is the density of the absorbing material measured in atoms cm^{-2} and is normalized to the total hydrogen number density, known as equivalent hydrogen column density. While σ(E) represents the cross-section for the absorption of X-ray photon with energy E. It is mainly derived by considering the individual contribution of three different cross sections of gas, grain and molecules present in the interstellar medium (ISM) (see Wilms et al. (2000) for a detailed discussion). This is modeled in the fitted spectrum by the `Phabs` model component. The `Phabs` model calculates the absorption cross section by taking into account of the gas-phase ISM only. However, an updated version of this model, i.e. `tbabs` (Tuebingen-Boulder ISM absorption model) is also implented in `XSPEC` (Wilms et al., 2000), which takes into

account all the three phases of ISM. In `tbabs`, while calculating the gas-phase ISM, the effective cross section is the sum of the photoionization cross sections of the different elements (weighted by their respective abundance). For molecular-phase, only molecular hydrogen is considered and for the grain-phase ISM, the effect of shielding by the grains is taken into account while calculating the cross section value.

On the top of continuum absorption, another prominent feature in the energy spectrum of accreting X-ray pulsars is the presence of Fe-K_α fluorescent emission line at 6.4 keV (see Figure 2.7). Due to the presence of strong stellar winds of the companion star, some accreting pulsars show additional Fe line at 6.7 keV, originating from the H-like Fe atoms (Nagase (1989) and references therein). These lines are modeled in `XSPEC` as a Gaussian function (`gauss`), expressed as:

$$\texttt{gauss}(E) = \frac{A}{\sigma\sqrt{2\pi}} \exp\left(\frac{-(E-E_0)^2}{2\sigma^2}\right) \tag{2.13}$$

where A is the normalization of the Gaussian component in units of photons cm^{-2} s^{-1} and E_0 and σ are line energy (Gaussian centroid) and line width in keV, respectively.

Several accreting pulsars have also been observed to show an excess at soft X-ray ranges, in addition to the continuum emission (below ∼5 keV). This is known as 'soft X-ray excess' and it is thought to be a very common intrinsic feature of X-ray pulsars. However, its detectability depends upon the source flux and column density (N_H) in the source direction (see Hickox et al. (2004) for a review). It has been modeled with a thermal blackbody spectrum of the form:

$$\texttt{bbody}(E) = N \times 8.0525 \frac{E^2}{(kT)^4(exp(E/kT)-1)} dE, \tag{2.14}$$

where, N is blackbody normalization in the units of 10^{39} erg s^{-1} (10 kpc)$^{-2}$ and kT is the blackbody temperature. In order to describe the pulsar spectrum shown in Figure 2.7, a `bbody` component was also used. The last empirical model presented here is a Lorentzian absorption profile to model a Cyclotron Resonance Scattering Feature (CRSF) in the pulsar spectrum (see Chapter-1 for the formation and discussion on the CRSF features; Makishima

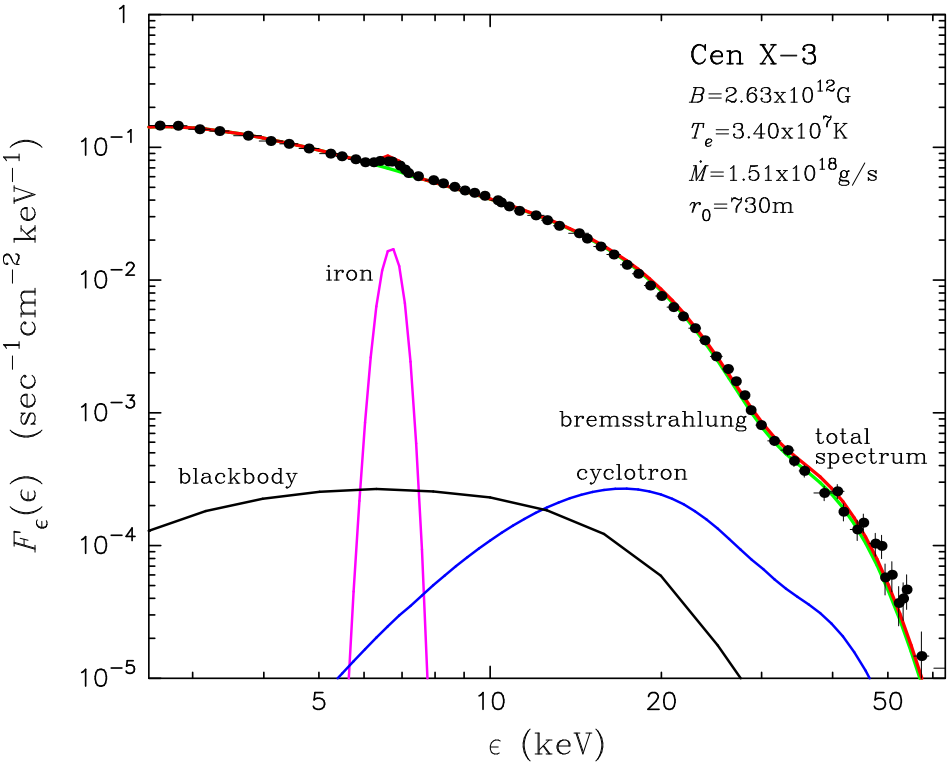

Figure 2.8: Theoretical energy spectrum (red line) of the pulsar Cen X-3, compared with the observational data taken from *BeppoSAX* observatory (black circles). The contribution of different spectral components is shown in different colors. The total spectrum is modulated with the interstellar absorption with hydrogen column density N_H= 2.0×10^{22} cm^{-2}. The figure is adapted from Becker & Wolff (2007a).

et al. 1990) and is expressed as:

$$\texttt{cyclabs}(E) = exp\left(-\tau \frac{WE/E_{line}^2}{(E-E_{line})^2 + W^2}\right) \tag{2.15}$$

where, E_{line} is the centroid energy and W and τ are the width and optical depth of the CRSF, respectively. However, the shape of the cyclotron line is better described by a Gaussian absorption profile (`Gabs`) for some sources. The functional form for `Gabs` model is expressed as:

$$\texttt{Gabs}(E) = exp\left(\frac{-\tau}{\sqrt{2\pi\sigma}} exp\left(\frac{-(E-E_{line})^2}{2\sigma^2}\right)\right) \tag{2.16}$$

where E_{line}, σ and τ are cyclotron line centroid energy, width and depth respectively.

Apart from the empirical models described above, we have implemented two physical models *COMPMAG* and *BWmod* in the present work. These models solve the RTE (see equation 1.15, Chapter-1) numerically and analytically, respectively. The key approximation

which allows these models to make RTE separable in energy and space, is the use of a specific velocity profile that is linearly dependent on optical depth of the accretion column (Becker & Wolff, 2007b). While solving RTE, the *BWmod* takes into account three major sources of injecting *seed photons* i.e., blackbody, cyclotron and bremsstrahlung processes (see Chapter-1, Section 1.5). The current version of publicly available *COMPMAG* model incorporates only the contribution of black-body *seed photons*, however, the velocity profile calculated by this model is the actual implementation of the true profiles calculated by Basko & Sunyaev (1976). A more detailed discussion and the method of implementation of these models are presented in Chapter 4 and a typical spectrum of a pulsar simulalted with *BWmod* is shown in Figure 2.8. In this case, the continuum emission is dominated with the contribution from bremsstrahlung emission. Also, it is worth mentioning that the comparison between theoretical spectrum and observed data, (as shown in Figure 2.8) and therefore the agreement between them, is rather qualitative.

Chapter 3

RXTE Observations of 2S 1417-624 during 2009 giant outburst

In this Chapter, a detailed spectral and timing studies of Be/X-ray binary pulsar 2S 1417-624 during its 2009 giant outburst are presented. Several pointed observations of the pulsar were carried out with the instruments onboard the Rossi X-ray Timing Explorer *(RXTE)* observatory, covering the rising as well as declining phase of the giant outburst. Timing properties of the pulsar such as spin period, evolution of the spin period, pulse profiles, energy and luminosity dependence of the pulse profiles and spectral properties such as continuum model, emission lines, features present in the source spectrum etc. have been investigated and presented in this Chapter. The Chapter is structured in the following way : A detailed introduction to the source is given in Section 3.1, followed by the details of observations utilized in the present work (Section 3.2). In Section 3.3, timing analysis is presented which is followed by spectral analysis in Section 3.4. Finally, the results are discussed in the context of present theoretical models for the accretion onto magnetized neutron star in Section 5.

3.1 Be/X-ray binary pulsar 2S 1417-624

The transient Be/X-ray binary pulsar 2S 1417-624 was first discovered in 1978 with the third *Small Astronomy Satellite (SAS-3)* observatory (Apparao et al., 1980). It was subsequently detected with other space-based missions as a variable Galactic X-ray source and recognized as 4U 1416-62 and MX 1418-61 (Forman et al. 1978; Markert et al. 1979). Kelley et al. (1981) analyzed the *SAS-3* archival data and detected a coherent pulsation of ∼17.64 s from the source light curves, thus confirming the source to be a pulsar. The source positions were refined later in 1979 through observations made with the high-resolution imaging detector (HRI) onboard the *Einstein* X-ray observatory. This allowed the optical identification of the companion as a B1 Ve star, located at a distance of 1.4–11.1 kpc (Grindlay et al., 1984), thereby confirming it to be a Be/X-ray binary system.

As opposed to systems like EXO 2030+375 (Epili et al., 2017), A0535+262 (Naik et al., 2008) and GRO J1008-57 (Kühnel et al., 2017) which show regular outbursting phenomenon at almost every periastron passage, 2S 1417-624 remains dormant for most of its observational history since its discovery. Only four Type II outbursts (sometimes followed by Type I outburst) have been detected from 2S 1417-624 till 2018 (Kelley et al. 1981; Finger et al. 1996; İnam et al. 2004; Gupta et al. 2018). However a fifth giant outburst has been observed from the source recently in 2018 (Nakajima et al. 2018; Krimm et al. 2018), which is the main topic of investigation in the Chapter-4.

Following its discovery in 1978, 2S 1417-624 remained in quiescence for about 16 years until a second giant outburst occurred in 1994 August. The giant outburst lasted for about 110 days and subsequently followed by five smaller Type I outbursts until 1995 July (Finger et al., 1996). BATSE onboard the *Compton Gamma Ray Observatory (CGRO)* continuously monitored the source during this period and the binary orbital parameters of the system such as orbital period P_{orb}=42.12 d, eccentricity e=0.446, semi-major axis $a_x\ sin\ i$=188 lt-s, ω=300°.3 and time of periastron passage T= JD 2449714.12 were derived by Finger et al. (1996). The mass function of the system was also derived from the BATSE data which put a

lower limit of 5.9 $M_{\odot}$ on the mass of the optical companion. These authors reported a spin-up rate of (3-6) $\times$ 10^{-11} Hz s^{-1} and established a strong correlation between spin-up rate and pulsed flux of the pulsar.

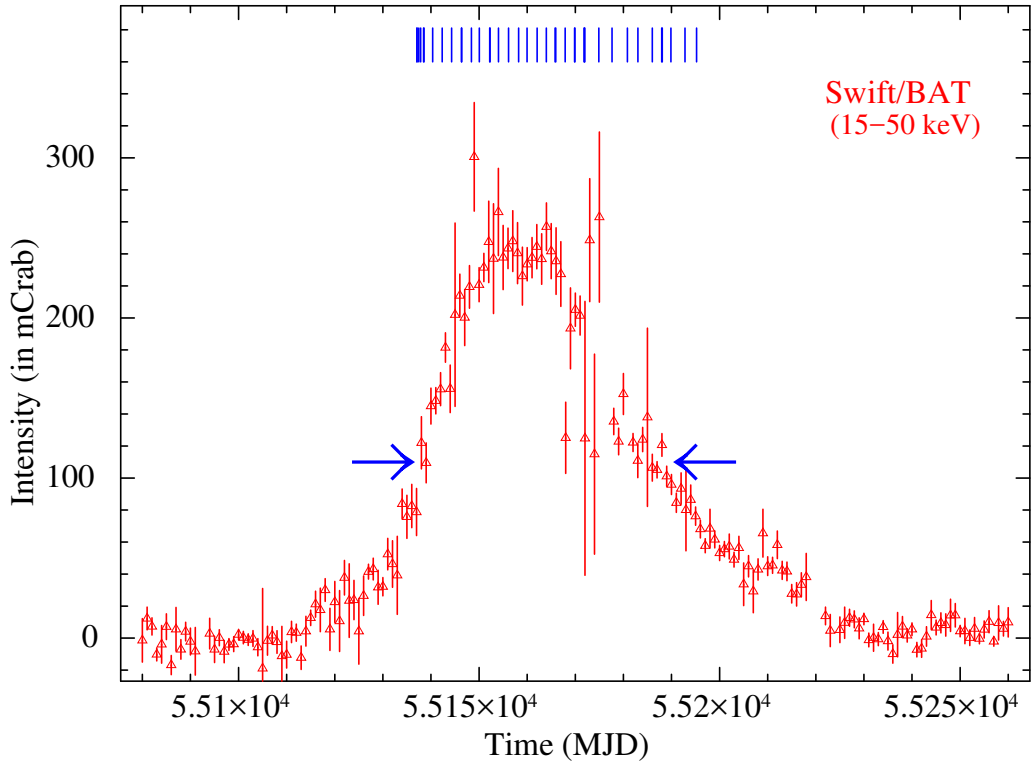

Figure 3.1: The *Swift*/BAT monitoring light curve of 2S 1417-624 in 15-50 keV range during its 2009 giant outburst. Two horizontal blue arrows mark the beginning and end of the *RXTE* pointed observations. A total of 39 *RXTE* pointed observations were carried out during this period, which are indicated by the blue vertical lines at the top of the figure. This figure is generated by using the data from the website of *Swift*/BAT hard X-ray transient monitor- `https://swift.gsfc.nasa.gov/results/transients/weak/H1417-624/`

The binary orbital parameters of the system were later refined by Raichur & Paul (2010) using data obtained from the *RXTE* observations of the pulsar during the third giant outburst in 1999. This outburst lasted from 1999 November to 2000 August. Using these observations, İnam et al. (2004) reported the intensity dependent pulse profiles and pulsed fraction of the pulsar. The pulsed fraction was found to be correlated with the source flux. The pulse profiles were found to be consisted of two peaks, separated by a phase difference of ∼0.5. During the entire outburst duration, the pulsar was found to exhibit a significant spin-up trend, which was interpreted as a sign of disc accretion. The pulsar continuum spectrum in 3-20 keV range was described with a power law model modified with a cut-off at higher energies. Apart from the continuum emission, an iron line complex in 6.4-6.8 keV range was also detected

in the pulsar spectrum for the first time. The origin of this feature was attributed to the emission from cold iron atoms along with H- or He-like ionized gas around the neutron star. These authors explained the observed variations of spectral and timing parameters in terms of disc accretion except at low-flux durations where a temporary accretion geometry change was speculated (İnam et al., 2004).

In the following sections, a detailed spectral and timing investigation of 2S 1417-624 during its 2009 outburst is presented. Using the observations made with the *RXTE*, we investigated the evolution of pulse profiles, accretion geometry, and variation in spectral parameters of the pulsar during the outburst.

3.2 Observations and data reduction

As mentioned in Chapter-2, the *RXTE* was operational between December 1995 and January 2012. During this period, 2S 1417-624 caught into featuring giant X-ray outburst events twice (i.e., once during 1999 and then again in 2009). The peak X-ray intensity of 2S 1417-624, as recorded in *Swift*/BAT during the 2009 outburst was $\sim$ 300 mCrab (Krimm et al., 2009). The pulsar was monitored at multiple epochs with the *RXTE* during this giant outburst. A total of 39 pointed observations of the pulsar were carried out, covering the rising as well as declining phase of the outburst (between 2 November 2009 to 30 December 2009). A log of these observations is presented in Table 3.1. These observations provided a total effective exposure of $\sim$133 ks and are marked by blue vertical lines across the 15-50 keV light curve of the pulsar (Figure 3.1) obtained from the Swift/BAT monitoring data (Krimm et al., 2013). Two additional horizontal arrows in the figure indicate the beginning and the end of the *RXTE* pointed observations of the pulsar.

For the timing studies, the Standard-1 binned mode data from PCA detectors were utilized to study the variations in the pulse profile of the pulsar with luminosity. Using *saextrct* task of `FTOOLS`, the source light curves were extracted in 2-60 keV energy range with the minimum time resolution allowed by this mode i.e., 0.125 s. Corresponding background light curves were

Table 3.1: Log of the *RXTE* pointed observations of the pulsar 2S 1417-624 during 2009 outburst.

Observation ID	Start Time (MJD)	Exp. Time (sec)	Spin period[a] (sec)	Observation ID	Start Time (MJD)	Exp. Time (sec)	Spin period[a] (sec)
94032-02-01-00	55137.08	3824	17.512(3)	94032-02-05-01	55162.07	3296	17.496(3)
94032-02-01-01	55137.47	2848	17.512(2)	94032-02-05-02	55163.97	3296	17.492(8)
94032-02-01-02	55137.86	7504	17.510(9)	94032-02-05-03	55165.80	3296	17.490(3)
94032-02-01-03	55138.67	896	17.51(2)	94032-02-05-04	55165.93	3312	17.490(8)
94032-02-01-04	55138.47	864	17.50(1)	94032-02-06-00	55169.85	3200	17.484(9)
94032-02-01-05	55138.54	992	17.5(1)	94032-02-06-01	55171.82	2448	17.49(3)
94032-02-01-06	55140.36	9486	17.508(8)	94032-02-06-02	55169.92	3104	17.483(4)
94032-02-02-00	55142.32	4608	17.506(7)	94032-02-06-03	55171.90	1712	17.481(9)
94032-02-02-01	55144.28	4000	17.504(9)	94032-02-06-04	55171.96	1712	17.480(7)
94032-02-02-02	55146.38	3648	17.503(3)	94444-01-01-00	55177.64	3552	17.474(6)
94032-02-02-03	55146.32	2064	17.503(2)	94444-01-01-01	55180.83	3152	17.471(8)
94032-02-03-00	55148.40	3568	17.500(3)	94444-01-02-00	55174.89	2640	17.479(5)
94032-02-03-01	55150.04	3408	17.499(6)	94444-01-03-00	55183.01	2512	17.469(8)
94032-02-03-03	55154.03	3120	17.503(8)	94444-01-03-01	55186.01	3776	17.467(3)
94032-02-03-04	55152.19	3424	17.501(4)	94444-01-03-02	55187.96	3776	17.465(7)
94032-02-03-05	55152.26	3408	17.500(3)	94444-01-03-03	55189.88	3776	17.464(7)
94032-02-04-00	55156.12	3344	17.504(5)	94444-01-03-05	55188.07	3344	17.466(3)
94032-02-04-01	55158.21	5552	17.502(9)	94444-01-04-00	55192.80	3152	17.464(7)
94032-02-04-02	55159.98	3296	17.5(1)	94444-01-04-01	55195.20	4640	17.468(4)
94032-02-05-00	55167.89	3296	17.486(4)				

[a] : The error on the spin period is estimated by fitting a Gaussian function on the chi-squared versus period distribution curve and is quoted for 1 σ level.

generated from the Standard-2 data by using background model provided by the instrument team. Barycentric correction was then applied on the background subtracted light curves to incorporate the motion of satellite and Earth to the barycentre of the Solar system by using *faxbary* task of `FTOOLS`. Moreover, in order to understand the change in the beam pattern of the pulsar with photon energy, we generated energy resolved light curves of the pulsar. For this purpose, we utilized the GoodXenon data by applying *make_se* task on the raw event files.

For the spectral analysis, we used the Standard-2 PCA and Cluster-B HEXTE data. The response files specific to each observational epoch of PCA were constructed by using the *pcarsp* task of `FTOOLS`. Standard procedures, as described in *RXTE* cookbook[1] were adopted to reduce the data obtained from the HEXTE clusters. For phase-resolved spectroscopy, we used GoodXenon data that have a total of 256 energy channels. The background data files were generated from the corresponding Standard-2 data file with the help of *pcabackest* task with *"fullspec=yes"* option. For HEXTE data, the response files were generated with the *hxtrsp* task. The deadtime correction was also applied on the HEXTE spectra by using the task *hxtdead*. All of the standard reduction procedures and step by step reduction guide for phase-resolved spectroscopy can be found in the *RXTE cookbook* at *RXTE Guest Observer Facility*[2].

3.3 Timing Analysis

After following the procedures described in the previous section, background subtracted source light curves were generated for all the observations with a time resolution of 0.125 s. Thereafter, we searched for pulse period of the pulsar during each observation by using *efsearch* task of `FTOOLS` (as described in Chapter-2, Section 4.2.2). The resulting spin period from individual observation is listed in Table 3.1. The corresponding barycentric corrected spin frequency of the pulsar was thus found to be in the range of 57.1–57.25 mHz, and is shown

[1] `https://heasarc.gsfc.nasa.gov/docs/xte/recipes/cook_book.html`
[2] `https://heasarc.gsfc.nasa.gov/docs/xte/recipes/pulse_phase.html`

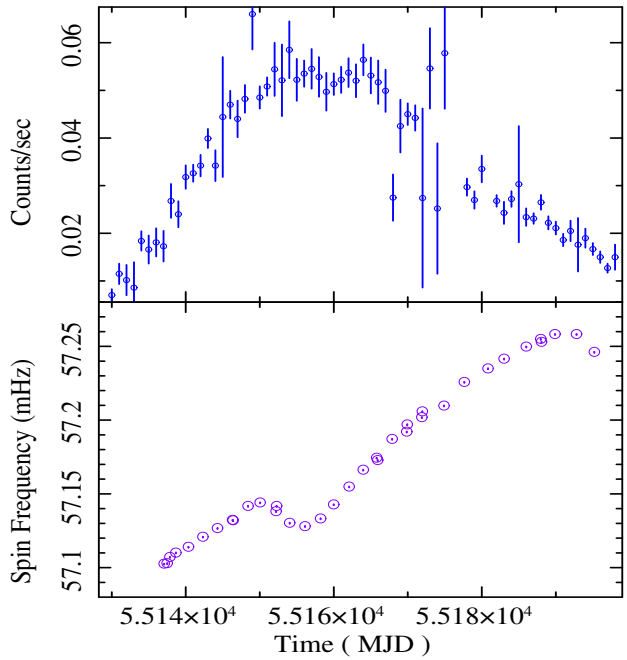

Figure 3.2: Barycentric corrected spin frequency of 2S 1417-624 obtained from the *RXTE* pointed observations of the pulsar. Upper panel shows the *Swift*/BAT light curve of the pulsar in 15-50 keV energy range and the bottom panel indicates the spin frequencies derived from respective *RXTE*/PCA observations during the outburst.

in Figure 3.2. On the top of an increasing trend, one can clearly notice the bump in the spin frequency of the pulsar. This bump corresponds to the orbital modulation of the pulsar about its companion. It has already been studied previously by many authors to derive the precise orbital parameters of the system (Finger et al. 1996; Raichur & Paul 2010). Therefore, we have not carried out orbital modelling in the present study.

3.3.1 Luminosity dependent pulse profiles

The pulse profiles were generated by folding the light curves at their respective spin periods determined from corresponding epoch of the observations. This was done in order to understand the evolution of the pulse profile with luminosity and as the outburst progressed. While generating the pulse profiles for all the pointed observations, we have chosen the folding epoch close to the start time of the respective observation and then adjusted in such a way that the minima of the pulse profiles align at phase zero. Some of the representative pulse profiles in 2-60 keV range are shown in Figure 3.3. These profiles are arranged sequentially as the outburst progressed. The start time of respective observation (in MJD), is quoted on the left

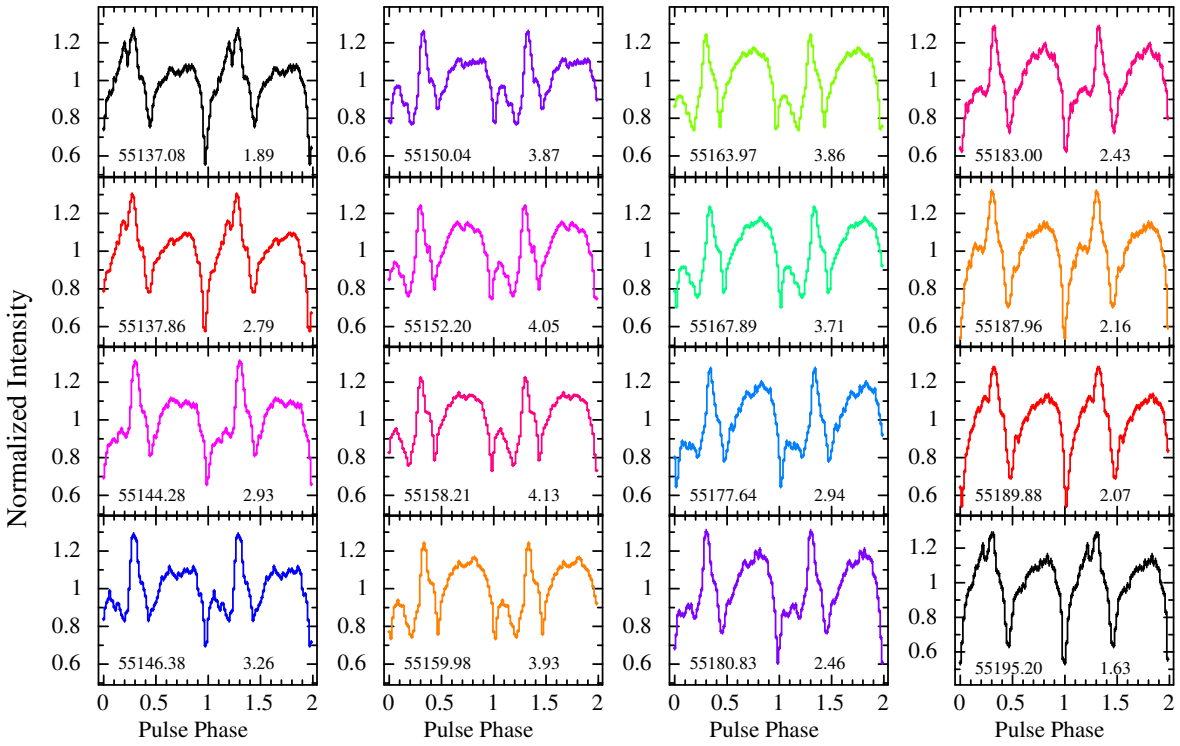

Figure 3.3: Pulse profiles of the pulsar at different phases of the 2009 giant X-ray outburst (from rise to decline). The profiles were generated by folding the 2-60 keV light curves from PCA data at the respective spin periods. The numbers quoted on the left and right side of each panel indicate the beginning of the corresponding *RXTE* pointed observation (in MJD) and the flux (in 10^{-9} erg s^{-1} cm^{-2} units) calculated in 3-30 keV energy range, respectively. Two pulses are shown in each panel for clarity. The error-bars represent 1σ uncertainties.

side of each panel whereas the number quoted on right side represents the estimated flux in 3-30 keV energy range, which is determined from the spectral fitting (discussed in the next section).

A careful investigation of Figure 3.3 indicates a systematic evolution of the pulse profiles with the source flux. At lower intensity, the pulse profiles appeared as double peaked with each peak separated by a pulse phase of ∼0.5. As the outburst progressed towards the maximum intensity (MJD 55146–55158), the peak appearing in 0-0.5 phase range evolved and gradually splitted into two components, thereby effectively producing a triple-peaked profile at a flux level of $\geq 3.2\times10^{-9}$ erg cm^{-2} s^{-1} (corresponding luminosity = 4.6×10^{37} erg s^{-1} by assuming the source distance as 11 kpc) (Grindlay et al. 1984; İnam et al. 2004). The pulsar then restored back to its double-peaked profile shape as the outburst faded. Although the luminosity dependent behaviour of the pulse profiles has already been noticed for several pulsars e.g. EXO 2030+375 (Epili et al. (2017) and references therein) and GX 304-1 (Jaisawal

et al., 2016), the luminosity dependence for 2S 1417-624 is reported for the first time in present thesis work. Moreover, it is also worth mentioning that the shape of profile was consistent at comparable luminosities irrespective of rising and declining phases of the outburst (see first and last panels of Figure 3.3).

3.3.2 Energy resolved pulse profiles

In order to understand the evolution of the emission geometry of pulsar with photon energy, we investigated the energy dependence of the pulse profiles. As described in Section 3.2, energy resolved light curves were created for two different luminosities of the pulsar i.e. one during the onset of the outburst (MJD 55144.28; third panel of Figure 3.3) and the other at the peak of the outburst (MJD 55152.20; sixth panel of Figure 3.3). The pulse profiles of the pulsar showed remarkable energy dependence at different luminosities (see Figure 3.4 and Figure 3.5, respectively). It is clearly evident that the energy evolution of the first peak (0–0.5 phase range) in pulse profile was found to be faster than the second peak at late phases (0.5–1.0 phase range).

At the same time, we also noticed that the energy evolution of the pulse profile at lower luminosity level was relatively simpler (Figure 3.4) as compared to the brightest observation at the peak of the outburst (Figure 3.5). During the latter observation, triple peaks are observed in the profile at energies below 15 keV (Figure 3.5). However with increasing energy, the peak between 0.0 and 0.2 phase range gradually disappeared from the pulse profile in hard X-rays. We also noticed that the peak in 0.2-0.5 phase range was strongly energy dependent that evolved into a narrow component at higher energy, as seen in case of lower luminosity (Figure 3.4). The prominent evolution of this component led to a minor phase shift of $\sim$0.1 phase between the minima of soft (2–6 keV) and hard X-ray profiles (above 30 keV). Also, in case of pulse profiles at lower luminosity, a broad structure in 0.5–1.0 phase range was also detected. This component became narrower with energy though the peak intensity was almost constant across the energy ranges. Pulsations were detected in the light curves up to

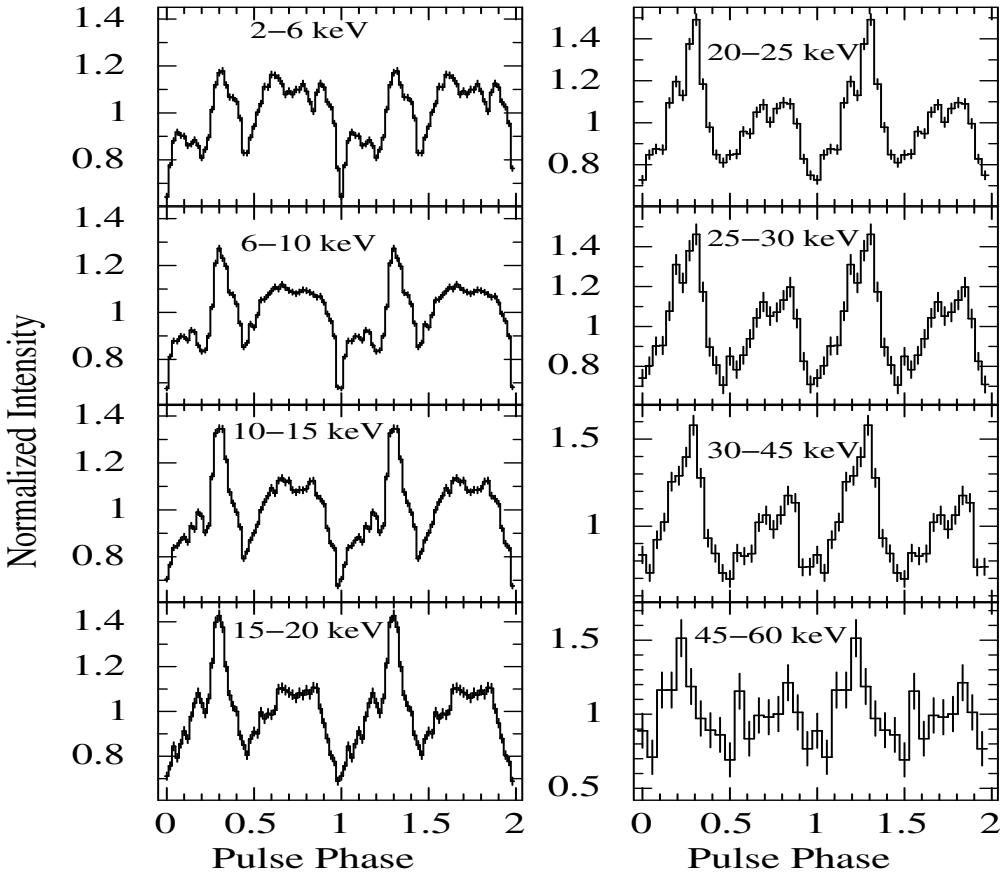

Figure 3.4: Energy resolved pulse profiles of 2S 1417-624 obtained from the *RXTE* observation of the pulsar on 2009 November 9 (MJD 55144.28) at the rising phase of the giant outburst. A double-peaked profile can be clearly seen in all the panels of the figure. The error-bars represent 1σ uncertainties. Two pulses in each panel are shown for clarity.

$\sim$60 keV in both representative pulse profiles at different luminosities of the pulsar.

3.3.3 Anti-correlation of pulsed fraction with source flux

The pulse fraction (hereafter, PF) of the pulsar is defined as the ratio between the difference of maximum (hereafter, I(max)) and minimum intensities (herafter I(min)) and the sum of maximum and minimum intensities in the pulse profiles, and can be expressed as:

$$PF = \frac{I(max) - I(min)}{I(max) + I(min)} \tag{3.1}$$

In order to quantify the fraction of X-ray photons contributing to the pulsation, we estimated pulse fraction in 2–60 keV range for all the observations. Figure 3.6 shows the variation of pulse fraction with the source flux (estimated in 3–30 keV energy range through spectral fit-

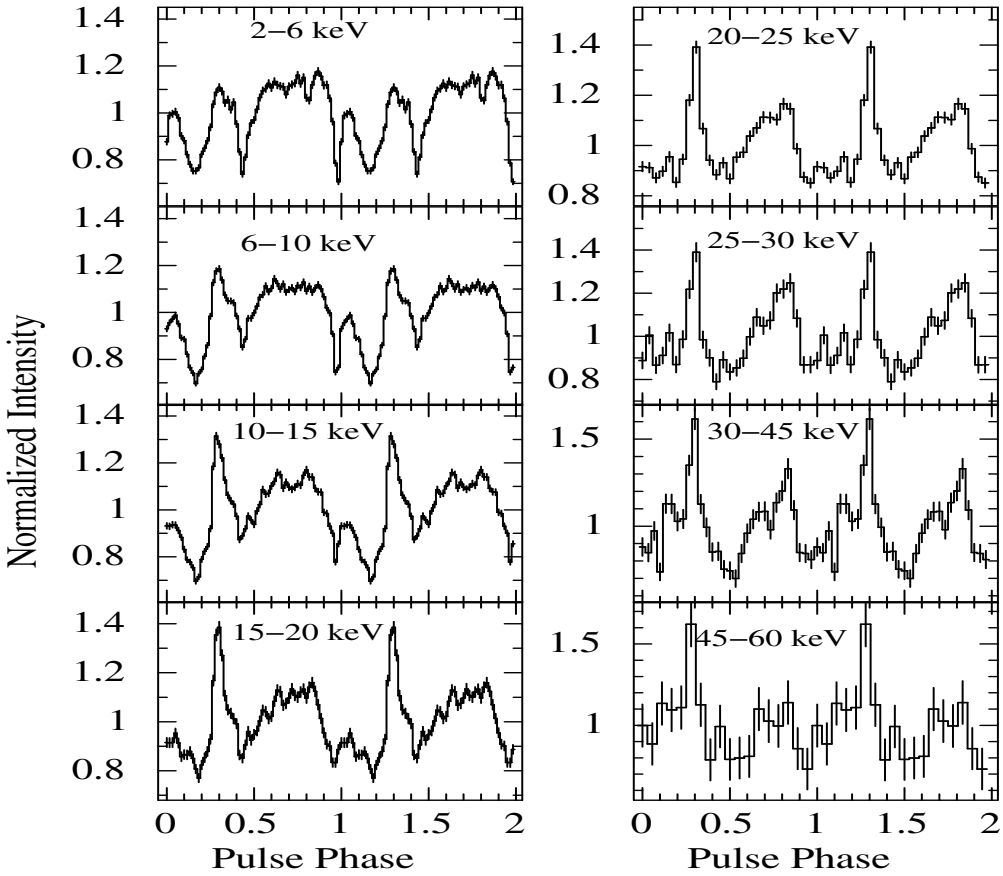

Figure 3.5: Energy resolved pulse profiles of 2S 1417-624 obtained from the *RXTE* observation on 2009 November 17 (MJD 55152.20) near the peak of the giant outburst. A triple-peaked profile can be clearly visible in soft X-ray pulse profiles that evolved into a double peaked structure at higher energies. The error-bars represent 1σ uncertainties. Two pulses in each panel are shown for clarity.

ting). An anti-correlation is clearly evident from Figure 3.6, although a correlation is expected from the pulsar in case of directly beamed emission. The correlation between pulse fraction and the source flux can be easily understood in terms of simple geometrical arrangement i.e., toy-model of the pulsar as proposed by Lutovinov & Tsygankov (2009). This model assumes a simple dipole geometry of the magnetic field of the pulsar. It further assumes a particular alignment in which the spin and magnetic axes are inclined with respect to the line of sight of observer in such a way that the observer could only see the one complete pole while the other one is partially occulted. As described in Chapter-1, the growth of the accretion column above the magnetic poles of the pulsar depends upon the mass accretion rate (luminosity). As the mass accretion rate increases (during the outburst episodes) the observer can only see one complete column (above one magnetic pole) while the upper part of the accretion column becomes visible (for the second pole), due to the inclined geometry. Moreover, as pointed out

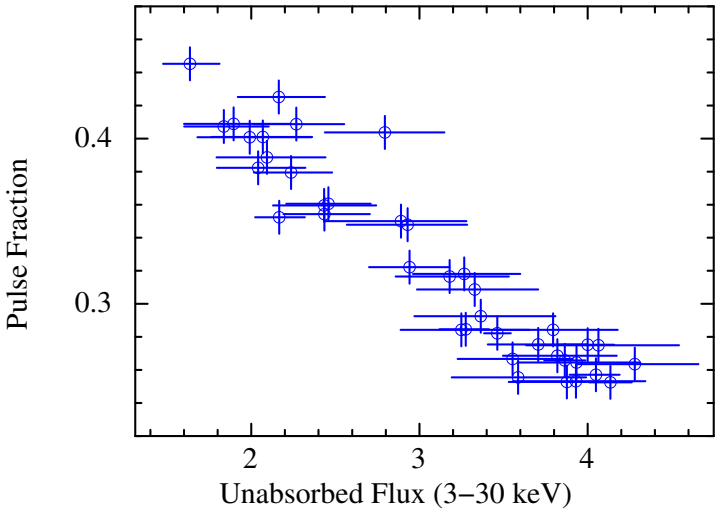

Figure 3.6: Variation of Pulse fraction of the pulsar with the 3–30 keV unabsorbed flux (in 10^{-9} erg s^{-1} cm^{-2} units) estimated from the spectral fitting of data obtained from *RXTE*/PCA observations. The associated errors are calculated for 1σ confidence level.

by Basko & Sunyaev (1976), there is a strong temperature gradient in the accretion column, ranging from highest at the column base (thermal mound) to the lowest at upper parts (where comptonization processes occur). This not only explain the correlation of PF with luminosity but also the transition of two peaked profile to single peaked profile. However, in the present study, an anti-correlation between the PF and the source luminosity is observed. This result is counter-intuitive and will be discussed in Section 5 in more detail.

3.4 Spectral Analysis

In the present study, we have witnessed a peculiar evolution of pulse profile with the photon energy and source luminosity. This motivated us to carry out a detailed spectral studies of the pulsar during the entire outburst. For that purpose, we extracted phase-averaged spectra of individual observations to trace the changes in spectral parameters across the outburst. Moreover, due to the presence of dip-like features observed in the pulse profile of the pulsar at higher luminosity, we decided to explore this evolution further through phase-resolved spectroscopy. The results of these studies are summarized below.

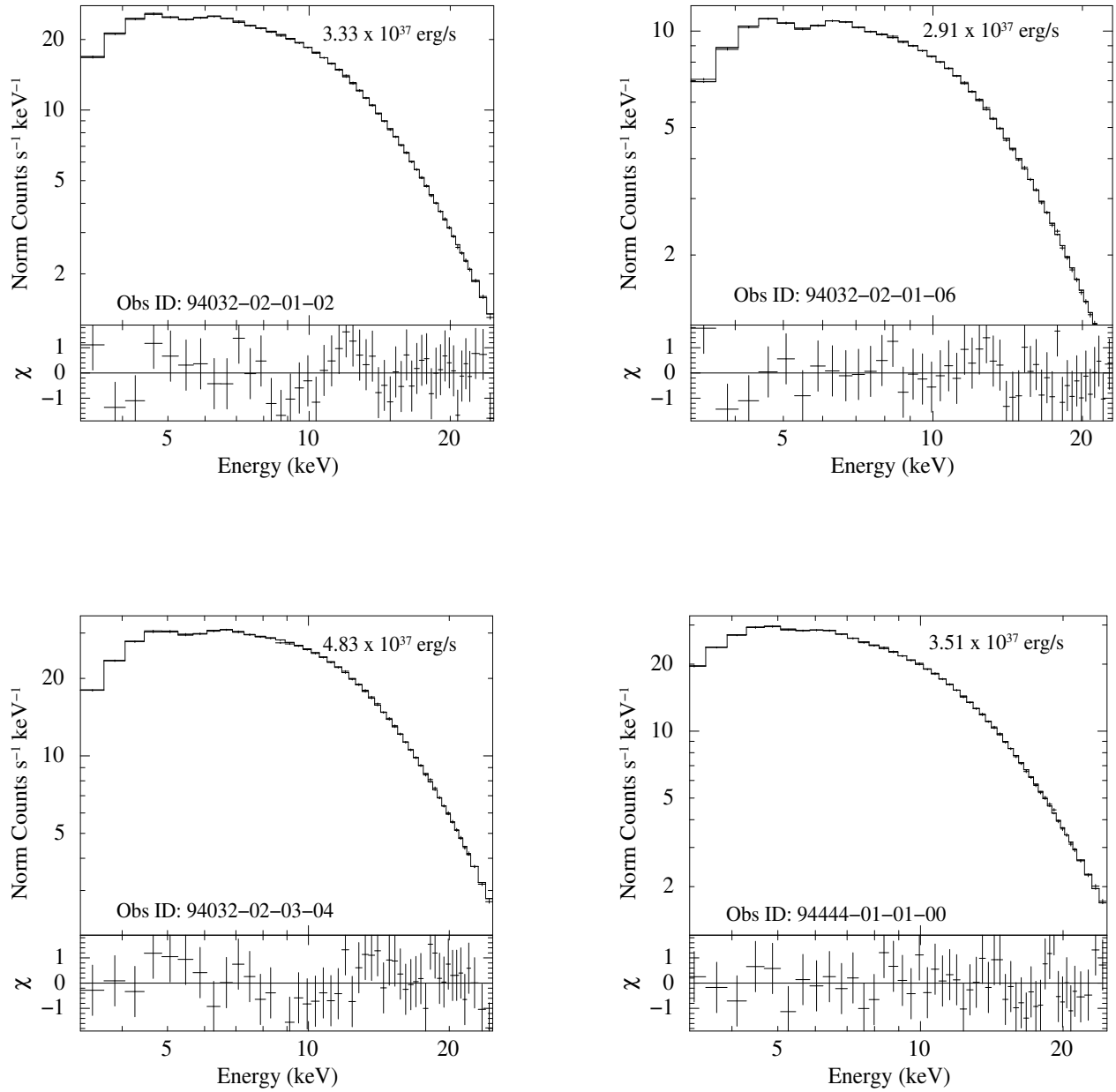

Figure 3.7: Representative *RXTE*/PCA spectra of the pulsar 2S 1417-624 for four epochs of observation at different luminosities during the rising as well as declining phases of the outburst. Each individual Obs-ID is fitted with the cut-off power law model and the corresponding best-fit spectral parameters are reported in Table 3.2. The luminosity of the pulsar during each observation is quoted on the top right of each panel.

3.4.1 Phase-averaged Spectroscopy

The pulse phase-averaged spectroscopy was carried out by using all available *RXTE* observations of the pulsar during the 2009 giant outburst. The source and background spectra were extracted by following the procedures as described in Section 3.2. `XSPEC` package of version 12.8.2 was used to carry out the spectral fitting of the individual observations of the pulsar. Spectra fitting was carried out in 3-30 keV energy range (from PCA data) from all the observations in order to have a comparison of spectral parameters with luminosity. In Figure 3.7, four representative energy spectra, spanning over wide luminosity range (i.e., from the rising phase to the declining phase of the outburst) are presented. However, at the peak of the outburst, the data from HEXTE instrument (15–70 keV range) were also used. A systematic error of 1.0% was added to the pulsar spectra obtained from the RXTE/PCA, as suggested by the instrument team. For the spectral fitting in 3-30 keV energy range, we attempted several conventional continuum models such as negative and positive exponential cut-off, Fermi-Dirac cut-off, cut-off power law, and high-energy cut-off power law continuum models (as discussed in Chapter-2). Apart from the phenomenological models, a physically motivated model `CompTT` was also used to fit the pulsar spectrum. However, this model yielded a poor fit with a reduced-χ^2 $\geq$2. During the spectral fitting, an absorbed cut-off power law and high-energy cut-off power law models were found to best describe the pulsar spectra obtained from all the *RXTE* observations. At the same time, an iron fluorescent emission line at $\sim$6.4 keV was clearly detected in all the epochs of observation, except at the lower luminosities (during the rising and decling phase of the outburst). The values of parameters obtained from our spectral fitting are listed in Table 3.2. A representative broad-band spectrum in 3–70 keV range, obtained from the simultaneous fitting of PCA and HEXTE data (acquired at the peak of the giant outburst; Obs. ID: 94032-02-03-03) and the best-fit model are shown in the top panel of Figure 3.8. The residuals obtained from the spectral fitting are shown in the bottom panel of the figure.

In Figure 3.9, we present the change in spectral parameters of the pulsar with the 3–30 keV

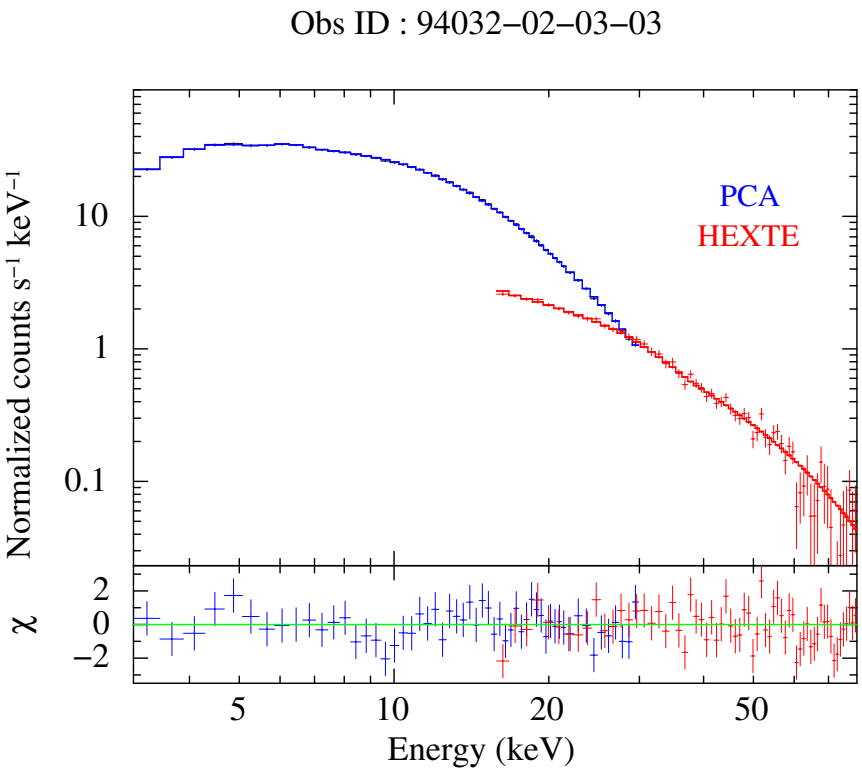

Figure 3.8: Broad-band spectrum of 2S 1417-624 in the 3-70 keV energy range (at the peak of the outburst; Obs-ID : 94032-02-03-03) and the best-fit model consisting of a cutoff power law model along with a Gaussian function at 6.4 keV for iron emission line are shown in the top panel. The bottom panel shows the contributions of the residuals to the χ^2.

unabsorbed source flux, obtained from fitting the *RXTE*/PCA spectra with a cut-off power-law continuum model (as described above). The parameters such as power-law photon index and cut-off energy are found to show interesting variations with the 3–30 keV unabsorbed flux. The pulsar spectrum became harder with the increase in luminosity. At the same time, the cut-off energy was also increased with the increasing luminosity. Apart from the photon index and cut-off energy, the column density (N_H) which was variable in the range of (1-6) $\times$ 10^{22} cm^{-2}, was found to be anticorrelated with the source flux. The estimated values of N_H was found to be marginally higher than the value of absorption column density in the direction of the source. The cut-off energy, however, did not show any dependence on the power-law photon index.

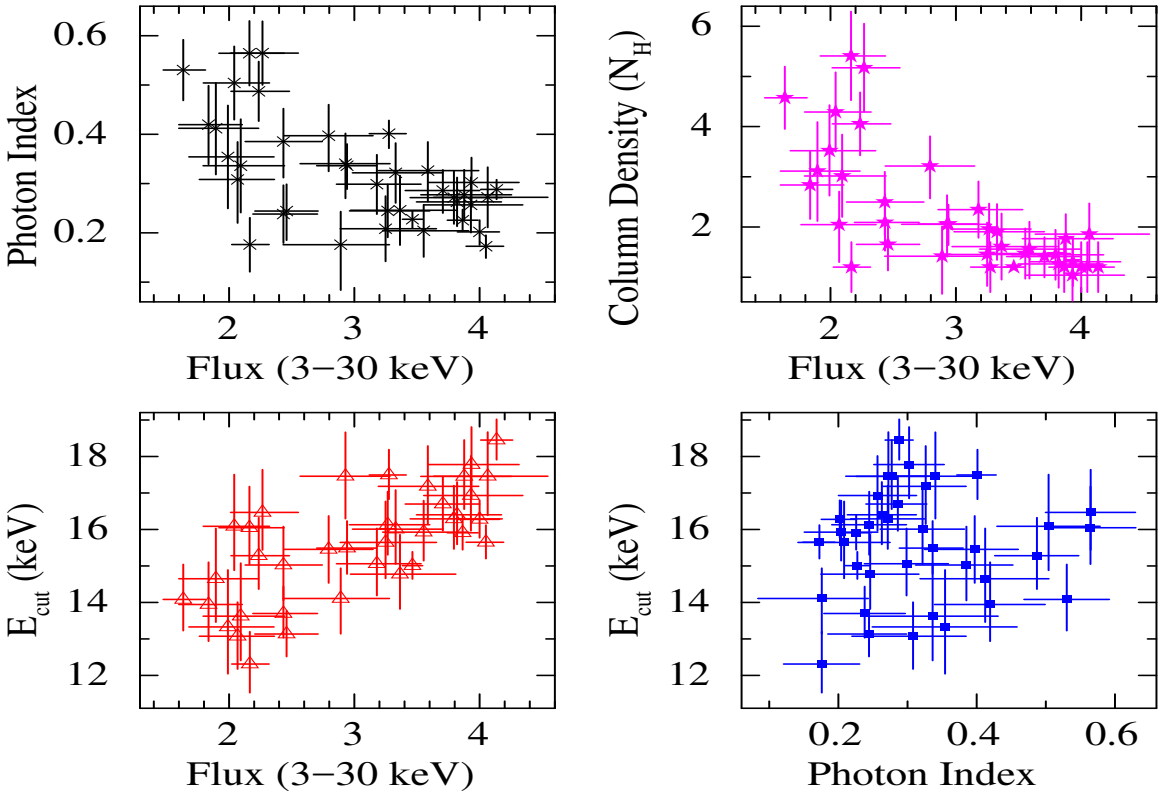

Figure 3.9: Variation of spectral parameters such as power-law photon index, absorption column density, cutoff energy with unabsorbed source flux in 3–30 keV range, obtained from the fitting of *RXTE*/PCA data with a cutoff power law continuum model. The error-bars are estimated for 90% confidence level.

3.4.2 Phase-resolved Spectroscopy

Phase-resolved spectroscopy of the pulsar was carried out by using *RXTE* observations at rising phase and peak of the giant X-ray outburst in 2009 (same IDs, selected to generate the energy resolved pulse profiles). This was done in order to understand the emission geometry, cause of pulse profile evolution from double- to triple-peaked profile and investigate the changes in spectral parameters over pulse phases. For this, the source and background spectra were extracted from GoodXenon mode data of PCA by following the standard procedure as described in the *RXTE cookbook*. We selected two representative observations with Obs. IDs 94032-02-01-06 (rising phase of the outburst; see left panel of Figure 3.10) and 94032-02-03-04 (peak of the outburst; see right panel of Figure 3.10) to extract phase-resolved spectra. Using appropriate background and response files, the 3–30 keV spectrum for each phase bin (a total of 10 and 9 phase bins for ID 94032-02-01-06 and 94032-02-03-04 were chosen, respectively) was fitted with a high-energy cut-off power law as well as cut-off power-law continuum

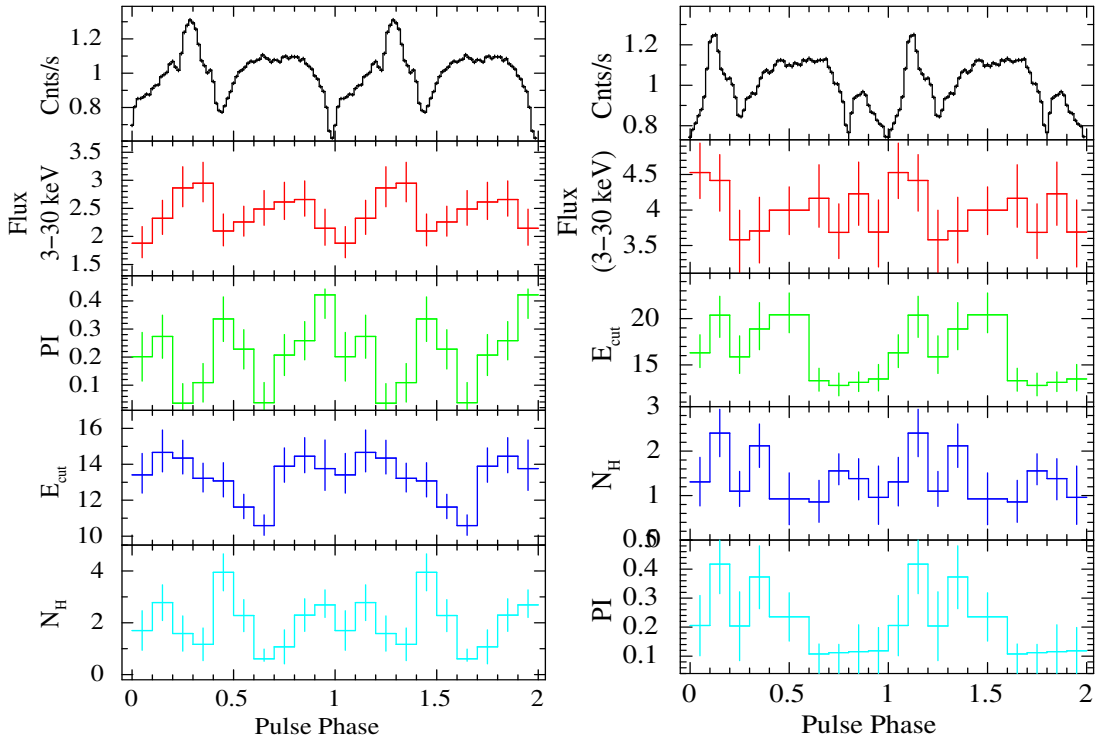

Figure 3.10: Variation of phase resolved spectral parameters such as power-law photon index, absorption column density, cutoff energy with unabsorbed source flux in 3–30 keV range, obtained from the fitting of two Observation IDs i.e., 94032-02-01-06 (left panel; 10 phase bins) and 94032-02-03-04 (right panel; 9 phase bins), of *RXTE*/PCA data with best-fit cutoff power law continuum model. The error-bars are estimated for 90% confidence level.

models along with a Gaussian function for iron emission line, as in case of phase-averaged spectroscopy. While fitting, the width of the iron emission line was kept fixed at 0.1 keV. A systematic error of 1% was also added to the phase-resolved spectra.

It was found that both the models yielded acceptable fits with comparable statistical significance on the spectral parameters. Phase-resolved spectroscopy of *RXTE* observations of the pulsar at the rising phase and at the peak of the 2009 giant outburst, however, did not yield any significant and systematic variation of spectral parameters over the pulse phases. For instance, the unabsorbed flux in 3–30 keV range was found to follow similar pattern with pulse phase as that of the 3–10 and 10–30 keV pulse profiles of the pulsar (see Figure 3.10). Other parameters such as power-law photon index, cut-off energy, and absorption column density did not show any systematic variation with pulse phase for both the observations. Moreover, in order to explore the possibility of potential correlation between the phase resolved spectral parameters, a correlation study has been done. It is clearly evident from Figure 3.11, that the cut-off energy does not show any specific dependence on the power-law photon index.

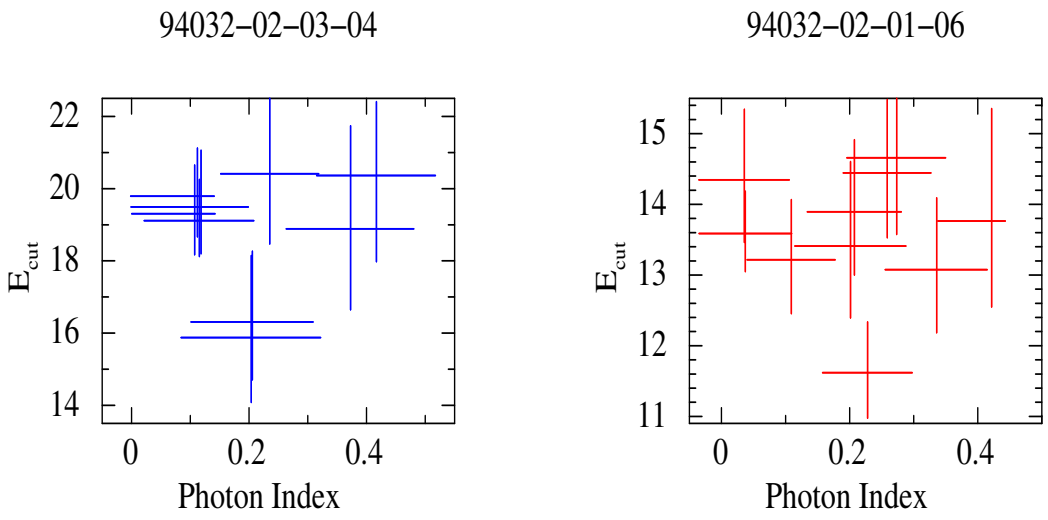

Figure 3.11: A potential correlation study between the phase resolved spectral parameters : photon index and cut-off enrgy. The results for two Obs IDs are presented and respective observation is quoted on the top of the figure. The error-bars are estimated for 90% confidence level.

Therefore, it is difficult to draw any meaningful conclusion from phase-resolved spectroscopy of the *RXTE* observations of the pulsar during the 2009 giant X-ray outburst.

3.5 Discussion and conclusions

In the present work, a comprehensive spectral and timing analysis of the Be/X-ray binary pulsar 2S 1417-624 has been carried out by using *RXTE* observations during a giant outburst in 2009. One of the most intriguing result emerging from this study is the peculiar changes in the pulse profiles of the pulsar with source luminosity. During most of the earlier observations, the pulse profiles of the pulsar were double-peaked and showed a marginal energy dependence. However, from our timing studies of 2S 1417-624, an interesting evolution of the pulse profile has been uncovered for the first time. A double-peaked profile at lower luminosity was found to evolve into a triple-peaked structure with increasing luminosity. This kind of variation had not been seen earlier in 2S 1417-624 during any other Type I and Type II (giant) X-ray outbursts (Finger et al. 1996; İnam et al. 2004). However, this kind of behaviour is not unique to 2S 1417-624. Several other Be/X-ray binary pulsars such as EXO 2030+375 (Naik et al. 2013; Naik & Jaisawal 2015; Epili et al. 2017), GX 304-1 (Jaisawal et al., 2016) also show multiple peaks in the pulse profile during X-ray outbursts. Extensive studies have already

Table 3.2: Best-fit spectral parameters of 2S 1417-624 obtained from fitting the *RXTE*/PCA data during the 2009 giant outburst with a cutoff power-law model. The errors are quoted for 90% confidence level.

Obs-id	N_H [a]	Photon index	E_{cut} (keV)	Line energy (keV)	Eq. width (eV)	Reduced-χ^2 (d.o.f)	Unabsorbed flux[b] (3-30 keV)
94032-02-01-00	3.2±0.9	0.41±0.09	14.6±1.4	6.52±0.27	55±28	1.17(43)	1.89±0.34
94032-02-01-02	3.2±0.6	0.39±0.06	15.4±0.9	6.34±0.21	128±60	1.10(42)	2.79±0.35
94032-02-01-06	2.1±0.5	0.23±0.05	13.7±0.7	6.43±0.15	71±22	0.50(47)	2.43±0.27
94032-02-02-00	1.4±0.6	0.17±0.06	14.1±0.8	6.26±0.16	133±78	1.01(45)	2.89±0.38
94032-02-02-01	2.1±0.6	0.34±0.06	17.4±1.2	6.35±0.18	80±50	0.84(48)	2.92±0.35
94032-02-02-02	1.9±0.6	0.24±0.05	16.1±0.9	6.28±0.19	60±23	0.89(50)	3.26±0.33
94032-02-02-03	1.4±0.7	0.20±0.06	15.6±1.2	6.32±0.12	90±23	0.67(49)	3.24±0.41
94032-02-03-00	1.5±0.5	0.20±0.05	15.9±0.9	6.26±0.17	71±22	1.04(50)	3.55±0.35
94032-02-03-01	1.7±0.5	0.27±0.05	17.4±1.0	6.38±0.15	75±22	1.15(50)	3.87±0.37
94032-02-03-03	1.1±0.2	0.20±0.02	16.3±0.5	6.18±0.21	120±60	0.72(50)	3.99±0.15
94032-02-03-04	1.1±0.2	0.17±0.02	15.6±0.5	6.18±0.19	103±50	0.65(49)	4.04±0.14
94032-02-03-05	1.8±0.7	0.27±0.06	17.4±1.2	6.39±0.17	61±24	0.85(49)	4.06±0.47
94032-02-04-01	1.4±0.3	0.28±0.01	18.4±0.6	6.30±0.16	98±37	0.67(49)	4.13±0.12
94032-02-04-02	1.0±0.5	0.25±0.05	16.9±1.1	6.28±0.15	75±23	0.71(46)	3.93±0.41
94032-02-05-00	1.4±0.4	0.28±0.04	16.7±0.7	6.31±0.13	69±31	0.86(49)	3.70±0.29
94032-02-05-01	1.3±0.5	0.30±0.05	17.8±1.0	6.39±0.16	67±22	0.81(50)	3.93±0.37
94032-02-05-02	1.1±0.2	0.22±0.02	15.9±0.5	6.29±0.21	71±32	0.57(49)	3.86±0.12
94032-02-05-03	1.1±0.5	0.27±0.05	16.3±0.9	6.22±0.21	66±23	0.63(50)	3.79±0.38
94032-02-05-04	1.2±0.5	0.26±0.04	16.4±0.9	6.31±0.11	81±18	0.79(49)	3.82±0.35
94032-02-06-00	1.5±0.6	0.32±0.05	17.2±1.1	6.37±0.16	82±42	0.83(48)	3.58±0.4
94032-02-06-01	1.0±0.4	0.40±0.02	17.5±0.7	6.39±0.16	64±39	0.55(47)	3.27±0.13
94032-02-06-02	1.3±0.2	0.22±0.01	15.0±0.4	6.45±0.12	69±13	0.88(48)	3.46±0.08
94032-02-06-03	1.9±0.5	0.32±0.06	16.1±1.1	6.50±0.25	55±24	0.92(50)	3.32±0.37
94032-02-06-04	1.6±0.7	0.24±0.07	14.8±1.0	6.24±0.14	76±25	0.79(49)	3.36±0.44
94444-01-01-00	2.0±0.4	0.33±0.04	15.5±0.7	6.53±0.14	68±30	1.05(45)	2.94±0.23
94444-01-01-01	1.6±0.5	0.24±0.05	13.1±0.7	6.44±0.16	99±40	0.91(48)	2.45±0.25
94444-01-02-00	2.3±0.6	0.29±0.06	15.0±1.0	6.39±0.16	59±21	0.53(47)	3.17±0.35
94444-01-03-00	2.5±0.6	0.38±0.06	15.0±1.1	6.57±0.23	72±52	1.11(48)	2.43±0.3
94444-01-03-03	2.0±0.7	0.30±0.07	13.1±0.9	6.47±0.27	101±64	0.99(43)	2.06±0.29
94444-01-04-00	2.8±0.7	0.41±0.07	13.9±1.2	6.59±0.32	60±28	1.27(45)	1.83±0.26
94032-02-01-01	4.3±0.8	0.5±0.07	16.1±1.4	–	–	1.12(47)	2.04±0.28
94032-02-01-03	2.0±0.4	0.17±0.05	12.3±0.9	–	–	1.02(45)	2.16±0.15
94032-02-01-04	3.5±1.0	0.35±0.1	13.3±1.6	–	–	0.73(51)	1.99±0.36
94032-02-01-05	3.0±0.8	0.33±0.09	13.6±1.5	–	–	1.04(47)	2.09±0.34
94444-01-03-01	5.1±0.2	0.56±0.06	16.5±1.2	–	–	0.87(50)	2.26±0.28
94444-01-03-02	5.4±0.9	0.56±0.06	16.1±1.1	–	–	0.85(50)	2.16±0.27
94444-01-03-05	4.0±0.7	0.48±0.06	15.3±1.0	–	–	1.27(47)	2.23±0.24
94444-01-04-01	4.5±0.7	0.53±0.06	14.1±0.9	–	–	0.86(47)	1.63±0.17

[a] : Equivalent hydrogen column density in the unit of 10^{22} cm^{-2}; [b] : in unit of 10^{-9} erg s^{-1} cm^{-2}.

been performed to understand the cause of the dip-like structures in the pulse profiles of these pulsars. The pulse phase-resolved spectroscopy of the observations during X-ray outbursts from these transient pulsars showed the presence of additional matter at dip phases. This indicates that the dips in the pulse profiles are originated due to the absorption/obscuration of X-ray photons by narrow streams of matter that are phase-locked with the pulsar.

Interestingly enough, we have witnessed the evolution of a broad peak (in 0-0.5 phase range; Figure 3.3) in the pulse profile into two peaks at a flux level of $\sim 3\times10^{-9}$ erg s^{-1} cm^{-2}, which further evolved into three peaks at brighter phases of the giant outburst. Nevertheless, the source intensity was found to be relatively high i.e. $\sim 2.7\times10^{-9}$ erg s^{-1} cm^{-2} in 3-20 keV range during the 2009 outburst compared to the previous outburst events when the peak flux of the pulsar was observed to be $\sim 1.7\times10^{-9}$ erg s^{-1} cm^{-2} in above energy range (İnam et al., 2004). This could be a possible reason that a double-peaked profile was only observed during the earlier studies. To explore the origin of multiple peaks at brighter phases of the pulsar, we have performed phase-resolved spectroscopy at two different luminosities. However, our results only showed moderate variation in the column density across the pulse phases in contrast to other Be/X-ray binary pulsars. Though, the observed column density (1-5 $\times$ 10^{22} cm^{-2}) was found to be marginally higher than the Galactic value ($\sim 1.4\times10^{22}$ cm^{-2}) along the line of sight, it is not sufficient to produce a remarkable dip or affect the beam function up to $\sim$20 keV, as seen in Figure 3.4. At the same time, we note that the limited low-energy coverage of the *RXTE*/PCA ($\sim$3 keV) may be one of the reason that constrained the column density measurement.

Another possible explanation for the presence of dip-like features in the pulse profiles of 2S 1417-624, could be due to the critical luminosity of the pulsar during the 2009 giant outburst. If we assume a source distance of 11 kpc (Grindlay et al. 1984; İnam et al. 2004), the 3-30 keV unabsorbed luminosity was calculated to be in range of $\sim$(2.4-6) $\times$ 10^{37} erg s^{-1}. Since the distance to the source is poorly constrained, we also estimated the luminosity values by assuming a distance of 5 kpc and it was found to be variable from 4.8×10^{36} to 1.2×10^{37} erg s^{-1}. For the considered values of source distance, the pulsar luminosity was

estimated to be in the order of 10^{37} erg s^{-1} which is the typical value of critical luminosity for accretion powered X-ray pulsars (Becker et al. 2012; Reig & Nespoli 2013; Mushtukov et al. 2015). As described in Chapter-1, the critical luminosity of an accretion powered X-ray pulsar is crucial to understand the transition between two accretion regimes i.e. sub-critical and super-critical phases (Basko & Sunyaev 1976; Becker et al. 2012). At lower luminosity (sub-critical phase), the accretion flow is expected to halt by Coulomb interaction close to the neutron star surface. In this regime, the high energy emission is dominated by a pencil beam (propagating parallel to the magnetic field) or pulsed component (Basko & Sunyaev, 1976). This component may produce a single or double peaked pulse profile depending on the visibility of the emission regions at poles of the neutron star. With increasing mass accretion rate, the radiation pressure takes lead and upscatters the accreting plasma particles in the presence of a radiation dominated shock above the surface. The X-ray photons emitted in this situation mostly diffuse through the side wall of the accretion column in the form of a fan beam pattern (perpendicular to magnetic field lines). This kind of pattern is un-pulsed and may produce a complex pulse profile, as seen in present study. Becker et al. (2012) has calculated the critical luminosity by considering various physical processes in the accretion column which can be expressed as

$$\begin{aligned} L_{\rm crit} &= 1.49\times10^{37}{\rm erg\,s^{-1}}\left(\frac{\Lambda}{0.1}\right)^{-7/5} w^{-28/15} \\ &\times\left(\frac{M}{1.4\,{\rm M_\odot}}\right)^{29/30}\left(\frac{R}{10\,{\rm km}}\right)^{1/10}\left(\frac{B}{10^{12}\,{\rm G}}\right)^{16/15} \end{aligned} \tag{3.2}$$

where R, M and B are the radius, mass and magnetic field (in 10^{12} G) of the neutron star, respectively. The constant Λ characterizes the mode of accretion which is assumed as 0.1 (for disk accretion) in our case. While the parameter ω represents the shape of the photon spectrum and considered as 1 (Becker & Wolff, 2007b). By plugging in the value of these

parameters in Equation 3.2 and for reasonable assumptions, above equation reduces to

$$L_{\rm crit} \;=\; 1.49 \times 10^{37} \left(\frac{B}{10^{12}\,{\rm G}} \right)^{16/15} {\rm erg\,s^{-1}} \tag{3.3}$$

By substituting the magnetic field value i.e., $9{\times}10^{11}$ G (reported by İnam et al. (2004) from the 1999 giant X-ray outburst studies of the pulsar) in above equation, the value of critical luminosity for the pulsar 2S 1417-624 is calculated to be $\sim$1.33$\times10^{37}$ erg s^{-1}. This estimate matches well with the observed luminosity ranges for considered distances, indicating that the pulsar was emitting close to the critical luminosity regime during the 2009 giant outburst. For sub-critical (below critical luminosity) sources, the emission geometry is expected to be simple i.e. described by a pencil beam pattern from the pulsating component. Thus, the presence of two peaks with individual peaks separated by $\sim$0.5 pulse phase in the profile, suggests a simple beam function originated from both the poles of the neutron star during outburst. As the source approaches the critical luminosity, the contribution from the un-pulsed photons escaping through side walls of the column increases. This increase may influence the total beam geometry and produce multiple peaks in the pulse profile, as seen in our study. This interpretation is further supported by the observed anti-correlation between pulsed fraction and source flux, as shown in Figure 3.6. A higher pulse fraction is expected from a pulsar in case of directly beamed emission. The increasing contribution of the fan beam enhances the un-pulsed component or decreases the pulsed component at higher luminosity from the pulsar. This results a negative correlation in the pulse fraction with luminosity, as observed in our study. Other sources in luminosity range of 10^{35}–10^{37} erg s^{-1} e.g. SXP 1323 (Yang et al., 2018), have also shown a negative trend with source intensity. Furthermore, the reflection from the neutron star surface can also contribute to un-pulsed radiations at higher luminosity (Mushtukov et al., 2018). Therefore, we suggest that the changes in pulse morphology from a double to a triple peaked profile is associated with the change in beam pattern at a luminosity close to the critical luminosity of the pulsar.

Apart from the timing studies, the results obtained from the spectral studies also support

this idea. The spectral parameters trace an interesting evolution as the outburst progressed. The photon index was found to be anti-correlated with the unabsorbed flux (see Figure 3.9), indicating that the spectrum became harder during the bright phase of the outburst. It is Interesting to note that the observed power-law photon index during the 2009 outburst (in 0.1–0.6 range) is found to be lower than the earlier reported values (in 0.8–2.5 range) by İnam et al. (2004). These authors also found a clear negative correlation between the photon index and source flux in (0.01–1) $\times$ 10^{-9} erg s^{-1} cm^{-2} range as in the present case. Along with the negative correlation between the photon index and source flux, the values of photon index are found to be clustered in (3–4) $\times$ 10^{-9} erg s^{-1} cm^{-2} flux range.

The pattern of distribution of power-law photon index with source flux (Figure 3.9) has been observed in pulsars accreting in sub-critical regime or close to the critical luminosity (Reig & Nespoli 2013; Postnov et al. 2015; Epili et al. 2017 and references therein). Reig & Nespoli (2013) performed a systematic analysis on a few Be/XRB pulsars during gaint outbursts to identify the different accretion modes of pulsar i.e., sub-critical and super-critical accretion regimes. In their study, the value of critical luminosity was found to be in range $\sim(1-4)\times10^{37}$ erg s^{-1}. Our estimates of the value of critical luminosity matches well with that of Reig & Nespoli (2013). Moreover, it is worth mentioning that the critical luminosity estimated in the present study also matches well with the recent estimates by Ji et al. (2020) using HXMT and NICER observations during 2019 outburst of 2S 1417-624. This is another independent confirmation of our findings.

In our study, the height of the pulsar emission region is considered to be in the range of a few kilometers (see Becker et al. 2012). With increase in mass accretion rate, the height of the emission region gets reduced. At the same time, increase in the optical depth of the accretion column leads to the origin of harder spectra (or negative correlation) in the sub-critical regime. Nevertheless, the cutoff energy also showed a positive trend with the source flux. This parameter is associated with the plasma temperature and indicates the temperature enhancement of emission region with increasing luminosity (Soong et al. 1990; Unger et al. 1992). The presence of clustered values of photon index in (3–4) $\times$ 10^{-9} erg s^{-1} cm^{-2} flux

range can be associated with the transition from sub-critical to super-critical regimes during the giant outburst. Therefore, the results from our spectral analysis also support the idea of accretion transition close to the critical luminosity of the pulsar 2S 1417-624 during the giant outburst. Accretion powered X-ray pulsars have strong magnetic field in the order of $\sim 10^{12}$ G. Detection of absorption features in 10–100 keV range pulsar spectrum, known as cyclotron resonance scattering features, provides direct estimation of the pulsar magnetic field (Jaisawal & Naik, 2017). However, in the present case, no such feature was detected in the pulsar spectra even at the peak of the giant outburst. One possible reason behind the non detection of cyclotron feature in the present case could be that the cyclotron line is expected to be outside the range of X-ray spectrum of the pulsar with *RXTE*/PCA. In their study, İnam et al. (2004) reported the value of magnetic field to be $\sim 9 \times 10^{11}$G. However, more recently Ji et al. (2020) reported the value of magnetic field of 2S 1417-624 to be around 7×10^{12}G, based on accretion torque theory (Ghosh & Lamb, 1979). Considering above estimates for the magnetic field of 2S 1417-624, the cyclotron line energy is expected to be found outside the energy range of *RXTE*/PCA (see equation 1.19, Chapter 1). As the pulsar is faint at hard X-rays, the *RXTE*/HEXTE data are not usable in spectral fitting.

Chapter 4

NuSTAR observation of 2S 1417-624 during 2018 giant outburst

In the previous chapter, a peculiar behaviour of the Be/X-ray binary pulsar 2S 1417-624 with luminosity has been established. Coincidentally, the pulsar went into another giant X-ray outburst during the course of this thesis work, i.e. in March 2018. The pulsar was observed simultaneously with *NuSTAR* and *Swift* observatories at the peak of the recent giant outburst. This provided another oppertunity to investigate the properties of the pulsar at a higher luminosity by using data from instruments with improved broad-band spectral capability. Below we present a comprehensive timing and spectral studies of the pulsar during its 2018 giant outburst event. The main objective of this chapter is to expand our knowledge on the characteristic properties of the source to higher luminosities compared to that during the earlier outbursts with *RXTE* data. Another important aspect of this work is the implementation of recently developed physical models (Becker & Wolff, 2007b; Farinelli et al., 2012) to infer the emission mechanism from the neutron star surface. Although the observed spectrum of accretion powered X-ray pulsars have been widely modelled with phenomenalogical models (as discussed in Section 5 of Chapter-2), these models do not give complete insight into the physical parameters related with the emission processes. In order to comprehend the situation, many attempts have been made in the past few decades to model the observed emission

from the accreting X-ray pulsars (Basko & Sunyaev 1975; Langer & Rappaport 1982; Harding et al. 1984). However, only recently it has become possible to model the spectral continuum of accreting pulsars with a reasonable set of approximations (see Becker & Wolff 2007b; Farinelli et al. 2012). Both of these models are discussed in this chapter in great detail.

4.1 Observations and data reduction

After the decline of 2009 giant outburst, 2S 1417-624 entered into a long quiscence state for about 9 years untill it showed an X-ray brightening again on 24 March 2018 (MJD 58201; Nakajima et al. 2018). The source flux increased steadily afterwards and peaked on 2018 April 30 (MJD 58238; Krimm et al. 2018), corresponding to a flux of ∼350 mCrab in 15-50 keV energy range. The *Swift*/BAT monitoring light curve of the source during 2018 gaint outburst event, is presented in Figure 4.1. The pulsar was observed with the *NuSTAR* and *Swift* observatories simultaneously at the peak of the outburst, as indicated by the vertical arrow mark in Figure 4.1. A detailed log of these observations along with the effective exposure time of the respective observation, is reported in Table 4.1. In order to have a systematic analysis of source properties with luminosity, we have also analyzed an *RXTE*/PCA (Jahoda et al. 1996) observation of 2S 1417-624 acquired at the peak of the 2009 outburst (ObsID 94032-02-04-01). Since the procedure for *RXTE* data reduction (see Chapter-2, Section 2.4.1) and analysis have already been explained in detail in Chapter-3 (see Section 3.2), it is not required to discuss here again.

We followed standard procedures[1] to analyze the *NuSTAR* data (as already described in Section 2.4.3, in detail). A circular region of 120 arc-sec, centered on the source coordinates, was used to accumulate the source products and a background region of same size was chosen from the source free region, to avoid the contamination from source photons. The *Swift*/XRT complemented our present study on exploring the source properties at high luminosity, in soft X-ray (0.9-10 keV) energy ranges, alongwith the simultaneous hard X-ray observation of the pulsar with the *NuSTAR* observatory. During the time of observation, the *Swift*/XRT

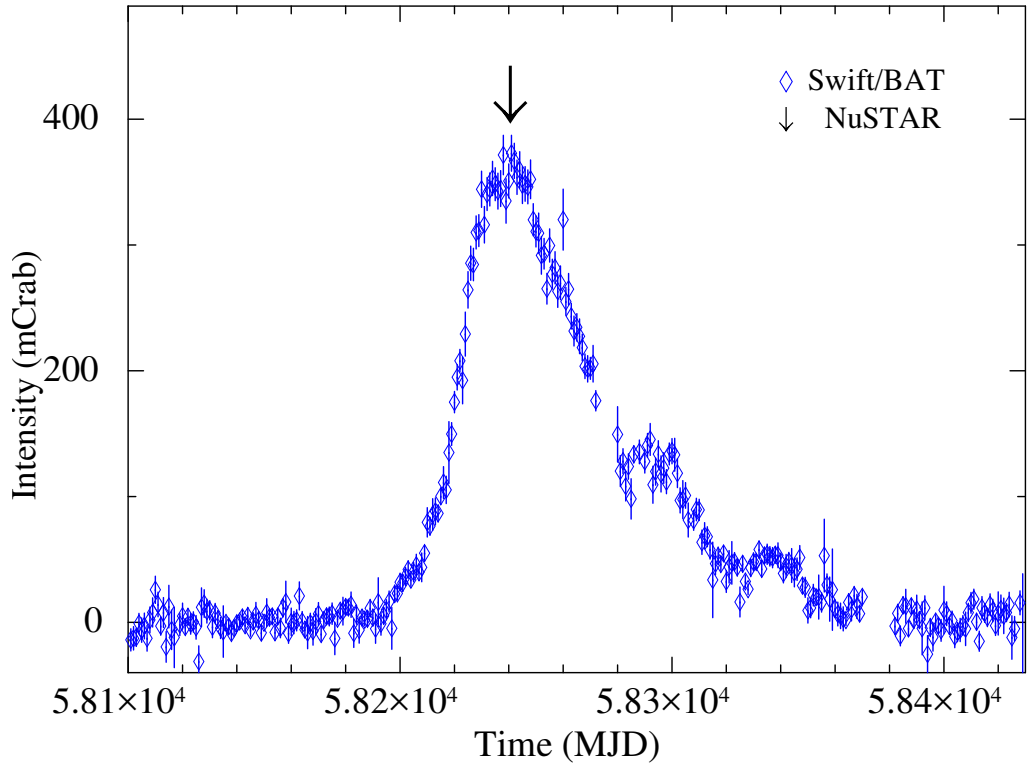

Figure 4.1: The *Swift*/BAT monitoring light curve (in 15-50 keV energy range) of 2S 1417-624 during 2018 giant outburst. The arrow mark on the top of light curve indicates the start time of simultaneous *NuSTAR* and *Swift* observations of the pulsar.

was operational in window timing mode (see Section 2.2.2 for various operating modes of XRT). Standard procedures, already described in Section 2.4.2, were followed to extract the source and background products. A rectangular region of 20×40 pixels centered on the source position, was considered to extract the source products. The background estimation was done in similar manner by considering the same size in the outer regions of the CCD. To check the possibility of photon pile-up on the CCD, the source light curve with the minimum time resolution allowed by this mode i.e., 2.5 s, was created and examined. The average source count rate during the entire observation was variable around ∼13 counts s^{-1} (i.e. <100 counts s^{-1}), thereby avoiding the pile-up effectively.

4.2 Timing Analysis

For timing analysis, the source and background light curves with a time resolution of 0.1 s were extracted from the *NuSTAR* and *Swift*/XRT data. Barycentric correction was then

[1]https://heasarc.gsfc.nasa.gov/docs/nustar/analysis/

Table 4.1: Log of the pointed observations of 2S 1417-624 used in this work.

Observatory/Instrument	ObsID	Start Time (MJD)	Exposure (ksec)	Pulse Period (sec)
NuSTAR/FPMs	90402318002	58240.57	28.8	17.475(6)
Swift/XRT	00088676001	58240.81	1.8	17.47(5)
RXTE/PCA	94032-02-04-01	55158.21	3.4[1]	17.502(9)

[1] : See Section 1.2 in text.

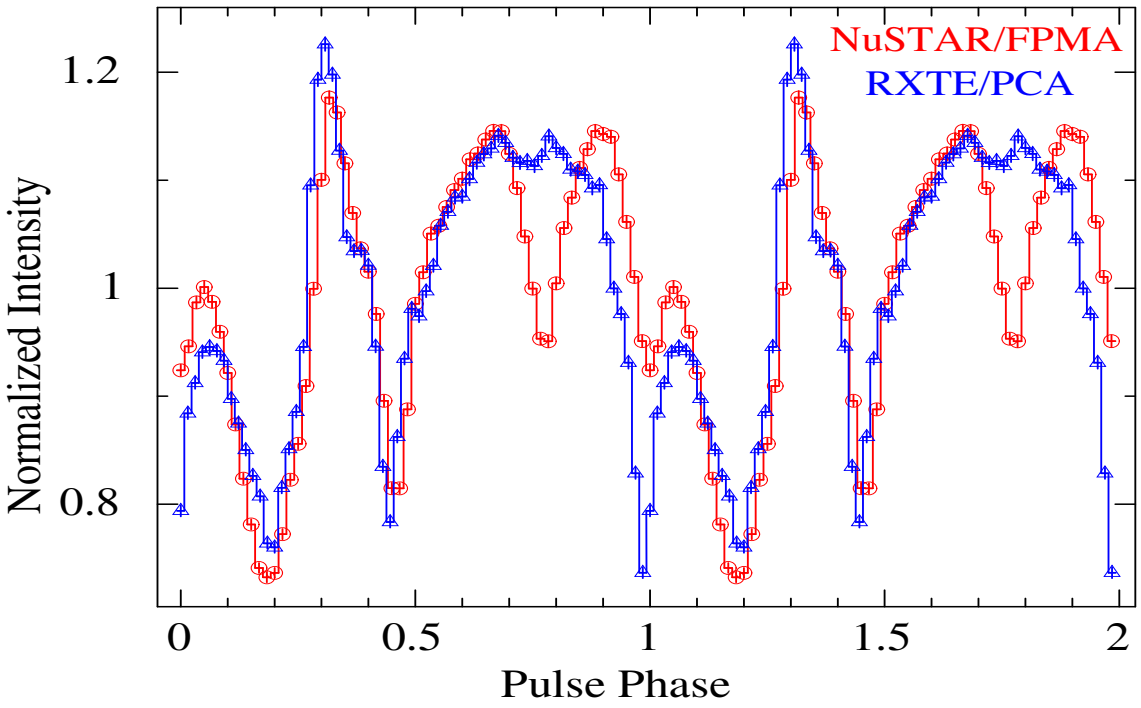

Figure 4.2: The *NuSTAR* and *RXTE* pulse profiles of 2S 1417-624 at the peaks of 2018 and 2009 giant outbursts are shown in red circles and blue triangles, respectively. In order to have a better comparision, the pulse profiles are shown in 3–60 keV energy range for both the epochs of observations. Both the pulse profiles are plotted for 64 phase bins. Pulse profiles of the pulsar during the *NuSTAR* and *RXTE* observations were generated by using the estimated pulse period during corresponding observation. Two pulses are shown in each panel for clarity.

applied on the background subtracted source light curves. The χ^2-maximization technique i.e, *efsearch* task (as described in Chapter-2; Leahy 1987) was utilized to estimate the spin period of the pulsar. Pulsations at a period of 17.475(6) s and 17.47(5) s were detected in the source light curves from the *NuSTAR* and *Swift*/XRT observations, respectively. The error on the pulse period value is estimated by fitting a Gaussian function on the chi-squared versus period distribution and is quoted for 1 σ level, unless stated otherwise.

We have also estimated the spin period of the pulsar by using independent methods already described in Chapter-2, such as `CLEAN` (Roberts et al., 1987) and Lomb-Scargle periodogram (Lomb, 1976; Scargle, 1982; Horne & Baliunas, 1986) as implemented in the `PERIOD` program distributed with STARLINK Software Collection[2]. A consistent spin period value of 17.475(1) s was derived from above methods. Moreover, in order to check the significance of the power peak in the periodogram, we calculated the False Alarm Probability (FAP; Horne & Baliunas 1986) and it was found to be significant above 95 per cent. However, the quoted value of uncertainity derived from these methods only corresponds to the minimum error on the period. It is also worth mentioning that the error on the estimated period is notoriously difficult to calculate. The only reliable estimate could be found via simulation of large number of light curves by implementing Monte Carlo or randomization method (see, e.g., Boldin et al. 2013). Therefore, based on the agreement between the estimated period from independent methods, we adopted 17.475(6) s as the spin period of 2S 1417-624 in our study, which corresponds to the larger value of error among all the methods. Pulse profiles were then constructed by folding the respective light curves at this period.

Further evidence on the evolution of pulse profiles with luminosity

The 2018 giant outburst was the brightest outburst featured by 2S 1417-624 till date (Krimm et al., 2018), thereby providing an opportunity to study the emission geometry of the pulsar at even higher luminosities as compared to previous outburst events. In order to carry out this comparative study, we have made use of an *RXTE* observation at the peak of the 2009 giant

[2]http://starlink.eao.hawaii.edu/starlink

outburst and compared it with the current *NuSTAR* pulse profile (see Figure 4.2). We note that the *NuSTAR* observation was performed at a higher flux level (≈5.14× 10^{-9} erg cm^{-2} s^{-1} in 3–30 keV range) as compared to the previous *RXTE* observation (≈4.13× 10^{-9} erg cm^{-2} s^{-1} in the same energy range). Irrespective of the flux differences, well agreement between the two profiles was observed except for the appearance of an additional dip in 0.7-0.8 phase range of the pulse profile obtained from the *NuSTAR* observation (Figure 4.2). This effectively produced a four-peaked pulse profile as opposed to the three-peaked profile observed with the *RXTE* during the peak of the 2009 giant outburst of the pulsar. This is the clear evidence of the further evolution of pulse profiles with luminosity. Since the pulsar has already featured single- to triple-peaked profiles during its earlier outburst events (Finger et al. 1996; İnam et al. 2004; Raichur & Paul 2010; Gupta et al. 2018), this is the first time it showed four peaks i.e., when the pulsar luminosity was higher as compared to the previous *RXTE* observations in 2009.

Energy resolved pulse profiles

A strong energy dependence of the pulse profiles, seen during previous outburst studies with the *RXTE* observations, motivated us to carry out similar study with the *NuSTAR* and *Swift* data during the 2018 giant outburst. The energy resolved light curves were extracted and folded with the estimated spin period of the pulsar and are presented in Figure 4.3. This was done in order to understand the evolution of individual peaks and the emission geometry of the pulsar with photon energy. From Figure 4.3, it is clear that the pulse profiles are strongly dependent upon energy. The pulse profiles in soft X-ray energy ranges from the *NuSTAR* and *Swift* observations (see panel two and three of Figure 4.3) were found to be consistent. Also, the four peaks in the pulse profiles are visible up to ≈15 keV along with the change in relative intensities of the individual peaks. The evolution of the first peak in 0.0–0.2 phase range is found to be different as compared to other peaks in the sense that it gets narrower and prominent with increasing energy. The hard X-ray pulse profile (in 50–79 keV range)

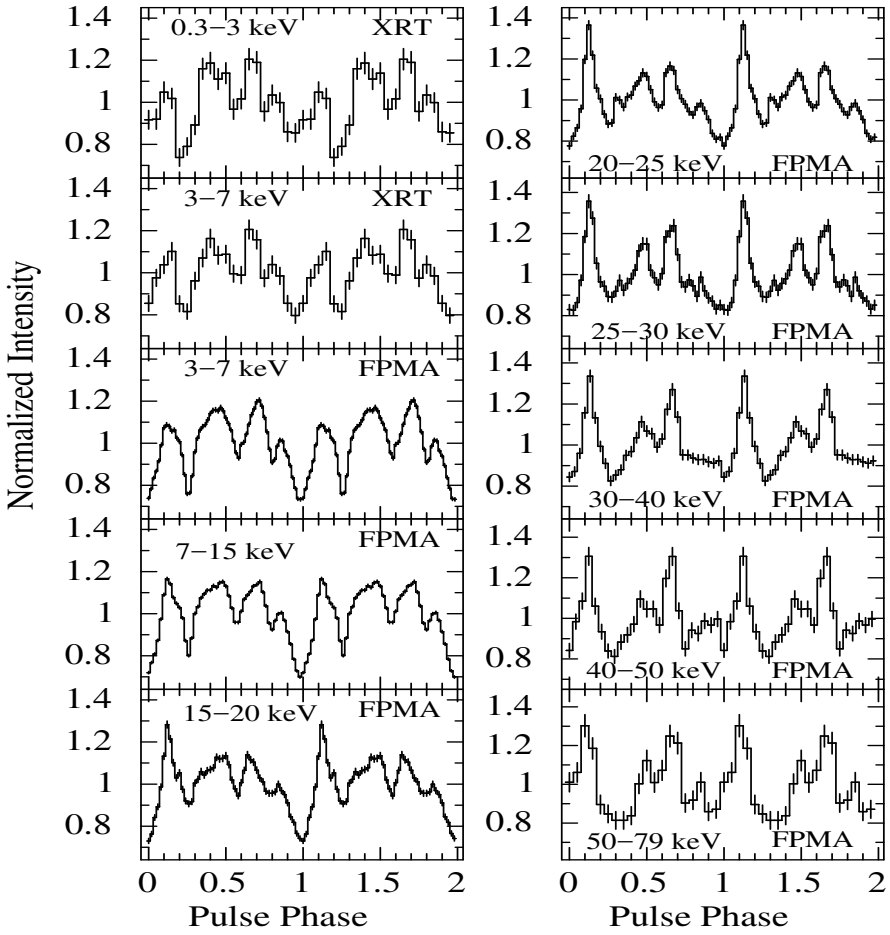

Figure 4.3: Energy resolved pulse profiles of 2S 1417-624, obtained from the *Swift* and *NuSTAR* observations of the pulsar during the 2018 giant outburst. A strong energy dependence of the pulse profiles could be traced easily among successive profiles. The error bars represent 1σ uncertainties. Two pulses are shown in each panel for clarity.

was found to be comparatively simple and appeared double peaked as the intensities of other peaks are reduced at higher energies. This is possibly due to the broadening of the minima (dip) after the first peak with increasing energy. The pulsations were detected in the light curves up to 79 keV. It is also worth mentioning that we noticed a remarkable similarity in the evolution of the pulse profiles of the pulsar during the 2018 *NuSTAR* observation and the *RXTE* observations during 2009 outburst (Gupta et al., 2018), suggesting a similar accretion geometry during both the giant X-ray outbursts.

Energy and luminosity dependence of pulse fraction

Although the *NuSTAR* observatory is operational in 3–79 keV energy range, we have estimated the value of pulse-fraction in 3–60 keV energy band. This was done, in order to have a direct

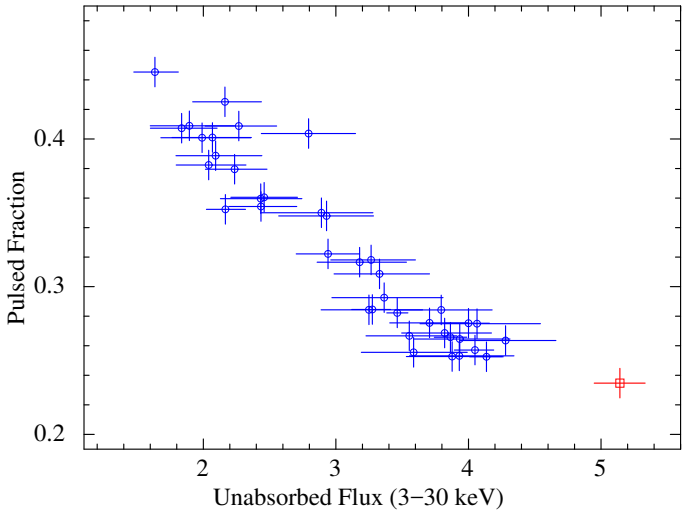

Figure 4.4: Evolution of the pulsed fraction with the 3-30 keV unabsorbed flux (in 10^{-9} erg cm^{-2} s^{-1} units). The blue circles corresponds to the pulsed fraction measured in 2-60 keV energy range with the *RXTE*/PCA during the giant outburst in 2009, while the red rectangle shows the measured value in 3-60 keV band from the *NuSTAR* observation during the 2018 outburst (present work).

comparison with the previous outburst studies in 2009 (Gupta et al., 2018). The pulse-fraction is defined as the ratio between the difference of maximum and minimum intensities and the sum of the maximum and minimum intensities in the folded light curve. The pulse-fraction in 3–60 keV range for the *NuSTAR* observation was estimated to be 23.4±0.4 per cent and is shown in Figure 4.4. The estimated value of pulsed fraction seems to follow the negative correlation trend with the pulsar luminosity as observed during the previous 2009 outburst studies (see Section 3.3.2, Chapter-3). Apart from the dependence of the pulsed fraction on luminosity, we have also studied the change in pulsed fraction with energy (Figure 4.5). It is evident that the pulsed fraction of the pulsar 2S 1417-624 increases with energy, similar to other X-ray pulsars. Energy dependence of the pulsed fraction has been studied extensively for a large sample of transient Be/X-ray binary pulsars by Lutovinov & Tsygankov (2009). Most of the pulsars were found to exhibit a monotonic increase in the pulsed fraction with energy. Some of them additionally showed local features near the cyclotron line energy and its harmonics. The presence of these features has been associated with the effect of resonance absorption. This qualitative explanation for the increase in pulsed fraction with energy is based on a simple geometrical model for the neutron stars with dipole magnetic fields (see Chapter-3, Section 3.3.3 for a detailed description of this model).

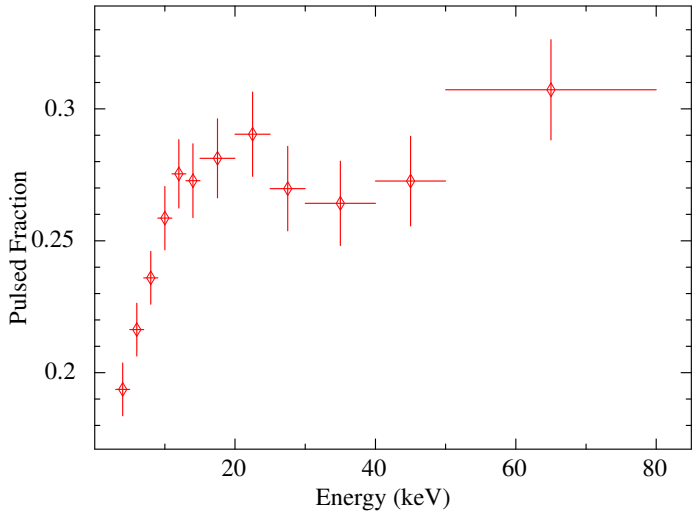

Figure 4.5: Dependence of the pulsed fraction of 2S 1417-624 on energy during the *NuSTAR* observation in 2018. The error bars represent 1σ uncertainties.

4.3 Spectral Analysis

In the following subsections, we describe the phase-averaged spectral modelling of 2S 1417-624 during its 2018 giant outburst, using simultaneous *NuSTAR* and *Swift*/XRT observations. In order to understand the emission properties of the pulsar, we have implemented both physical and phenomenological models. The details of the implemented models can be found in text of the respective sections. Apart from the phase-averaged spectroscopy, we have also performed a detailed pulse phase-resolved spectroscopy of the *NuSTAR* observation. Main motivation behind this study was to understand the cause of the additional dip-like feature (0.7-0.8 phase range; Figure 4.2) observed in the pulse profile. The results obtained from these studies are summarized below.

4.3.1 Phase-averaged Spectroscopy

For the phase-averaged spectroscopy, the source and background spectra were accumulated by following standard procedures as described in Section 1. Using appropriate background, response matrices and effective area files, spectral fitting was carried out in 0.9-79 keV energy range by using `XSPEC` package v12.8.2 . All the model parameters were tied together for the FPMA, FPMB and XRT data in the simultaneous spectral fitting, whereas the relative instrument normalizations were kept free. The cross-normalization constants between the

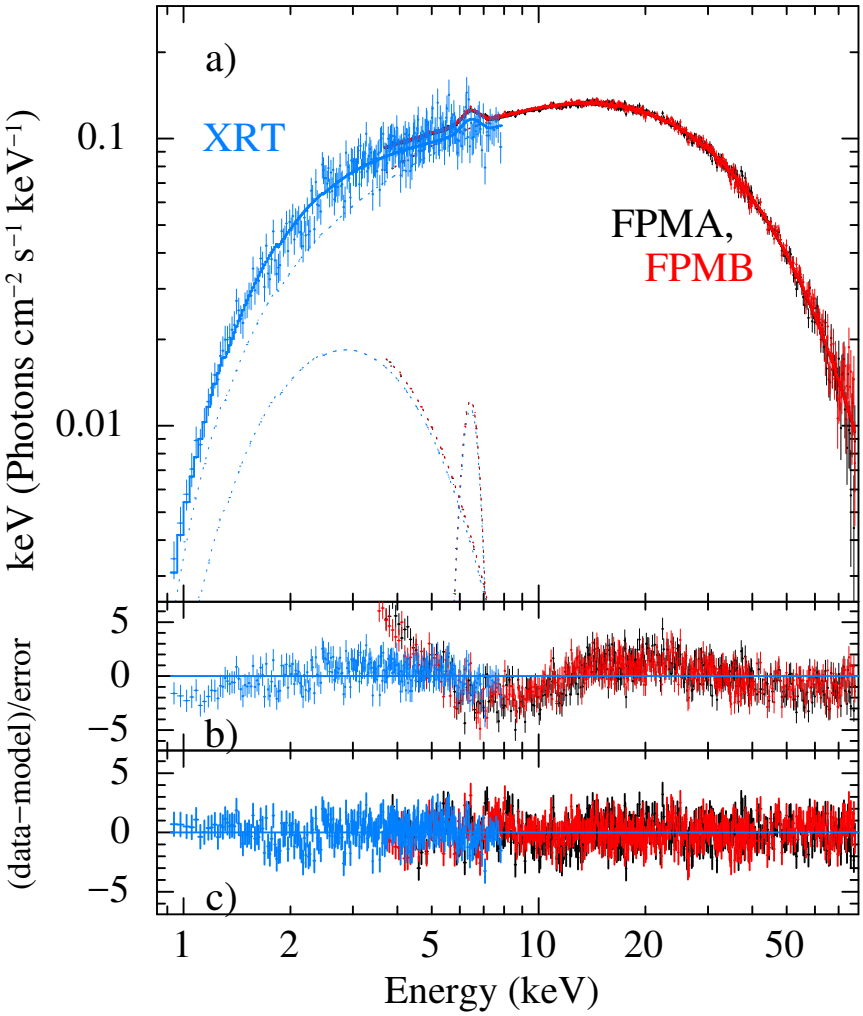

Figure 4.6: (a) : Broad-band continuum spectrum of 2S 1417-624 in 0.9-79 keV energy range, obtained from the *Swift*/XRT (blue), *NuSTAR*-FPMA (black) and -FPMB (red) detectors. The top panel shows the source spectra obtained from above mentioned detectors along with the best fitted model comprising of a cutoff power law continuum model and a blackbody component (Cutoff+BB) modified with the interstellar absorption and a Gaussian function for the iron emission line at 6.4 keV. Panels (b) and (c) show the spectral residuals obtained after fitting the broad-band spectrum, without and with the inclusion of blackbody component, respectively.

detectors were consistent with the values suggested by the instrument teams. While fitting the simultaneous *Swift*/XRT and *NuSTAR* data, we noticed a marginal mismatch between the distribution of data points below 3.5 keV. Therefore, we did not use *NuSTAR* data below 3.5 keV. This mismatch have also been previously reported by several authors in other studies (Bellm et al. 2014; Kühnel et al. 2017).

In the previous studies, the broad-band continuum spectrum of 2S 1417-624 has been widely described with a power law model modified with a cutoff at higher energies. Therefore, we initially approximated the spectrum with a cutoff power law model. Additionally, we detected a fluorescent iron emission line at 6.4 keV. The result of this fitting i.e,

phabs×(CutoffPL + ga), yielded a reduced χ^2 value of >2 and the corresponding residuals are shown in Figure 4.6(b). The presence of wave-like residuals in 1–15 keV energy range of the spectrum and high value of reduced χ^2 made the fitting unacceptable. In order to account for these residuals, we included a thermal blackbody (BB) component with a temperature of ∼1 keV. Addition of this BB component improved the fitting with reduced χ^2 value of ≈1.1 (Figure 4.6(c)). We have also attempted to use partial covering (PC) absorber model component instead of the BB component. A cutoff power law model, modified with a PC component can be expressed as

$$N(E) \;=\; e^{-N_{\rm H1}\sigma(E)}(K_1 + K_2 e^{-N_{\rm H2}\sigma(E)})\; f(E)$$

where

$$\begin{aligned} f(E) &= E^{-\Gamma} && for\ E < E_{\rm c} \\ &= E^{-\Gamma} e^{-\left(\frac{E}{E_{\rm c}}\right)} && for\ E > E_{\rm c} \end{aligned}$$

where, *f(E)* represents the cutoff power-law model with Γ as the power-law photon index, E_c is the cutoff energy in keV. K_1 & K_2 are normalization constants, expressed in the units of photon keV^{-1} cm^{-2} s^{-1}. N_{H1} & N_{H2} are the equivalent Galactic and the additional hydrogen column densities (in units of 10^{22} atoms cm^{-2}), respectively. $\sigma(E)$ is the photoelectric absorption cross-section. As compared to BB component, the result of this fitting yielded a comparable statistical significance and the respective spectral parameters are listed in Table 4.2. Though the pulsar was observed at the highest luminosity till date (at the peak of the 2018 giant X-ray outburst), there was no signature of the presence of any cyclotron resonance scattering feature in the pulsar spectrum in 0.9-79 keV range.

Despite the non-detection of CRSF feature, we performed a comprehensive search for possible CRSF through the inclusion of a multiplicative Gaussian absorption line (Gabs, see

Section 2.6.2 of Chapter-2) with arbitrary fixed energy in the fit (in addition to the best-fit model described above). To determine the upper limit of any absorption line in the spectrum, the width of the line was kept fixed at 1 keV and 2keV in the energy bands of 4-10 keV and 11-78 keV respectively. We found that for all energies, the depth of the line was found to be well below 0.1 (see Figure 4.7). This value is lower than for most other pulsars where CRSFs has been robustly detected (Staubert et al., 2019).

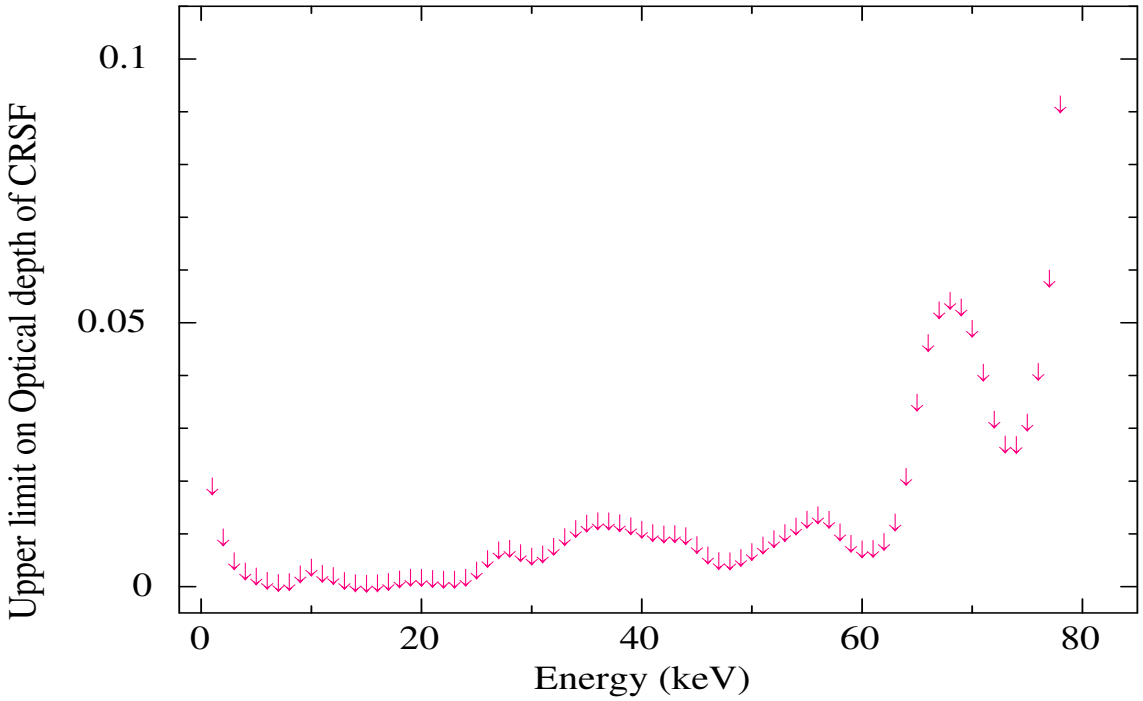

Figure 4.7: The upper limit on the optical depth of a gaussian absorption line (Gabs) as a function of energy.

We also investigated several other standard continuum models (see Chapter-2, Section 2.6.1) such as high energy cutoff power law (HECut), a HECut power law with a smoothing Gaussian at cutoff energy (NewHcut) and negative and positive exponential cutoff (NPEX) models, in order to find a suitable continuum for 2S 1417-624. For all considered models, the addition of BB or a PC component and an iron line at ∼6.4 keV was necessary to describe the pulsar spectrum. The spectral parameters obtained from fitting the broad-band spectrum of the pulsar with these models are listed in Table 4.2. The value of equivalent hydrogen column density obtained from fitting various spectral models was found to be in the range of $\approx$0.6–0.9$\times10^{22}$ cm^{-2}, which is lower than the value of Galactic absorption in the source

Table 4.2: Best-fitting spectral parameters (90% errors) obtained from the simultaneous *NuSTAR* and *Swift*/XRT observations of 2S 1417- 624. The fitted models are (i) High-energy cutoff power law with a blackbody component, (ii) cutoff power law model with blackbody, (iii) NEWHCUT model with a blackbody component, (iv) Cutoff power law modified with a partial covering absorption, and (v) COMPMAG model along with photoelectric absorption component and a Gaussian component for iron emission line.

Parameters	Spectral Models				
	HECut+BB	Cutoff+BB	NEWHCut+BB	CutoffPL(with PC)	COMPMAG
N_{H_1} [a]	0.63±0.05	0.72±0.04	0.69±0.04	0.83±0.04	0.67±0.06
N_{H_2} [b]	–	–	–	168.3±12.4	–
Cov. Fraction	–	–	–	0.16±0.01	–
Photon index	0.12±0.01	0.12±0.01	0.10±0.01	0.37±0.01	–
E_{cut} (keV)	3.1±0.5	15.3±0.2	5.4±0.4	17.04±0.15	–
E_{fold} (keV)	15.3±0.1	–	15.2±0.2	–	–
BB temp. (keV)	0.94±0.04	0.96±0.04	0.94±0.03	–	–
COMPMAG kT_{bb} (keV)	–	–	–	–	0.86±0.06
COMPMAG kT_e (keV)	–	–	–	–	4.45±0.12
COMPMAG τ	–	–	–	–	0.90±0.02
Column radius (km)	–	–	–	–	2.18±0.05
Iron line parameters					
Line energy (keV)	6.41±0.02	6.41±0.02	6.40±0.02	6.39±0.02	6.41±0.02
Eq. width (eV)	82±9	82±12	76±8	69±15	79±7
Component Flux (1-79 keV)[c]					
Power law flux	8.11±0.02	8.11±0.01	8.09±0.03	8.24±0.03	–
Blackbody flux	0.13±0.01	0.13±0.01	0.15±0.02	–	–
Source flux[c]					
Flux (1-10 keV)	1.46±0.02	1.47±0.01	1.47±0.01	1.46±0.01	1.47±0.02
Flux (10-79 keV)	6.78±0.01	6.77±0.02	6.78±0.01	6.79±0.01	6.80±0.02
Reduced χ^2 (*d.o.f*)	1.10 (1065)	1.10 (1066)	1.09 (1065)	1.11 (1064)	1.11 (1066)

[a] : Equivalent hydrogen column density in the source direction(in 10^{22} atoms cm^{-2} unit)
[b] : Additional hydrogen column density (in 10^{22} atoms cm^{-2} unit)
[c] : Unabsorbed flux in unit of 10^{-9} erg cm^{-2} s^{-1}.

direction (≈1.4×10^{22} cm^{-2}; Willingale et al. 2013). This indicated that the presence of an additional absorber close to the neutron star is unlikely. However, the spectral fitting with PC model leads to significantly higher additional column density of ≈168×10^{22} atoms cm^{-2}. Therefore, we consider the two-component model, i.e, CutoffPL and a thermal blackbody (CutoffPL+BB) to be the best-fit continuum models (see Figure 4.6).

4.3.2 Broad-band continuum modelling with physical models

As discussed in Chapter-1, the formation of accretion column above the magnetic poles of the accreting neutron star is mainly responsible to shape the characteristic spectrum of X-ray pulsars (Becker & Wolff, 2007b). The detection of the thermal blackbody component in the phase-averaged spectrum of 2S 1417-624 motivated us to explore the properties of accretion column through physically motivated models such as *BWmod* (Becker & Wolff, 2007b) and *COMPMAG* model (Farinelli et al., 2012).

The *BWmod* solves the radiative transfer equation (RTE) inside the accretion column analytically. The model assumes highly supersonic flow of fully ionized hydrogen falling onto the poles of neutron star via cylindrical accretion column. The infalling matter slowed down to subsonic velocities while interacting with the radiation dominated shock formed above the surface of neutron star. This is the major site for the reprocessing of X-ray photons, originating from the thermal mound of the neutron star surface. Due to the high optical depth along the axis of accretion column, most of the reprocessed photons escapes through the side walls of the column. The RTE equations incorportes three major sources of injecting *seed photons* i.e., blackbody, cylotron and bremsstrahlung processes (see Chapter-1, Section 1.5 for the detailed description about the origin of seed photons). Since the *BWmod* implementation accounts for the thermal as well as bulk comptonization processes, it is more suitable for fitting the spectrum of super-critical (bright) pulsars. A key approximation which allows *BWmod* to make RTE separable in energy and space, is the use of a specific velocity profile that is linearly dependent on optical depth of the accretion column (Becker & Wolff, 2007b). It is publicly available as a local model[3] in `XSPEC`. Due to the large uncertainty in the distance estimates for 2S 1417-624, we tried to use the *BWmod* by considering two different distance values i.e., 5 and 11 kpc. However, our attempts to use the *BWmod* to describe the pulsar spectrum failed as the reduced χ^2 value obtained from the fitting was >2 in each case. Therefore, it will not be discussed further.

COMPMAG is another phisically motivated model with a reasonable set of approxima-

tions. As compared to *BWmod*, it solves the RTE numerically by assuming a velocity profile which is characterized by an index η and a terminal velocity β. This velocity profile is the actual implementation of the true profiles calculated by Basko & Sunyaev (1976). The current publicly available version[4] of *COMPMAG* model uses only black-body *seed photons*, making it more suitable for the cases where the pulsar spectrum is dominated by comptonized black-body component i.e., like in the present study (see Table 4.2). While fitting this model in `XSPEC`, we assumed the velocity profile of the accretion column to be linearly dependent on the optical depth ($\beta(\tau) \propto \tau$, i.e. beta flag 2; Farinelli et al. 2012). This gives rise to an acceptable fit with reasonable values of spectral parameters (listed in Table 4.2). The other free parameters of the model are (i) the temperature of seed blackbody spectrum kT_{bb}, (ii) the electron plasma temperature kT_e and (iii) the vertical optical depth of the accretion column τ.

4.3.3 Pulse phase-resolved Spectroscopy

In order to investigate the cause of four peaks in the pulse profiles, the nature of thermal blackbody component and the variation of other spectral parameters during the 2018 giant outburst, we carried out pulse phase-resolved spectroscopy of 2S 1417-624 by using *NuSTAR* observation. The simultaneous *Swift*/XRT observation of the pulsar was not utilized for this purpose due to its low exposure time (1.8 ks, Table 4.1). Phase-resolved spectroscopy was performed by accumulating the source spectrum in 10 phase-bins by applying phase filters on the barycentric corrected event file in the `xselect` package. For phase-resolved spectral fitting, we used the same energy range as chosen for the phase averaged spectroscopy of the *NuSTAR* data i.e., 3.5-79 keV. Each individual phase-sliced spectra were fitted by using appropriate background, response and effective area files. We found that both the models i.e., cutoff+BB and HECut+BB along with the photoelectric absorption component and a Gaussian function at 6.4 keV, were able to describe the spectrum of individual phase bins and yielded a com-

[3]http://www.isdc.unige.ch/ ferrigno/images/Documents/BW_distribution/BW_cookbook.html
[4]https://heasarc.gsfc.nasa.gov/xanadu/xspec/models/compmag.html

parable values of fitted parameters. While fitting, the value of equivalent hydrogen column density was fixed at the phase averaged value (N_{H_1}; Table 4.2). The phase-resolved spectral parameters obtained from the fitting are shown in Figure 4.8 for the cutoff+BB model, along with the pulse profile of the pulsar at the top panel.

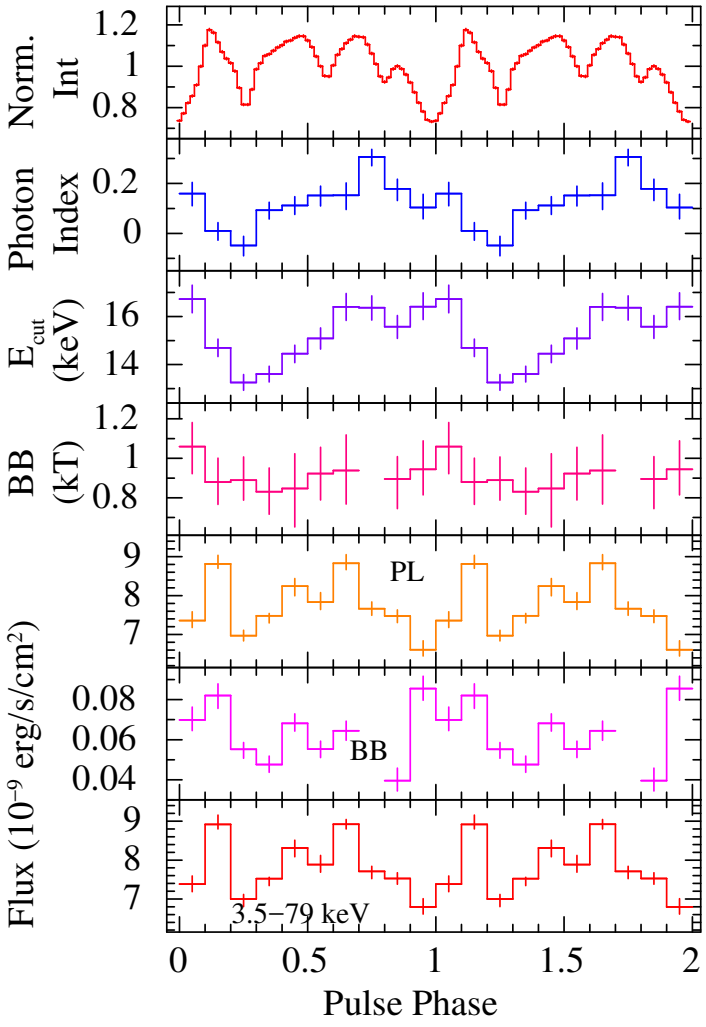

Figure 4.8: Spectral parameters obtained from the phase-resolved spectroscopy of 2S 1417-624 during *NuSTAR* observation in 2018 May by using cutoff+BB continuum model. Top panel shows the pulse profile of the pulsar in 3–79 keV energy range. The values of power-law photon index, cutoff energy (E_{cut}) and blackbody temperature are shown in the second, third and fourth panels from top, respectively. The power-law flux (PL), blackbody component flux (BB) and total flux in 3.5–79 keV range are presented in fifth, sixth and seventh panels, respectively. All fluxes are quoted in the units of 10^{-9} erg cm^{-2} s^{-1}. The errors in the spectral parameters are estimated at 90% confidence level.

Although the shape of the pulse profile of 2S 1417-624 during the *NuSTAR* observation was significantly different from those during previous outbursts in the *RXTE* era, the variation in the spectral parameters over the pulse phases were marginal. From Figure 4.8, it can be seen that the values of power-law photon index and cutoff energy were found to be variable in

range −0.1–0.3 and 13–17 keV, respectively. The blackbody component was detectable in all phase bins except for one (fourth panel of Figure 4.8), which indicates that the blackbody flux was either too low or not significant beyond 3 keV. The blackbody temperature was found to be almost constant (within errors) throughout the pulse phases. The power-law and best-fit model fluxes in 3.5-79 keV energy range, obtained from the fitting of data of individual phase bins, follow the shape of pulse profiles (fifth and seventh panels of Figure 4.8, respectively). Apart from the shape of total flux profiles over the pulse phase, an enhancement in the blackbody (BB) flux component can be clearly seen in 0.1–0.2, 0.4–0.5 and 0.9–1.0 phase ranges (sixth panel; Figure 4.8). This enhanced value of BB flux could be associated with the peculiar evolution of peaks in the energy resolved pulse profiles (Figure 4.3). All the flux values quoted in this Chapter are calculated by using the `cflux` convolution model. Other parameters such as iron line energy and its equivalent width were found to be consistent with the phase-averaged values and do not show any significant variation over the pulse phase.

4.4 Discussion

As seen in the previous Chapter, 2S 1417-624 shows strong luminosity dependent pulse profiles, i.e. switiching from two peaks to three peaks in the profile with the increase in luminosty. In the present study, we have witnessed a further evolution of pulse profile with the pulsar luminosity. The observations utilized in the present work, were performed at a flux level of approximately 350 mCrab (i.e. at the peak of the giant outburst) as recorded with the *Swift*/BAT (Nakajima et al., 2018). This provided us an opportunity to study the source properties at the highest observed luminosity till date. We took this opportunity to carry out a detailed timing and spectral analysis of 2S 1417-624 by using simultaneous *NuSTAR* and *Swift* observations. One of the most interesting aspect of the present study is the presence of four-peaks in the pulse profile. A more recent study with the *NICER* and *Insight-HXMT* shows a smooth and gradual evolution of the peaks in the pulse profiles of 2S 1417-624, from two to three and finally to four peaks with the increase in luminosity as the outburst

progressed (Ji et al., 2020). These results are in agreement with our findings during previous and current (2018 giant outburst) studies of the pulsar (Gupta et al. 2018, 2019).

As already pointed out in the previous Chapter, several other Be/X-ray binary pulsars are known to show energy dependent peaks and dips in their profiles during the outburst activities. These dip-like features in the pulse profiles have been widely associated with the presence of additional matter, which results in absorption/obscuration of the X-ray photons. Following these findings, we modelled the phase-resolved spectra of 2S 1417-624 with a partial covering cutoff power law model. As described in Section 4.3.1, we fixed the value of equivalent hydrogen column density (N_{H_1}) to the phase averaged value and left additional hydrogen column density (N_{H_2}) free to vary. We obtained an exceptionally high value of additional column density during the primary dip (0.95-1.05 pulse phase range: top panel of Figure 4.8). During other phases, there was no significant variation in the additional column density to draw any meaningful conclusion on this regard.

The broad-band spectrum of 2S 1417-624 has been successfully described with the standard continuum models such as cutoff power law and high energy cutoff power law models (İnam et al. 2004; Gupta et al. 2018 and references therein). However, in the present study, we found that these models are not suitable to describe the spectrum obtained at the peak of the 2018 giant X-ray outburst. Rather, it was found that a composite model consisting of a cutoff power law and blackbody component was required to describe the spectrum well. The *NuSTAR* observation presented here was carried out when the pulsar was brighter compared to the *RXTE* observations during the 2009 giant X-ray outburst. The additional blackbody component is, therefore, very likely due to the enhanced luminosity of the pulsar though the sensitivities of *NuSTAR* detectors at soft X-ray ranges are better than the *RXTE*/PCA.

Origin of soft X-ray excess emission

Several of the accretion powered X-ray binary pulsars (XBPs) have been observed to show an excess in the soft X-ray ranges. This is known as soft excess and has been modeled with

an additional thermal component in the pulsar spectrum. This soft excess is thought to be a very common intrinsic feature of XBPs. However, its detectability depends upon the source flux and column density (N_H) in the source direction (see Hickox et al. 2004 for a review). The possible mechanism behind the origin of this component could be : (i) emission from accretion column, (ii) thermal emission from collisionally energized diffuse gas around the neutron star, (iii) reprocessing of hard X-rays by diffuse cloud, and (iv) reprocessing of hard X-rays in optically thick accretion disk (Hickox et al., 2004). By using the value of blackbody normalization obtained from the phase-averaged spectral fitting and considering the source distance of 5 kpc, the radius of blackbody emitting region is estimated to be ≈2 km. In our study, the presence of hard Comptonized spectrum as well as an emitting radius of ≈2 km makes it difficult to consider accretion column as a primary source of soft excess emission. The non-pulsating nature of blackbody component also suggests the same. Alternatively, it is possible that the neutron star surface is contributing for reflection of X-ray photons from the column. This may explain the presence of non-pulsating thermal emission from the pulsar. A similar analogy has also been suggested by Poutanen et al. (2013) on cyclotron line scattering feature.

4.5 Summary and Conclusion

In the present study, we have witnessed a change in spectral continuum at higher luminosity. By considering a distance of 5 kpc and 11 kpc, the source luminosity in 1-79 keV range was estimated to be $\approx 2.46\times10^{37}$ erg s^{-1} and 1.19×10^{38} erg s^{-1}, respectively. This luminosity ($\sim10^{37}$ erg s^{-1}) is crucial in understanding the accretion state transitions in X-ray binary pulsars and is known as critical luminosity (Becker et al., 2012). At such high luminosities, the radiation dominated shocks may form near the neutron star surface, giving rise to dramatical changes in pulsar beam configuration and spectral parameters (see Reig & Nespoli 2013; Epili et al. 2017). Thus, the spectral changes seen in the present study could be associated with the critical luminosity of the source. Similar results were found during the previous giant outburst

in 2009 when the pulsed fraction of the pulsar was anti-correlated with the source flux in a luminous regime (Gupta et al., 2018). However, recently Ji et al. (2020) have provided an alternative explanation for this peculiar transition in the pulse profiles of 2S 1417-624, to be due to the transition of the accretion disc from gas-dominated to radiation pressure-dominated state (theoretically predicted by Shakura & Sunyaev 1973). This kind of transition have been reported previously for a ULXP source Swift J0243.6+6124 by Doroshenko et al. (2020).

It is also important to note that a positive correlation was detected between the pulsed fraction and flux below 1.2×10^{-9} erg cm^{-2} s^{-1} (see, Figure 2 of İnam et al. 2004). Above this limit, we detected a clear anti-correlation in the present study. The observed anti-correlation can be attributed to the increase in unpulsed component from the pulsar in the form of fan beam emission close to the critical luminosity. The timing analysis, in the present study (Figure 4.4) also supports this idea in context of earlier finding by Gupta et al. (2018).

Chapter 5

Concluding Remarks and Future prospects

In the present thesis, the effects of change in mass accretion rate on the spectral and temporal properties of accretion powered Be/X-ray binary pulsars have been explolerd. As the Be/X-ray binary pulsars show a large variation in the X-ray luminosity (from quiescence to the peak of X-ray outbursts), these HMXB pulsars provide better opportunity to carry out luminosity dependent studies. For this study, the Be/X-ray binary pulsar 2S 1417-627 was chosen as it was observed extensively with several X-ray observatories during its quiescent phase and at different luminosity levels during X-ray outbursts. The summary of our investigations are presented below. After the summary, the chapter will be concluded with the ongoing and future projects emerging from the present study.

5.1 Summary

To carry out the luminosity dependence of temporal and spectral properties of accretion powered X-ray pulsars, the Be/X-ray binary pulsar 2S 1417-627 was chosen as it was observed with several observatories at a wide range of luminosities. The results obtained from such studies are summarized here.

- As mentioned previously, the critical luminosity marks the transition luminosity at which the radiation dominated shock is expected to form in the accretion column of the pulsar. A sharp transition in the spectral and temporal properties of the pulsar, is expected at this luminosity regime. In Chapter-3, we presented a comprehensive study of the Be/X-ray binay pulsar 2S 1417-624 during its 2009 giant outburst as observed with *RXTE* observatory. The pulsar was observed with *RXTE* at various pointings covering the rising as well as declining phases of the outburst, thereby giving us an opportunity to study the accretion mechanism at various luminosity levels. We observed a smooth transition in the shape of the pulse profiles of the pulsar from two-peak to three-peak morphology during the outburst rise. However, a reverse trend i.e., three-peaked profile to two-peaked profile, was observed during the outburst decline. This kind of variation had never been seen in this pulsar. At the same time, an anti-correlation between the pulse fraction and the pulsar flux was observed though a positive correlation is generally expected.

  The broadband spectrum of the pulsar was modeled with a power law modified with high-energy cut-off model along with a Gaussian function for the iron fluorescence emission line at 6.4 keV. The associated spectral parameters also showed an intriguing variation with the source luminosity, which together with the timing studies, points toward the change in accretion regime of the pulsar from sub-critical to super-critical luminosity levels. Using the value of observed critical luminosity (i.e. luminosity corresponding to the transition between pulse profile morphology), we determined the strength of the pulsar magnetic field by the following equation:

$$L_{\rm crit} \;=\; 1.49 \times 10^{37} \left(\frac{B}{10^{12}\,{\rm G}}\right)^{16/15} {\rm erg\,s^{-1}} \tag{5.1}$$

  The critical luminosity was estimated to be $3.52\times\ 10^{37}$ erg s^{-1} (i.e. corresponding to the flux level 2.94×10^{-9} erg s^{-1} cm^{-2}, where transition from two- to three- peaks start to occur). By using this value in Equation 5.1, the value of magnetic field strength was

derived to be $\sim$2.24 $\times$ 10^{12} G. Recently, 2S 1417-624 showed another strong giant X-ray outburst in 2018. Ji et al. (2020) have reported the timing studies of 2018 giant outburst with *Insight*/HXMT, *NICER*/XTI and *Fermi*/GBM instruments and calculated the magnetic field strength to be $\sim$ 7$\times$ 10^{12} G (based upon wide phenomenology). We note that our estimate of magnetic field strength is marginally off compared to that reported by Ji et al. (2020). A possible explanation behind this discrepancy could be due to the fact that Ji et al. (2020) estimated the strength of magnetic field by implementing the accretion driven torque model which requires the distance of the source to be $\sim$20 kpc. However, we have assumed a source distance of 10 kpc while estimating the magnetic field strength. Although, there is a huge uncertainty in the source distance estimates, recent *Gaia* measurements constrain the source distance to be $\sim$10 kpc.

- In Chapter-4, we studied the spectral and timing behavior of 2S 1417-624 at the peak of the giant X-ray outburst in 2018, using simultaneous observations with the *NuSTAR* and *Swift* observatories. This outburst was more luminous as compared to the previous giant outburst in 2009, thus offering the opportunity to study the source properties at even higher luminosities. We observed further evolution of pulse profiles with luminosity, i.e. to four peaks during this observation. This result is consistent with the timing studies reported by Ji et al. (2020). The broadband spectrum of the pulsar was described with a composite model, i.e., a cut-off power law (modified with the interstellar absorption), a Gaussian function for the iron fluorescence emission line at 6.4 keV and a thermal blackbody component with a temperature of $\approx$1 keV. The presence of blackbody emission in the energy spectrum of the pulsar motivated us to carry out a detailed physical modeling of the spectral continuum using recently developed physical models such as COMPMAG and BW models. We found that the COMPMAG model could describe the energy spectrum of 2S 1417-624 well. This model has several free parameters such as temperature of seed blackbody photons (kT_{bb}), electron plasma temperature (kT_e), vertical optical depth of the accretion column (τ) etc. By implementing this model, we

were able to derive the physical parameters of the accretion column. We found that the optical depth of the accretion column was marginally higher (i.e., $\tau \approx 1$; see Table-4.2 of Chapter-4). This is an important result as it could be interpreted as an observational evidence for the formation of optically thick accretion column, i.e. super-critical regime. However, we would like to emphasize that these models are relatively new and still under development. Hence, further studies are required to prove their robustness. Therefore, it is important to implement these models on a large sample of sources to give inputs to the theory of pulsar accretion. Further improvements are required in this direction to develop a self consistent physical models for the pulsar spectrum. Also, the modeling of pulse profiles (including general relativistic considerations and light bending effects) would be required to understand the complex physical processes happening in the vicinity of the pulsars, which is an extremely complicated task and outside the scope of this work.

5.2 Future prospects

Be/X-ray binary pulsars during quiescence

This thesis demonstrates that the emission characteristics of accretion powered Be/X-ray binary pulsars strongly depend upon the mass accretion rate (and hence on luminosity). We have systematically studied the impact of increasing mass accretion rate on the spectral and temporal properties of the Be/X-ray binary pulsar 2S 1417-624. However, at present we have very little knowledge about the emission characteristics of the pulsar during very low mass accretion rates (i.e. during quiescent phase). Therefore, in future we would like to study very low luminosity regimes of accretion powered Be/X-ray binary pulsars. As discussed in Section 1.4 of Chapter-1, it is commonly believed that during quiescence, the X-ray pulsars transit to propeller regime and show no X-ray activity at all. At such low luminosities, the spin period of the neutron star plays a dominant role in determining how the accretion

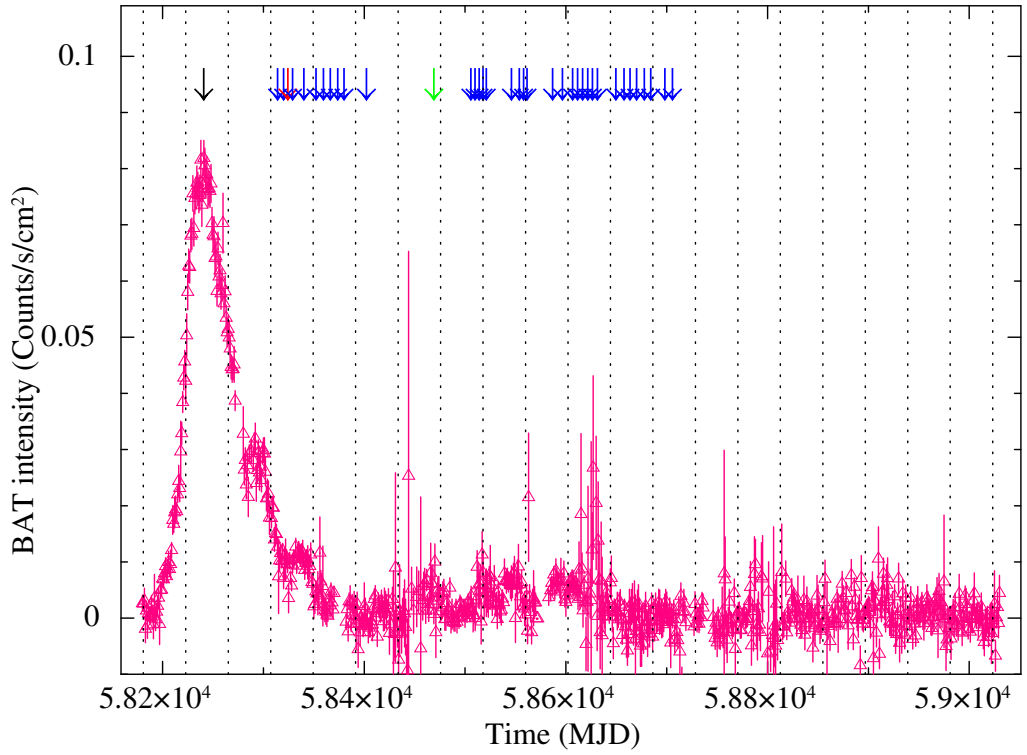

Figure 5.1: Monitoring light curve of 2S 1417-624 during the decline of 2018 giant outburst, as observed with *Swift*/BAT in 15-50 keV energy range. The vertical arrow-marks on the top of the light curve indicate the pointed observations made with the *Swift*/XRT. The vertical dotted lines indicate the expected times of periastron passage of the pulsar.

proceeds. For slow rotating neutron stars, matter may still be able to leak through the magnetoshphere, thereby leading to pulsed emission (Rouco Escorial et al. 2017; Tsygankov et al. 2017). However, for rapidly spinning magnetized neutron star, the accreted material is expected to get expelled rather than being accreted (Illarionov & Sunyaev 1975; Romanova et al. 2004; D'Angelo & Spruit 2010). The detection of pulsed emission at very low luminoities is still an open question. Several theories are proposed to explain the detection of pulsations at extremely low luminosities such as, cooling of accretion heated surface of the neutron star and low-level accretion on the magnetic poles by the leakage of matter through the magnetic barrier (see Rouco Escorial et al. 2017 and references therein). Therefore, the study of these sources at low luminosity regimes would help us to obtain a better understanding about the magnetospheric interactions. Moreover, with the improved sensitivity of X-ray detectors, it has now become possible to observe these sources at extremely low luminosities.

Recent studies indicate that a few pulsars show pulsed emission even at extremely low mass accretion rates, which contradicts our understanding (Tsygankov et al., 2017). In their

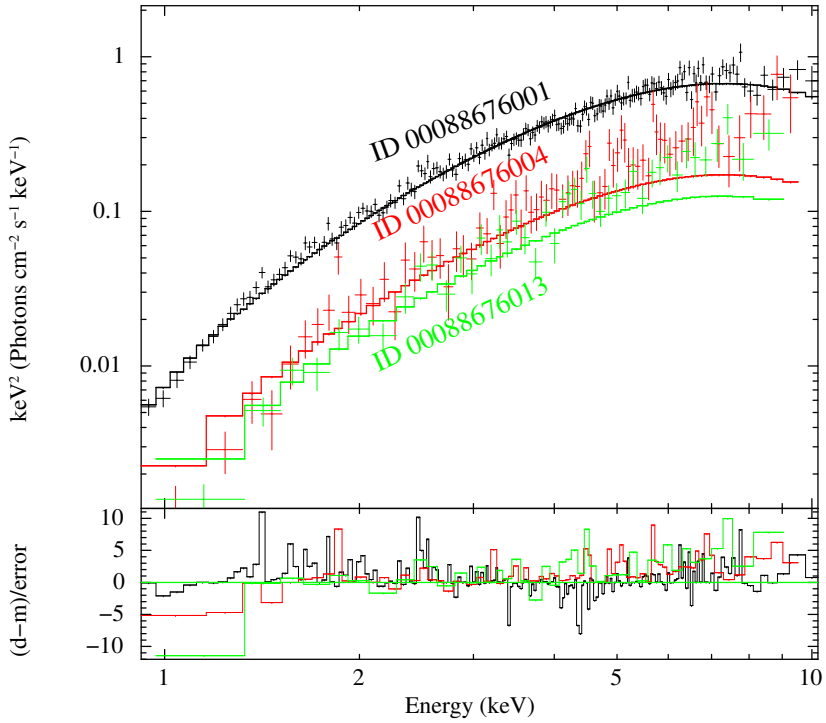

Figure 5.2: Spectral fitting for three different observations selected at different luminosity levels. The spectrum (plotted in black color) indicated the highest luminosity level at the outburst peak, the energy spectrum in red indicates one of the observation taken during the declining phase and the green points indicate the observation taken during the quiescence state (see text for the detailed description).

study, Tsygankov et al. (2017) found that for certain combination of spin period and magnetic field strength, a few pulsars could show pulsed emission during quiescence states. Moreover, the broadband spectrum of accretion powered pulsars at low luminosity are found to be well characterized by two component comptonization model (see Doroshenko et al. 2012; Tsygankov et al. 2019), as opposed to cut-off power law model fitted during high luminosities. Motivated from these studies, we would like to carry out a detailed investigation of a few Be/X-ray binary pulsars during quiescence regime. In particular, we would like to carry out a detailed investigation of 2S 1417-624 and EXO 2030+375 during their quiescent phases. We have selected EXO 2030+375 for this study as this pulsar regularly shows Type-I X-ray outbursts at its periastron passage and has been observed many times. We have started our study on 2S 1417-624 by using observations carried out with the *Swift*/XRT instrument, covering the 2018 giant outburst decline and then its transition to the quiescent luminosities (see Figure 5.1).

The vertical arrow-marks on the *Swift*/BAT monitoring light curve indicate the epochs

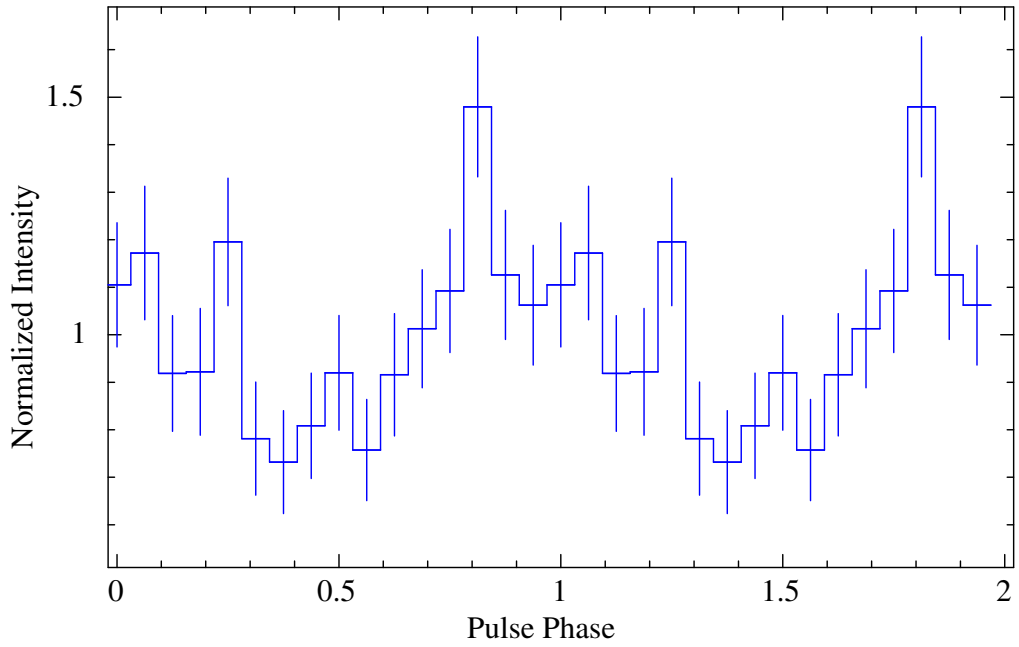

Figure 5.3: Pulse profile of 2S 1417-624 during its quiescent phase (corresponding to the observation indicated with green arrow in Figure 5.1). Two pulses are shown for clarity.

of XRT pointed observations (each with roughly ∼1 ks exposure) taken during the declining phase of 2018 giant outburst. In particular, we have selected three observations with longest exposure times (∼1.9 ks each) across different luminosities, i.e. one at the outburst peak (ID 00088676001; indicated with black arrow in Figure 5.1), one during the outburst decline (ID 00088676004; indicated with red arrow in Figure 5.1) and one during the quiescence state (ID 00088676013; indicated with green arrow in Figure 5.1). We carried out a preliminary spectral analysis of these three observations. We found that the quiescence spectrum can be well described with an absorbed power law model. However, spectral variations are not seen among these observations (see Figure 5.2). A detailed spectral analysis for all the epochs of the observations is ongoing and in future, we further plan to compliment these observations with additional *NICER* observations taken at various luminosity levels.

Apart from the spectral studies, we have carried out a detailed timing analysis of the individual *Swift*/XRT observations. Our preliminary analysis indicates that 2S 1417-624 showed pulsed emission during its quiescence state (as indicated with green arrow in Figure 5.1). We were successfully able to detect pulsation at 17.41(8) s in the quiescent light curve of 2S 1417-624. We further folded the light curve at the estimated spin period and generated

the corresponding pulse profile during the quiescence (see Figure 5.3). Upto the best of our knowledge, this is the first report on the detection of pulsation in the quiescent phase of 2S 1417-624. This gives us confidence to investigate this source further through a detailed spectral and timing studies with multiple instruments (with *Swift*/XRT, *NICER*/XTI and *ASTROSAT*/LAXPC) during this event. We are planning to propose a deep *ASTROSAT* observation of this source during its quiescence state to strengthen our results.

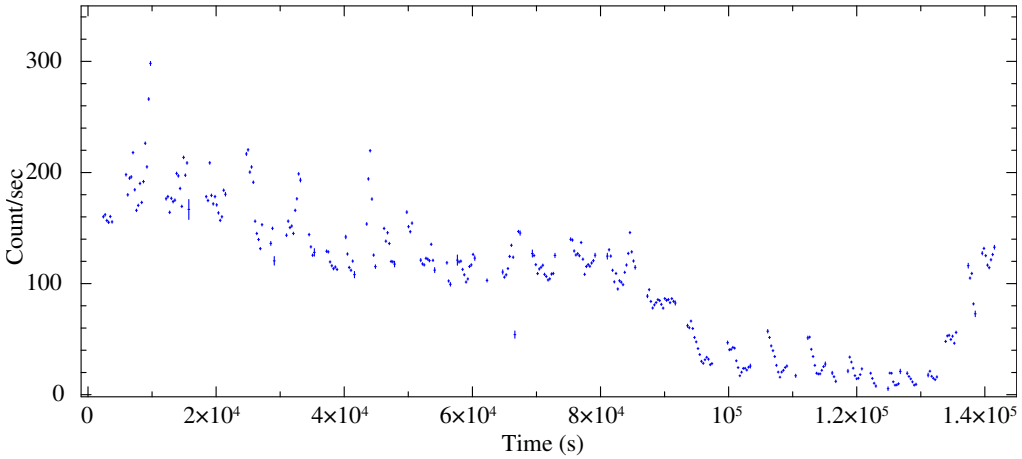

Figure 5.4: Light curve of SG-HMXB pulsar Cen X-3 as observed with *ASTROSAT*/LAXPC-20. The source has been observed during late orbital phases of the pulsar and a clear dipping activity is visible in the light curve.

A systematic analysis of Be/X-ray binary pulsars during quiescent phases, is one of the natural project emerging from our studies. Therefore, we propose to investigate the quiescence state of other Be/X-ray binary pulsars in future. For that purpose, we would like to select those sources which show regular Type-I outbursts during their periastron passage. One such source which shows regular outburst activity is EXO 2030+375 (Epili et al., 2017). This would allow us to systematically plan and propose for observations i.e., once the pulsar enters the quiescence state (after the decline of Type-I outburst). Other Be/XRB sources, showing regular Type-I outburst activities are 2S 1835-024 (Finger et al., 1999) and GRO J1008-57 (Coe et al., 2007).

Properties of other HMXB pulsars at different luminosities

We would also like to perform a detailed study on a well known disk-fed super-giant high mass X-ray binary (SG-HMXB) pulsar Cen X-3. We have observed this source with *ASTROSAT* for an effective exposure of ∼80 ks during its late orbital phase (see Figure 5.4). Cen X-3 shows peculiar dipping activity at different orbital phases, which is speculated to be associated with the formation of accretion wake in the presence of stellar winds emanating from its super-giant companion star. Apart from Cen X-3, only four other HMXB pulsars. i.e., 4U 1700-37, Vela X-1, 4U 1907+09 and GX 301-2 show such kind of dipping activity in their X-ray light curves. Although Cen X-3 is among one of the first detected pulsars in our Galaxy and have been studied extensively since then, the orbital dependence of its dipping activity have not been explored yet. Therefore, we would like to undertake this study with highly sensitive instruments onboard *ASTROSAT*, which will eventually help us to develop an understanding about the formation of structured wind found in these HMXB systems.

Bibliography

Alpar, M. A. & Shaham, J. 1985, Is GX5 - 1 a millisecond pulsar?, Nature, 316, 239

Apparao, K. M. V., Naranan, S., Kelley, R. L., & Bradt, H. V. 1980, 2S 1417-624 : a variable galactic X-ray source near CG 312-1., A&A, 89, 249

Arnaud, K. A. 1996, in Astronomical Society of the Pacific Conference Series, Vol. 101, Astronomical Data Analysis Software and Systems V, ed. G. H. Jacoby & J. Barnes, 17

Baade, W. & Zwicky, F. 1934, Cosmic Rays from Super-novae, Proceedings of the National Academy of Science, 20, 259

Barthelmy, S. D., Barbier, L. M., Cummings, J. R., et al. 2005, The Burst Alert Telescope (BAT) on the SWIFT Midex Mission, Space Sci. Rev., 120, 143

Basko, M. M. & Sunyaev, R. A. 1975, Radiative transfer in a strong magnetic field and accreting X-ray pulsars., A&A, 42, 311

Basko, M. M. & Sunyaev, R. A. 1976, The limiting luminosity of accreting neutron stars with magnetic fields., MNRAS, 175, 395

Becker, P. A., Klochkov, D., Schönherr, G., et al. 2012, Spectral formation in accreting X-ray pulsars: bimodal variation of the cyclotron energy with luminosity, A&A, 544, A123

Becker, P. A. & Wolff, M. T. 2005, Spectral Formation in X-Ray Pulsar Accretion Columns, ApJ, 621, L45

Becker, P. A. & Wolff, M. T. 2007a, Thermal and Bulk Comptonization in Accretion-powered X-Ray Pulsars, ApJ, 654, 435

Becker, P. A. & Wolff, M. T. 2007b, Thermal and Bulk Comptonization in Accretion-powered X-Ray Pulsars, ApJ, 654, 435

Bellm, E. C., Fürst, F., Pottschmidt, K., et al. 2014, Confirmation of a High Magnetic Field in GRO J1008-57, ApJ, 792, 108

Bhattacharya, D. 1995, The Evolution of the Magnetic Fields of Neutron Stars, Journal of Astrophysics and Astronomy, 16, 217

Bildsten, L., Chakrabarty, D., Chiu, J., et al. 1997, Observations of Accreting Pulsars, ApJS, 113, 367

Blaauw, A. 1961, On the origin of the O- and B-type stars with high velocities (the "run-away" stars), and some related problems, Bull. Astron. Inst. Netherlands, 15, 265

Blondin, J. M., Kallman, T. R., Fryxell, B. A., & Taam, R. E. 1990, Hydrodynamic Simulations of Stellar Wind Disruption by a Compact X-Ray Source, ApJ, 356, 591

Blondin, J. M., Stevens, I. R., & Kallman, T. R. 1991, Enhanced Winds and Tidal Streams in Massive X-Ray Binaries, ApJ, 371, 684

Boldin, P. A., Tsygankov, S. S., & Lutovinov, A. A. 2013, On timing and spectral characteristics of the X-ray pulsar 4U 0115+63: Evolution of the pulsation period and the cyclotron line energy, Astronomy Letters, 39, 375

Bondi, H. & Hoyle, F. 1944, On the mechanism of accretion by stars, MNRAS, 104, 273

Burderi, L., Di Salvo, T., Robba, N. R., La Barbera, A., & Guainazzi, M. 2000, The 0.1-100 KEV Spectrum of Centaurus X-3: Pulse Phase Spectroscopy of the Cyclotron Line and Magnetic Field Structure, ApJ, 530, 429

Burrows, D. N., Hill, J. E., Nousek, J. A., et al. 2005, The Swift X-Ray Telescope, Space Sci. Rev., 120, 165

Casares, J., Negueruela, I., Ribó, M., et al. 2014, A Be-type star with a black-hole companion, Nature, 505, 378

Chaty, S., Fortin, F., García, F., & Fogantini, F. 2019, The dark side of supergiant High-Mass X-ray Binaries, arXiv e-prints, arXiv:1901.03593

Coe, M. J. 2000, in Astronomical Society of the Pacific Conference Series, Vol. 214, IAU Colloq. 175: The Be Phenomenon in Early-Type Stars, ed. M. A. Smith, H. F. Henrichs, & J. Fabregat, 656

Coe, M. J., Bird, A. J., Hill, A. B., et al. 2007, Now you see it, now you don't - the circumstellar disc in the GRO J1008-57 system, MNRAS, 378, 1427

Coe, M. J. & Kirk, J. 2015, Catalogue of Be/X-ray binary systems in the Small Magellanic Cloud: X-ray, optical and IR properties, MNRAS, 452, 969

Corbet, R. H. D. 1986, The three types of high-mass X-ray pulsator., MNRAS, 220, 1047

Currie, M. J., Berry, D. S., Jenness, T., et al. 2014, in Astronomical Society of the Pacific Conference Series, Vol. 485, Astronomical Data Analysis Software and Systems XXIII, ed. N. Manset & P. Forshay, 391

D'Angelo, C. R. & Spruit, H. C. 2010, Episodic accretion on to strongly magnetic stars, MNRAS, 406, 1208

Davidson, K. & Ostriker, J. P. 1973, Neutron-Star Accretion in a Stellar Wind: Model for a Pulsed X-Ray Source, ApJ, 179, 585

Doroshenko, V., Santangelo, A., Kreykenbohm, I., & Doroshenko, R. 2012, The hard X-ray emission of X Persei, A&A, 540, L1

Doroshenko, V., Zhang, S. N., Santangelo, A., et al. 2020, Hot disc of the Swift J0243.6+6124 revealed by Insight-HXMT, MNRAS, 491, 1857

Dugair, M. R., Jaisawal, G. K., Naik, S., & Jaaffrey, S. N. A. 2013, Detection of a variable QPO at ∼41 mHz in the Be/X-ray transient pulsar 4U 0115+634, MNRAS, 434, 2458

Epili, P., Naik, S., Jaisawal, G. K., & Gupta, S. 2017, Decade long RXTE monitoring observations of Be/X-ray binary pulsar EXO 2030+375, MNRAS, 472, 3455

Esposito, P., Israel, G. L., Milisavljevic, D., et al. 2015, Periodic signals from the Circinus region: two new cataclysmic variables and the ultraluminous X-ray source candidate GC X-1, MNRAS, 452, 1112

Farinelli, R., Ceccobello, C., Romano, P., & Titarchuk, L. 2012, Numerical solution of the radiative transfer equation: X-ray spectral formation from cylindrical accretion onto a magnetized neutron star, A&A, 538, A67

Finger, M. H., Bildsten, L., Chakrabarty, D., et al. 1999, The Outbursts and Orbit of the Accreting Pulsar GS 1843-02 = 2S 1845-024, ApJ, 517, 449

Finger, M. H., Wilson, R. B., & Chakrabarty, D. 1996, Reappearance of the X-ray binary pulsar 2S 1417-624., A&AS, 120, 209

Forman, W., Jones, C., Cominsky, L., et al. 1978, The fourth Uhuru catalog of X-ray sources., ApJS, 38, 357

Frank, J., King, A., & Raine, D. J. 2002, Accretion Power in Astrophysics: Third Edition

Friedman, H., Lichtman, S. W., & Byram, E. T. 1951, Photon Counter Measurements of Solar X-Rays and Extreme Ultraviolet Light, Physical Review, 83, 1025

Fürst, F., Kreykenbohm, I., Pottschmidt, K., et al. 2010, X-ray variation statistics and wind clumping in Vela X-1, A&A, 519, A37

Gehrels, N., Chincarini, G., Giommi, P., et al. 2004, The Swift Gamma-Ray Burst Mission, ApJ, 611, 1005

Ghosh, P. & Lamb, F. K. 1978, Disk accretion by magnetic neutron stars., ApJ, 223, L83

Ghosh, P. & Lamb, F. K. 1979, Accretion by rotating magnetic neutron stars. III. Accretion torques and period changes in pulsating X-ray sources., ApJ, 234, 296

Giacconi, R., Gursky, H., Kellogg, E., Schreier, E., & Tananbaum, H. 1971, Discovery of Periodic X-Ray Pulsations in Centaurus X-3 from UHURU, ApJ, 167, L67

Giacconi, R., Gursky, H., Paolini, F. R., & Rossi, B. B. 1962, Evidence for x Rays From Sources Outside the Solar System, Phys. Rev. Lett., 9, 439

Grindlay, J. E., Petro, L. D., & McClintock, J. E. 1984, Optical identification of 2S 1417-62., ApJ, 276, 621

Gupta, S., Naik, S., & Jaisawal, G. K. 2019, NuSTAR view of Be/X-ray binary pulsar 2S 1417-624 during 2018 giant outburst, MNRAS, 490, 2458

Gupta, S., Naik, S., Jaisawal, G. K., & Epili, P. R. 2018, Spectral and timing studies of 2S 1417-624 during a giant outburst, MNRAS, 479, 5612

Haardt, F. & Maraschi, L. 1991, A Two-Phase Model for the X-Ray Emission from Seyfert Galaxies, ApJ, 380, L51

Harding, A. K., Meszaros, P., Kirk, J. G., & Galloway, D. J. 1984, Self-consistent models for Coulomb-heated X-ray pulsar atmospheres., ApJ, 278, 369

Harrison, F. A., Craig, W. W., Christensen, F. E., et al. 2013, The Nuclear Spectroscopic Telescope Array (NuSTAR) High-energy X-Ray Mission, ApJ, 770, 103

Henrichs, H. F. & van den Heuvel, E. P. J. 1983, Is the millisecond pulsar formed from coalescence of a close neutron-star binary?, Nature, 303, 213

Hewish, A., Bell, S. J., Pilkington, J. D. H., Scott, P. F., & Collins, R. A. 1968, Observation of a Rapidly Pulsating Radio Source, Nature, 217, 709

Hickox, R. C., Narayan, R., & Kallman, T. R. 2004, Origin of the Soft Excess in X-Ray Pulsars, ApJ, 614, 881

Hill, J. E., Burrows, D. N., Nousek, J. A., et al. 2004, in Society of Photo-Optical Instrumentation Engineers (SPIE) Conference Series, Vol. 5165, Proc. SPIE, ed. K. A. Flanagan & O. H. W. Siegmund, 217–231

Horne, J. H. & Baliunas, S. L. 1986, A Prescription for Period Analysis of Unevenly Sampled Time Series, ApJ, 302, 757

Illarionov, A. F. & Sunyaev, R. A. 1975, Why the Number of Galactic X-ray Stars Is so Small?, A&A, 39, 185

İnam, S. Ç., Baykal, A., Matthew Scott, D., Finger, M., & Swank, J. 2004, X-ray flux related timing and spectral features of 2S 1417-62, MNRAS, 349, 173

Islam, N. & Paul, B. 2014, Orbital phase resolved spectroscopy of GX 301-2 with MAXI, MNRAS, 441, 2539

Jahoda, K., Markwardt, C. B., Radeva, Y., et al. 2006, Calibration of the Rossi X-Ray Timing Explorer Proportional Counter Array, ApJS, 163, 401

Jahoda, K., Swank, J. H., Giles, A. B., et al. 1996, in Society of Photo-Optical Instrumentation Engineers (SPIE) Conference Series, Vol. 2808, Proc. SPIE, ed. O. H. Siegmund & M. A. Gummin, 59–70

Jaisawal, G. K. & Naik, S. 2014, Investigation of iron emission lines in the eclipsing high mass X-ray binary pulsar OAO˜1657-415, Bulletin of the Astronomical Society of India, 42, 147

Jaisawal, G. K. & Naik, S. 2015, Broad-band spectroscopy of the eclipsing high-mass X-ray binary 4U 1700-37 with Suzaku, MNRAS, 448, 620

Jaisawal, G. K. & Naik, S. 2017, in 7 years of MAXI: monitoring X-ray Transients, ed. M. Serino, M. Shidatsu, W. Iwakiri, & T. Mihara, 153

Jaisawal, G. K., Naik, S., & Epili, P. 2016, Suzaku view of the Be/X-ray binary pulsar GX 304-1 during Type I X-ray outbursts, MNRAS, 457, 2749

Ji, L., Doroshenko, V., Santangelo, A., et al. 2020, Timing analysis of 2S 1417-624 observed with NICER and Insight-HXMT, MNRAS, 491, 1851

Kaaret, P., Feng, H., & Roberts, T. P. 2017, Ultraluminous X-Ray Sources, ARA&A, 55, 303

Kelley, R. L., Apparao, K. M. V., Doxsey, R. E., et al. 1981, Discovery of X-ray pulsations from 2S 1417-624., ApJ, 243, 251

Kraus, U., Blum, S., Schulte, J., Ruder, H., & Meszaros, P. 1996, Analyzing X-Ray Pulsar Profiles: Geometry and Beam Pattern of Centaurus X-3, ApJ, 467, 794

Kraus, U., Zahn, C., Weth, C., & Ruder, H. 2003, X-Ray Pulses from Accretion Columns: Contributions to the Energy Dependence of the Pulse Shape, ApJ, 590, 424

Kreykenbohm, I., Wilms, J., Kretschmar, P., et al. 2008, High variability in Vela X-1: giant flares and off states, A&A, 492, 511

Krimm, H. A., Barthelmy, S. D., Baumgartner, W., et al. 2009, Swift/BAT confirms the outburst from 2S 1417-624, The Astronomer's Telegram, 2276, 1

Krimm, H. A., Barthelmy, S. D., Cummings, J. R., et al. 2018, Swift/BAT confirms the giant outburst of H 1417-624, The Astronomer's Telegram, 11569, 1

Krimm, H. A., Holland, S. T., Corbet, R. H. D., et al. 2013, The Swift/BAT Hard X-Ray Transient Monitor, ApJS, 209, 14

Kühnel, M., Fürst, F., Pottschmidt, K., et al. 2017, Evidence for different accretion regimes in GRO J1008-57, A&A, 607, A88

Lai, D. 2001, Matter in strong magnetic fields, Reviews of Modern Physics, 73, 629

Lamb, F. K., Pethick, C. J., & Pines, D. 1973, A Model for Compact X-Ray Sources: Accretion by Rotating Magnetic Stars, ApJ, 184, 271

Langer, S. H. & Rappaport, S. 1982, Low-luminosity accretion onto magnetized neutron stars, ApJ, 257, 733

Lattimer, J. M. 2007, Equation of state constraints from neutron stars, Ap&SS, 308, 371

Leahy, D. A. 1987, Searches for pulsed emission - Improved determination of period and amplitude from epoch folding for sinusoidal signals, A&A, 180, 275

Leahy, D. A., Elsner, R. F., & Weisskopf, M. C. 1983, On searches for periodic pulsed emission - The Rayleigh test compared to epoch folding, ApJ, 272, 256

Levine, A. M., Bradt, H., Cui, W., et al. 1996, First Results from the All-Sky Monitor on the Rossi X-Ray Timing Explorer, ApJ, 469, L33

Lewin, W. H. G., van Paradijs, J., & Taam, R. E. 1993, X-Ray Bursts, Space Sci. Rev., 62, 223

Lewin, W. H. G., van Paradijs, J., & van den Heuvel, E. P. J. 1995, X-ray binaries., Cambridge Astrophysics Series, 26

Lewin, W. H. G., van Paradijs, J., & van den Heuvel, E. P. J. 1997, X-ray binaries., Cambridge Astrophysics Series, 26

Liu, Q. Z., van Paradijs, J., & van den Heuvel, E. P. J. 2006, Catalogue of high-mass X-ray binaries in the Galaxy (4th edition), A&A, 455, 1165

Liu, Q. Z., van Paradijs, J., & van den Heuvel, E. P. J. 2007, A catalogue of low-mass X-ray binaries in the Galaxy, LMC, and SMC (Fourth edition), A&A, 469, 807

Lomb, N. R. 1976, Least-Squares Frequency Analysis of Unequally Spaced Data, Ap&SS, 39, 447

Lutovinov, A. A. & Tsygankov, S. S. 2009, Timing characteristics of the hard X-ray emission from bright X-ray pulsars based on INTEGRAL data, Astronomy Letters, 35, 433

Makishima, K., Mihara, T., Ishida, M., et al. 1990, Discovery of a Prominent Cyclotron Absorption Feature from the Transient X-Ray Pulsar X0331+53, ApJ, 365, L59

Makishima, K., Mihara, T., Nagase, F., & Tanaka, Y. 1999, Cyclotron Resonance Effects in Two Binary X-Ray Pulsars and the Evolution of Neutron Star Magnetic Fields, ApJ, 525, 978

Manousakis, A., Walter, R., & Blondin, J. M. 2012, Neutron star masses from hydrodynamical effects in obscured supergiant high mass X-ray binaries, A&A, 547, A20

Markert, T. H., Winkler, P. F., Laird, F. N., et al. 1979, The MIT/OSO 7 catalog of X-ray sources: intensities, spectra, and long-term variability., ApJS, 39, 573

Meszaros, P. & Nagel, W. 1985a, X-ray pulsar models. I. Angle-dependent cyclotron line formation and comptonization., ApJ, 298, 147

Meszaros, P. & Nagel, W. 1985b, X-ray pulsar models. II. Comptonized spectra and pulse shapes., ApJ, 299, 138

Mihara, T. 1995, PhD thesis, -

Moretti, A., Campana, S., Mineo, T., et al. 2005, in Society of Photo-Optical Instrumentation Engineers (SPIE) Conference Series, Vol. 5898, Proc. SPIE, ed. O. H. W. Siegmund, 360–368

Mushtukov, A. A., Suleimanov, V. F., Tsygankov, S. S., & Poutanen, J. 2015, The critical accretion luminosity for magnetized neutron stars, MNRAS, 447, 1847

Mushtukov, A. A., Verhagen, P. A., Tsygankov, S. S., et al. 2018, On the radiation beaming of bright X-ray pulsars and constraints on neutron star mass-radius relation, MNRAS, 474, 5425

Nagase, F. 1989, Accretion-powered X-ray pulsars., PASJ, 41, 1

Nagel, W. 1981a, Radiative Transfer in a Strongly Magnetized Plasma - Part Two - Effects of Comptonization, ApJ, 251, 288

Nagel, W. 1981b, Radiative transfer in a strongly magnetized plasma. I - Effects of anisotropy. II - Effects of Comptonization, ApJ, 251, 278

Naik, S., Dotani, T., Terada, Y., et al. 2008, Broadband X-Ray Spectroscopy of A0535+262 with Suzaku, ApJ, 672, 516

Naik, S. & Jaisawal, G. K. 2015, Suzaku observation of Be/X-ray binary pulsar EXO 2030+375, Research in Astronomy and Astrophysics, 15, 537

Naik, S., Maitra, C., Jaisawal, G. K., & Paul, B. 2013, Timing and Spectral Properties of Be/X-Ray Pulsar EXO 2030+375 during a Type I Outburst, ApJ, 764, 158

Nakajima, M., Negoro, H., Serino, M., et al. 2018, MAXI/GSC detection of the outburst onset from the Be/X-ray binary pulsar 2S 1417-624, The Astronomer's Telegram, 11479, 1

Negueruela, I. 1998, On the nature of Be/X-ray binaries, A&A, 338, 505

Negueruela, I. 2007, in Astronomical Society of the Pacific Conference Series, Vol. 367, Massive Stars in Interactive Binaries, ed. N. St. -Louis & A. F. J. Moffat, 477

Okazaki, A. T., Hayasaki, K., & Moritani, Y. 2013, Origin of Two Types of X-Ray Outbursts in Be/X-Ray Binaries. I. Accretion Scenarios, PASJ, 65, 41

Okazaki, A. T. & Negueruela, I. 2001, A natural explanation for periodic X-ray outbursts in Be/X-ray binaries, A&A, 377, 161

Paczynskii, B. 1976, in BAAS, Vol. 8, 442

Parmar, A. N., White, N. E., & Stella, L. 1989a, The Transient 42 Second X-Ray Pulsar EXO 2030+375. II. The Luminosity Dependence of the Pulse Profile, ApJ, 338, 373

Parmar, A. N., White, N. E., Stella, L., Izzo, C., & Ferri, P. 1989b, The Transient 42 Second X-Ray Pulsar EXO 2030+375. I. The Discovery and the Luminosity Dependence of the Pulse Period Variations, ApJ, 338, 359

Patruno, A. & Watts, A. L. 2012, Accreting Millisecond X-Ray Pulsars, arXiv e-prints, arXiv:1206.2727

Pavlovskii, K., Ivanova, N., Belczynski, K., & Van, K. X. 2017, Stability of mass transfer from massive giants: double black hole binary formation and ultraluminous X-ray sources, MNRAS, 465, 2092

Petterson, J. A. 1978, On the occurrence of streams and disks in massive X-ray binary systems., ApJ, 224, 625

Porter, J. M. 1996, On the rotational velocities of Be and Be-shell stars, MNRAS, 280, L31

Porter, J. M. & Rivinius, T. 2003, Classical Be Stars, PASP, 115, 1153

Postnov, K. A., Gornostaev, M. I., Klochkov, D., et al. 2015, On the dependence of the X-ray continuum variations with luminosity in accreting X-ray pulsars, MNRAS, 452, 1601

Poutanen, J., Mushtukov, A. A., Suleimanov, V. F., et al. 2013, A Reflection Model for the Cyclotron Lines in the Spectra of X-Ray Pulsars, ApJ, 777, 115

Press, W. H. & Rybicki, G. B. 1989, Fast Algorithm for Spectral Analysis of Unevenly Sampled Data, ApJ, 338, 277

Pringle, J. E. 1981, Accretion discs in astrophysics, ARA&A, 19, 137

Puls, J., Vink, J. S., & Najarro, F. 2008, Mass loss from hot massive stars, A&A Rev., 16, 209

Raichur, H. & Paul, B. 2010, Apsidal motion in 4U0115+63 and orbital parameters of 2S1417-624 and V0332+53, MNRAS, 406, 2663

Reig, P. & Nespoli, E. 2013, Patterns of variability in Be/X-ray pulsars during giant outbursts, A&A, 551, A1

Reynolds, A. P., Parmar, A. N., & White, N. E. 1993, The Luminosity Dependence of the X-Ray Spectrum of the Transient 42 Second Pulsar EXO 2030+375, ApJ, 414, 302

Rivinius, T., Carciofi, A. C., & Martayan, C. 2013, Classical Be stars. Rapidly rotating B stars with viscous Keplerian decretion disks, A&A Rev., 21, 69

Roberts, D. H., Lehar, J., & Dreher, J. W. 1987, Time series analysis with CLEAN. I. Derivation of a spectrum., AJ, 93, 968

Romano, P., Campana, S., Chincarini, G., et al. 2006, Panchromatic study of GRB 060124: from precursor to afterglow, A&A, 456, 917

Romanova, M. M., Ustyugova, G. V., Koldoba, A. V., & Lovelace, R. V. E. 2004, The Propeller Regime of Disk Accretion to a Rapidly Rotating Magnetized Star, ApJ, 616, L151

Roming, P. W. A., Kennedy, T. E., Mason, K. O., et al. 2005, The Swift Ultra-Violet/Optical Telescope, Space Sci. Rev., 120, 95

Rothschild, R. E., Blanco, P. R., Gruber, D. E., et al. 1998, In-Flight Performance of the High-Energy X-Ray Timing Experiment on the Rossi X-Ray Timing Explorer, ApJ, 496, 538

Rouco Escorial, A., Bak Nielsen, A. S., Wijnands, R., et al. 2017, The low-luminosity behaviour of the 4U 0115+63 Be/X-ray transient, MNRAS, 472, 1802

Sako, M., Kahn, S. M., Paerels, F., et al. 2003, Structure and Dynamics of Stellar Winds in High-mass X-ray Binaries, arXiv e-prints, astro

Sasaki, M., Klochkov, D., Kraus, U., Caballero, I., & Santangelo, A. 2010, Analyzing X-ray pulsar profiles: geometry and beam pattern of EXO 2030+375, A&A, 517, A8

Scargle, J. D. 1982, Studies in astronomical time series analysis. II. Statistical aspects of spectral analysis of unevenly spaced data., ApJ, 263, 835

Schönherr, G., Wilms, J., Kretschmar, P., et al. 2007, A model for cyclotron resonance scattering features, A&A, 472, 353

Schreier, E., Giacconi, R., Gursky, H., Kellogg, E., & Tananbaum, H. 1972, Discovery of the Binary Nature of SMC X-1 from UHURU, ApJ, 178, L71

Schwarm, F. W., Ballhausen, R., Falkner, S., et al. 2017, Cyclotron resonant scattering feature simulations. II. Description of the CRSF simulation process, A&A, 601, A99

Shakura, N. I., Postnov, K. A., Kochetkova, A. Y., et al. 2015, Wind accretion: Theory and observations, Astronomy Reports, 59, 645

Shakura, N. I. & Sunyaev, R. A. 1973, Reprint of 1973A&A....24..337S. Black holes in binary systems. Observational appearance., A&A, 500, 33

Sidoli, L. & Paizis, A. 2018, An INTEGRAL overview of High-Mass X-ray Binaries: classes or transitions?, MNRAS, 481, 2779

Slettebak, A. 1988, The Be Stars, PASP, 100, 770

Soong, Y., Gruber, D. E., Peterson, L. E., & Rothschild, R. E. 1990, Spectral Behavior of Hercules X-1: Its Long-Term Variability and Pulse Phase Spectroscopy, ApJ, 348, 641

Staubert, R., Trümper, J., Kendziorra, E., et al. 2019, Cyclotron lines in highly magnetized neutron stars, A&A, 622, A61

Stella, L., White, N. E., & Rosner, R. 1986, Intermittent Stellar Wind Acceleration and the Long-Term Activity of Population I Binary Systems Containing an X-Ray Pulsar, ApJ, 308, 669

Taam, R. E., Fryxell, B. A., & Brown, D. A. 1988, A Model for the Recurrent Flares in EXO 2030+375, ApJ, 331, L117

Tananbaum, H., Gursky, H., Kellogg, E. M., et al. 1972, Discovery of a Periodic Pulsating Binary X-Ray Source in Hercules from UHURU, ApJ, 174, L143

Townsend, R. H. D., Owocki, S. P., & Howarth, I. D. 2004, Be-star rotation: how close to critical?, MNRAS, 350, 189

Tsygankov, S. S., Rouco Escorial, A., Suleimanov, V. F., et al. 2019, Dramatic spectral transition of X-ray pulsar GX 304-1 in low luminous state, MNRAS, 483, L144

Tsygankov, S. S., Wijnands, R., Lutovinov, A. e. A., Degenaar, N., & Poutanen, J. 2017, The X-ray properties of Be/X-ray pulsars in quiescence, MNRAS, 470, 126

Unger, S. J., Norton, A. J., Coe, M. J., & Lehto, H. J. 1992, Pulse phase-resolved X-ray spectroscopy of the transient high-mass X-ray binary V 0332+53., MNRAS, 256, 725

van den Heuvel, E. P. J. 1976, in Structure and Evolution of Close Binary Systems, ed. P. Eggleton, S. Mitton, & J. Whelan, Vol. 73, 35

van den Heuvel, E. P. J. 2004, X-ray binaries and their descendants: binary radio pulsars; evidence for three classes of neutron stars?

van den Heuvel, E. P. J. & Heise, J. 1972, Centaurus X-3, Possible Reactivation of an Old Neutron Star by Mass Exchange in a Close Binary, Nature Physical Science, 239, 67

van den Heuvel, E. P. J., Portegies Zwart, S. F., & de Mink, S. E. 2017, Forming short-period Wolf-Rayet X-ray binaries and double black holes through stable mass transfer, MNRAS, 471, 4256

van der Klis, M., Stella, L., White, N., Jansen, F., & Parmar, A. N. 1987, Intensity and Source State Dependence of the Quasi-periodic Oscillations in Scorpius X-1, ApJ, 316, 411

van Paradijs, J. & McClintock, J. E. 1994, Absolute visual magnitudes of low-mass X-ray binaries., A&A, 290, 133

Warner, B. 2003, Cataclysmic Variable Stars

Wheaton, W. A., Dunklee, A. L., Jacobsen, A. S., et al. 1995, Multiparameter Linear Least-Squares Fitting to Poisson Data One Count at a Time, ApJ, 438, 322

White, N. E., Swank, J. H., & Holt, S. S. 1983, Accretion powered X-ray pulsars., ApJ, 270, 711

Willingale, R., Starling, R. L. C., Beardmore, A. P., Tanvir, N. R., & O'Brien, P. T. 2013, Calibration of X-ray absorption in our Galaxy, MNRAS, 431, 394

Wilms, J., Allen, A., & McCray, R. 2000, On the Absorption of X-Rays in the Interstellar Medium, ApJ, 542, 914

Yang, J., Zezas, A., Coe, M. J., et al. 2018, Anticorrelation between X-ray luminosity and pulsed fraction in the Small Magellanic Cloud pulsar SXP 1323, MNRAS, 479, L1

Zeldovich, Y. B. & Guseynov, O. H. 1966, Collapsed Stars in Binaries, ApJ, 144, 840